Heinrich Heine
Universität
Düsseldorf

Laser pump-probe experimental studies in the relativistic regime

Inaugural-Dissertation

zur Erlangung des Doktorgrades
der Mathematisch-Naturwissenschaftlichen Fakultät
der Heinrich-Heine-Universität Düsseldorf

vorgelegt von

Esin Aktan
geboren in Duisburg

Düsseldorf, November 2020

Düsseldorf DARC turus
LASER FACILITY

aus dem Institut für Laser- und Plasmaphysik
der Heinrich-Heine-Universität Düsseldorf

Gedruckt mit der Genehmigung der
Mathematisch-Naturwissenschaftlichen Fakultät der
Heinrich-Heine-Universität Düsseldorf

Berichterstatter:
1. Prof. Dr. Oswald Willi
2. Prof. Dr. Alexander Pukhov

Tag der mündlichen Prüfung: 25.01.2021

"Dünyada her şey için; uygarlık için, hayat için, başarı için en hakiki mürşit ilimdir; fendir. İlim ve fennin dışında rehber aramak dikkatsizliktir, bilgisizliktir, yanlışlıktır."

(For everything in the world; for civilisation, for life, for success; the only true mentor is knowledge; is science. Seeking a guide outside of science and knowledge is carelessness, ignorance and fallacy.)

M. K. Atatürk

Abstract

The interaction between high-intensity, ultrashort laser pulses with solid matter is characterised by unique properties. In this thesis, various experimental studies investigating different fields of physics resulting from the irradiation of (ultra-)thin solid targets by a high-intensity ($\approx 10^{20}$ W/cm^2) and ultrashort (≈ 30 fs) high power laser are carried out. The double-chirped pulse amplification (CPA) architecture of the Arcturus laser facility at the Heinrich-Heine-University in Düsseldorf is exploited in order to address different experimental configurations and therefore different physical processes.

In the first part, the plasma dynamics from dual beam experiments are investigated by employing various diagnostics. A striking feature in the experimental study of the laser energy absorption by ultra-thin diamond-like carbon (DLC) foils could be observed. Different physical parameters including the laser energy on target and the target thickness are studied. Moreover, the ion acceleration from an already exploded thin foil target in a dual beam configuration is investigated.

Furthermore, employing the proton probing technique, the parameters influencing the electromagnetic pulse generated by the high-intensity laser and solid interaction have been investigated. The parametric study, including laser pulse duration, energy and intensity, revealed the strong dependence of the amplitude of the electromagnetic pulse on the incident laser energy and pulse duration. A semi-analytical model confirmed the experimentally obtained results and an optimum pulse duration for a given laser energy was found to be close to 100 fs. Motivated by the agreement between the experiments and the analytical model, simulations for a larger range of laser energies are demonstrated in order to estimate the optimum pulse duration of the electromagnetic pulse for example for future facilities.

Exploiting the properties of laser-accelerated proton beams, electric fields induced by the laser-target interaction are diagnosed by employing the proton probing technique. Due to the high temporal and spatial resolution, the proton probing technique is a highly powerful tool to probe the distinct features of the laser-target interaction. For the first time, the effect of the laser light polarisation on the interaction could be demonstrated experimentally. In case of circularly polarised light, the proton probing images show that the target is pushed forward as a compressed layer due to the less efficient heating of the electrons (which is evident for RPA), while in case of linearly polarised light, the target is significantly decompressed, since the electrons are heated efficiently by the TNSA process.

Zusammenfassung

Die Wechselwirkung zwischen hochintensiven ($\approx 10^{20}$ W/cm^2), ultrakurzen Laserpulsen ($\approx$ 30 fs) mit Festkörper-Targets zeichnet sich durch einzigartige Eigenschaften aus. In dieser Arbeit werden unterschiedliche experimentelle Studien durchgeführt, die verschiedene Bereiche der Physik untersuchen, die sich aus der Bestrahlung von (ultra-)dünnen Targets mit Hochleistungslasern ergeben. Mit Hilfe der double-CPA-Architektur der Arcturus-Laseranlage an der Heinrich-Heine-Universität Düsseldorf, werden unterschiedliche experimentelle Konfigurationen und damit unterschiedliche physikalische Prozesse adressiert.

Im ersten Teil wird die Plasmadynamik aus Doppelstrahlexperimenten mit Hilfe verschiedener Diagnostiken untersucht. Ein auffälliges Merkmal bei der experimentellen Untersuchung der Absorption von Laserenergie durch ultradünne diamantähnliche Kohlenstofffolien (DLC) konnte beobachtet werden. Verschiedene physikalische Parameter, einschließlich der Laserenergie und der Targetdicke, werden untersucht. Darüber hinaus wird die Ionenbeschleunigung von einem bereits explodierten, dünnen Folientarget in einer Doppelstrahlkonfiguration untersucht.

Darüber hinaus wurden unter Verwendung der Protonenradiographietechnik die Parameter untersucht, die den elektromagnetischen Puls beeinflussen, der bei der Laser-Target-Wechselwirkung erzeugt wird. Die parametrische Studie zeigte die starke Abhängigkeit des elektromagnetischen Pulses von der einfallenden Laserenergie und Pulsdauer. Ein semi-analytisches Modell bestätigte die experimentellen Ergebnisse und eine optimale Pulsdauer nahe bei 100 fs wurde bestimmt. Motiviert durch die Übereinstimmung der Experimente und dem analytischen Modell werden Simulationen für einen größeren Bereich von Laserenergien demonstriert, um die optimale Pulsdauer beispielsweise für zukünftige Einrichtungen abzuschätzen.

Die Eigenschaften laserbeschleunigter Protonenstrahlen werden ausgenutzt, um elektrische Felder, die durch die Laser-Target-Wechselwirkung induziert werden, mit Hilfe der Protonenradiographietechnik zu diagnostizieren. Aufgrund der hohen zeitlichen und räumlichen Auflösung ist diese ein äußerst leistungsfähiges Werkzeug, um den Einfluss der Laserlichtpolarisation auf die Wechselwirkung nachzuweisen. Zum ersten Mal konnte experimentell demonstriert werden, dass bei zirkular polarisiertem Licht das Target aufgrund der weniger effizienten Erwärmung der Elektronen (ein Indiz für RPA) als komprimierte Schicht nach vorne gedrückt wird, während bei linear polarisiertem Licht das Target signifikant dekomprimiert wird, da die Elektronen durch den TNSA-Prozess effizient erwärmt werden.

Contents

1 Introduction

Since the invention of the first operative laser in 1960 by Ted Maiman [1], the main aim was to reach shorter and shorter pulses [2]. Nowadays, pulse durations in the femtosecond range can be achieved easily. For these ultrashort pulse durations the commonly used chirped-pulse amplification (CPA)-technique is crucial [3] [4]. With the development of the CPA technique, high-intensity and ultra-short laser pulses can now be generated, which yield the opportunity of producing and investigating rapidly heated matter. Peak powers of the laser pulse up to petawatt range can be achieved [5] [6]. Focusing the CPA generated laser pulse to a few µm enables reaching intensities up to 10^{21} W/cm^2. Laser pulses ionise targets (solids or gases) rapidly and generate a plasma at high intensities. Different physical processes can be observed depending on the laser intensity and target density. The experimental and theoretical investigations of the interaction between solid targets and ultra-short and high-intensity laser pulses have become an active research area in the last decades.

Advances in high-intensity and ultra-short pulses made it possible to generate energetic particles from laser-plasma interaction, like relativistic electrons[7] [8], γ-rays [9] and multi-MeV ions [10] [11] [12]. Particularly laser-driven protons have attracted great attention. Their potential for various applications such as proton probing [13] [14], fast ignition in inertial fusion [15] [16], proton therapy in oncology [17] [18] etc. leads to an intense research interest.

During the interaction of a high-intensity laser pulse with a (thin) metallic foil target, protons and heavier ions are accelerated by an electric field formation. Protons which are originating from hydrocarbon contamination layers on the surfaces of the foil are usually accelerated easier than heavier ions, unless prepared in a particular way [19] [20] [21].

Compared to conventional accelerators, laser-driven ions/protons have several advantages: high brightness ($\sim 10^{12}$ protons on a picosecond time scale) [22], high intensity, ultra-low emittance [23], high laminarity [24], multi MeV-energy spectral cut-off and short pulse durations. Since all "peak" quantities are high compared to conventional accelerators, laser-driven ions are most suitable for time-resolved and single-shot applications. However, the average beam properties of laser-based accelerators are quite low since repetition rates are limited due to current technology standards regarding requirements for average optical powers and thermal load. Nevertheless, the reduced acceleration length of laser-based particle accelerators is

one of the greatest advantages. While conventional accelerator facilities have large dimensions, laser-based accelerators are more compact and can be used on smaller laboratory scales.
The most extensively studied laser-driven ion acceleration mechanism is the target normal sheath acceleration (TNSA) scheme. Irradiating a foil target with a high-intensity laser pulse leads to a build-up of TV/m electric fields at the rear side of the target, which is emerging due to relativistic electrons generated from the laser-irradiated side of the foil. The electrons are typically heated via the oscillating $\vec{j} \times \vec{B}$-heating mechanism of the linearly polarised laser pulse [21] [25] [26].
Another approach of accelerating ions using thin foil targets is based on using circularly polarised laser light. Irradiating a target with circularly polarised light, a strong electrostatic field is established, since the oscillating component of the $\vec{j} \times \vec{B}$-heating is vanished and the heating of the electrons is suppressed. Electrons are piled up into a compressed layer which induces a strong charge separating field [27] [28] [29].
The properties of laser-accelerated particles appoint them attractive for different applications. Short-pulsed radiation sources like X-rays are well suited for the study of the structures and properties of matter on the atomic scale length [30].
Radiation therapy is a commonly used method in cancer treatment. For tumours which are close to risk organs, for which a surgery would be not trivial, radiation therapy is chosen. High-energy ions have several advantages compared to electron beams or Bremsstrahlung. Since ions have a well-defined penetration depth and a distinct Bragg peak at the end of the penetration path, they are of great importance for radiation therapy. The stopping power increases towards the end of the range and reaches a maximum (the Bragg peak) right before it drops to zero. Combined with small side scatterings, they are rather convenient in oncology, since healthy tissue around the tumour tissue is exposed to much less dose. Ion beams are found to induce a greater damage up to a factor of six compared to Bremsstrahlung [30]. However, conventional accelerators in ion beam therapy are large and expensive. Hence research in laser-driven ions is getting into focus [17] [31].

The experimental studies in this thesis concentrate on the properties of plasmas generated by the interaction of high intensity, high-contrast laser pulses with (ultra-) thin solid targets. The experiments were carried out at the Arcturus laser facility at the Heinrich-Heine-University in Düsseldorf, Germany. The unique property of the Arcturus laser facility allows to use a dual beam configuration in which the laser parameters of each beam can be adjusted separately. A plasma mirror

system is enhancing the laser contrast up to 10^{-12} on a time scale of a few tens of picoseconds before the main peak. Especially for very thin and delicate targets an excellent contrast is desirable, since the pre-pulse of the laser pulse can already destroy the target.
The architecture of the Arcturus laser facility allows to address different physical processes. In this thesis, the fundamental processes of laser energy transfer and ion acceleration using laser absorption measurements, ion spectrometers and different imaging diagnostics were investigated.
Furthermore, the generation and optimisation of a laser-driven electro-magnetic pulse on solid surfaces is presented. A parametric study is performed in order to optimise laser parameters.
Moreover, the dynamics of the laser and ultra-thin foil interaction are visualised by employing the proton imaging technique. The impact of different polarisations of the laser light (linear and circular) is shown.

This thesis is structured as follows:

- First, in chapter 2, an introduction of the main physical parameters of laser induced plasmas is given. The dynamics of the motion of a free electron in the electromagnetic field are described.
  Further, the relevant physical processes occurring during the interaction between the laser and a solid target are presented. Primary effects such as ionisation processes are described, including their characteristics and validity domains. Different collisional and collisionless absorption mechanisms are summarised. The absorption coefficient for the different processes is given. An overview for the main ion acceleration mechanisms is given. Front and rear surface ion acceleration are discussed. In the last section of this chapter, relativistic effects such as relativistic transparency and relativistic self-focusing are reviewed. The main conditions and processes for these effects are presented.

- In chapter 3, the experimental methods and diagnostics used to obtain the experimental results in this thesis are introduced. The high power Arcturus laser system is presented to begin with, followed by the description of the ion detection diagnostics such as a Thomson-parabola-MCP assembly and radiochromic films. Last, the principles of the proton probing technique are discussed.

- Chapter 4 presents the study for controlled plasma dynamics from dual beam experiments. Various methods and diagnostics are used in order to investigate the absorption and ion acceleration mechanisms. The results indicate a significant decrease of the transmission laser energy fraction at a specific delay between the two pulses. Simultaneously, an increase in the proton energy can be observed. Intriguingly, the minimum in transmission is shifting with the laser energy. Increasing the laser energy leads to a drop in transmission at earlier delays.
  The channelling of a laser pulse through a plasma is probed by a simple imaging system. A dependence between the channelling and the density of the plasma could be found.

- A parametric study of an intense-laser driven electromagnetic pulse is presented in chapter 5. The dependence of an electromagnetic pulse on the laser parameters (such as energy, pulse duration and intensity) is investigated by employing the proton probing technique. Using wire targets engineered in a special way supports the study of the dynamics of the electromagnetic pulse. The square wave pattern allows to control the spatial confinement of the charge pulse, thus increasing the field of view of the probing proton pulse. An optimum for the electromagnetic amplitude is found around 100 fs of the laser pulse duration.

- In Chapter 6, the study of dynamics of thin foils irradiated by a high intensity laser pulse with two different polarisations (linear and circular) is described. By employing the proton probing technique, one is able to investigate the interaction at different moments of time in one single shot. The study shows that the polarisation has a great impact on the interaction. The acceleration mechanism for each polarisation is different. While the target is decompressed and the laser pulse creates a hole in the target in the linearly polarised case, the whole foil is pushed forward as a dense compressed layer in the circularly polarised case.

- The final chapter summarises the experimental and simulation results in this thesis. Last but not least, an outlook for future investigations is given.

Role of author

The experiments presented in this thesis were carried out at the Arcturus laser facility in Düsseldorf. The author was involved as a main investigator in planning,

setting up and running the experimental diagnostics under the supervision of Dr. Rajendra Prasad.
Some parts of the theoretical background presented in chapter 2 are adopted from the author's master thesis.
The analysis of the experimentally obtained data is entirely conducted by the author. Some analysis tools and simulations were provided externally.
The evaluation of proton energy in chapter 4 is done by using a Matlab code developed by A. Alejo Alonso. Analytical calculations for the interpretation of the experimental observations are provided by A. P. L. Robinson.
A C++ code developed by A. Shiavi [32] is used in order to obtain the linear charge pulse density presented in chapter 5. Semi-analytical simulations confirming the experimental data are provided by A. Poyé. Some parts of this chapter are already published in [139].
The 2D PIC simulations presented are carried out by Dr. Rajendra Prasad. The particle tracer simulations are provided by L. Romagnani.

2 Physical processes in laser-plasma interaction

In this chapter, the main physical processes relevant for the interaction between a laser pulse and matter are presented. The effect of the electromagnetic field of the laser pulse on the solid matter surface strongly depends on its intensity. In order to ionise matter and create a plasma, high intensities well above the surface damage threshold are needed. Therefore the laser energy needs to exceed the ionisation energy, which is the minimum energy required to remove the valence electron of a neutral atom or molecule. Usually, single photons are not energetic enough to ionise the atom. An atom can be ionised by either absorbing one high-frequency photon or several lower frequency photons. Multi-photon effects depend on the number of photons required for the ionisation process. High-intensity lasers make it possible to reach high photon-densities. In case of ultra-short, high-intensity laser pulses, the laser field is rapidly coupled into the solid matter which leads to a fast ionisation of the target surface within the first few laser pulse cycles.
This chapter presents an overview of the physical parameters relevant for characterisation of the laser induced plasma. Since electrons are the main energy carriers in ultra-short laser pulse interactions, the dynamics of the motion of a free electron in an electromagnetic field will be presented.
Subsequently, ionisation mechanisms dominant at different intensity regimes are introduced. The consecutive interaction of laser and plasma are depending on the laser intensity and the energy absorption efficiency. The relevant absorption mechanisms depending on the laser parameters are demonstrated.
Laser accelerated ion beams have become a highly interesting and active research area. Multi MeV ion beams accelerated during the interaction of short and intense laser pulses with thin solid foils have provided a dynamic tool to explore the fast dynamics of laser produced plasmas [33] [34]. The main mechanisms and properties of accelerated ion beams will be discussed.
Finally, relativistic effects, such as relativistic transparency and relativistic self-focusing, are going to be described. Since the laser intensities achieved in the experiments in this thesis reach the relativistic regime, relativistic effects play an important role.

2.1 Laser pulse interaction with solid matter

Being exposed to high intensity irradiation, matter is ionised rapidly. The released electrons will immediately be captured in the electromagnetic field of the laser and start oscillating with a distinctive energy. The interaction of the electrons and the electric and magnetic field influence a wide variety of laser-plasma processes.
In general, electrons determine the interaction physics of laser radiation with matter, since the electromagnetic field couples the energy to the electrons.
During laser and matter interaction, several processes occur due to the electromagnetic field of the laser pulse. The laser parameters have an impact on the interaction and affect the physical processes.
In the following, the motion of a single electron in an electromagnetic field and the related most significant laser parameters will be presented.

2.1.1 Dynamics of a free electron in the electromagnetic field

Plasmas are difficult to analyse, since sometimes they behave like fluids and sometimes like a collection of individual particles. In a first step, it is important to understand the behaviour of a single particle in an electric and magnetic field.
Considering uniform $\vec{E}-$ and $\vec{B}-$fields, which are assumed to be described and not affected by charged particles, the motion of a particle in the presence of an electromagnetic field can be described by the Lorentz equation

$$\frac{d\vec{p}}{dt} = \frac{d(\gamma m_e \vec{v})}{dt} = -q\left(\vec{E} + \frac{1}{c}\vec{v_e} \times \vec{B}\right), \tag{2.1.1}$$

where $\vec{p}$ is the momentum, m_e the electron mass, v_e the electron velocity, q the charge and γ the relativistic factor $\gamma = 1/\sqrt{1-(\frac{v}{c^2})}$. The motion is a superposition of two motions: a circular Larmor gyration and a drift of the guiding centre, linear along the magnetic field. Considering a plane and linearly polarised electromagnetic field, the electric and magnetic field components are given by:

$$\begin{aligned} \vec{E}(\vec{r},t) &= \vec{E_0} cos(\omega t - \vec{k}\vec{z}) \\ \vec{B}(\vec{r},t) &= \vec{B_0} sin(\omega t - \vec{k}\vec{z}), \end{aligned} \tag{2.1.2}$$

where $\omega = \frac{2\pi c}{\lambda}$ is the angular laser frequency and $\vec{k}$ the propagation factor. In the non-relativistic case, the magnetic term $\vec{v} \times \vec{B}$ of the Lorentz force can be neglected,

thus reducing the equation of motion to

$$\frac{d\vec{v}}{dt} = -\frac{q}{m}\vec{E}. \tag{2.1.3}$$

Assuming the initial conditions $\vec{x}(t=0) = 0$ and $\vec{v}(t=0) = 0$, the motion of an electron can easily be calculated by integrating the momentum over time, which yields a transverse harmonic oscillation in the electric field with an amplitude $x_0 = \frac{eE_0}{m_e\omega^2}$, with a maximum velocity of $v_0 = \frac{eE_0}{m_e\omega}$.
The transition from non-relativistic to relativistic particle motions can be described by means of the dimensionless parameter

$$a_o = \frac{eE_L}{m_e\omega c} = \frac{eE_0\lambda}{2\pi m_e c^2} = \frac{E_{osc}}{E_0} = 0.85 \times \sqrt{1 + I\lambda^2/10^{18}}, \tag{2.1.4}$$

where e represents the electron charge, m_e the electron mass, c the speed of light and E_L the field strength of the laser. In other words, the dimensionless parameter a_0 can be described by the ratio of the momentum of an electron moving in the laser field, divided by its rest momentum. A non-relativistic case can be considered for $a_0 \ll 1$ and a relativistic case for $a_0 \geq 1$. In the relativistic case, the relativistic factor $\gamma = \frac{1}{\sqrt{1-v^2/c^2}}$ becomes crucial.
The effect of the laser field strength on the electrons can be described using the dimensionless parameter. Considering a laser beam with a radial profile $E(r) = E_0 exp(-r^2/2\sigma^2)$ and the dimensionless parameter, the electromagnetic field can be redefined in practical units as follows:

$$E_0 = \frac{m2\pi c^2}{\lambda e}a_0 \cong \frac{a_0}{\lambda[\mu\text{m}]}3.2 \times 10^{12}[\text{V/m}] \tag{2.1.5}$$

$$B_0 = \frac{E}{c} = \frac{m2\pi c}{\lambda e}a_0 \cong \frac{a_0}{\lambda[\mu\text{m}]}1.067 \times 10^{4}[\text{T}]. \tag{2.1.6}$$

This implies for the intensity:

$$I = \frac{c\varepsilon_0}{2}E_0^2 = \frac{c\epsilon_0}{2}\left[\frac{m2\pi c^2}{\lambda e}a_0\right]^2. \tag{2.1.7}$$

Note that the above mentioned parameters 2.1.4 - 2.1.7 are only valid for electrons. Further, the total laser power is described by the relation:

$$P_L = \pi c\epsilon_0 \int_0^\infty E(r)^2 r \, \mathrm{d}x. \tag{2.1.8}$$

In a practical units, the intensity can be calculated as follows

$$I = \frac{E}{\tau \pi R^2}, \tag{2.1.9}$$

where R indicates the beam radius, E the beam energy and τ the laser pulse duration.
Electrons with an energy $E > E_0$ and $a_0 \geq 1$ become relativistic and have a velocity close to the speed of light (e.g. E = 1 MeV, v = 0.28×10^9 m/s = 0.93c). High energy electrons generated by high intense laser pulses are at the origin of a large number of processes in plasma like acceleration of ions [29], high energy radiation, self induced transparency [35] etc.. Therefore, the understanding of electron acceleration and the dynamics in the laser field are of key importance in the further approach of these processes.
If electrons approach the speed of light, relativistic effects become relevant. The threshold for relativistic effects is $\langle v \rangle = \sqrt{\frac{2k_B T}{m}} \geq 0.3c$.
In addition to the linear acceleration of electrons, there is a "sidewise"motion which is called "*drift*". This drift motion occurs if a force (i.e. magnetic and gravitational field, time- and/or space-dependent magnetic/electric field) acts on a free particle. If the magnetic field exerts sufficient force on an electron, a nonlinear, average forward drift of the electron in the direction of propagation is caused. This drift velocity can be defined as follows:

$$\vec{v_D} = \overline{v}_x = c\frac{a_0^2}{4 + a_0^2}. \tag{2.1.10}$$

The drift motion allows particles to escape the magnetic confinement by moving across the magnetic field lines. Figure 2.1 illustrates the motion of an electron in a linearly polarised electromagnetic field in the laboratory reference frame. The electrons have a sidewise drift motion in propagation direction and an oscillation in polarisation direction of the electric field. Regarding a reference frame, which is moving with the drift velocity, the shape of the electrons' motion turns into a figure of eight (cf. figure 2.1). Considering an electron at rest, the free electron gets a drift motion in propagation direction during the presence of a laser pulse and rests again afterwards. Ultimately, the electrons net-energy does not change. Due to the focusing, the laser field becomes inhomogeneous and an intensity gradient is present which needs to be taken into account. Electrons are moving (oscillating) slightly off-centre of the focussed beam. After the first half of the laser cycle, the repelling force becomes smaller, as the laser field strength decreases

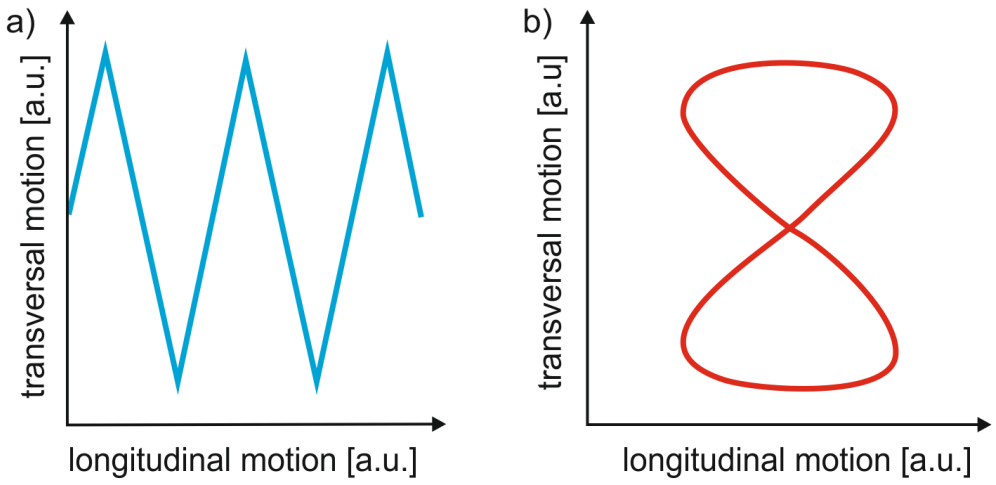

Figure 2.1: Motion of an electron in a linear polarised electromagnetic field in a) laboratory reference frame and b) in the rest frame moving with an average drift velocity (cf. [59] [36]).

with distance from the laser axis. The electrons cannot return to their place of origin. The electrons will be accelerated away from the laser axis, i.e. from an

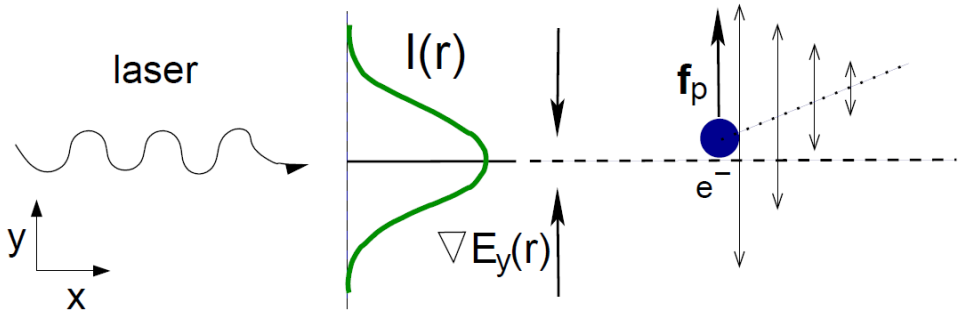

Figure 2.2: Schematic imaging of the electron motion caused by the ponderomotive force f_p. The electron is accelerated away from the laser axis towards the area with lower intensity [36].

area of high intensity towards an area of lower intensity. This effect is caused by the ponderomotive force, which can be defined as the gradient of the oscillation potential which is averaged over time (cf. figure 2.2) using the already mentioned dimensionless parameter a_0 (cf. equation 2.1.4) the ponderomotive potential can be described as [36]

$$U_P = \frac{m_e}{2}\frac{e^2 E_0^2}{2m_e\omega^2} = m_e c^2 \frac{a_0^2}{4\bar{\gamma}} \tag{2.1.11}$$

where $\bar{\gamma}$ is the γ-factor of an electron averaged over one period. For laser light at an incidence angle normal to the target, the ponderomotive force per unit volume

can be identified by following the deviation in [36] as

$$f_P = m\overline{\frac{\partial v_y^2}{\partial t}} = -\frac{e^2}{4m\omega^2}\frac{\partial E_0^2}{\partial y} = -\bigtriangledown U_P. \tag{2.1.12}$$

Note that the space dependent electric field is averaged over one laser oscillating period while the laser pulse propagates in z-direction. The ponderomotive force is non-linear. A slow time scale force is induced by a high-frequency laser field.
In the relativistic regime at high intensities ($\geq 10^{18}$ W/cm^2), the magnetic field component of the Lorentz force is no longer negligible. Similar to the non-relativistic regime, the ponderomotive force pushes the electrons away from regions of higher intensity. A single electron will drift forward due to the magnetic field and will experience a relativistic mass increase during the first half of the laser cycle. In the second half of the laser cycle, the repelling force is weaker due to the lower intensity, and thus the electron moves sidewise and forward. To derive the relativistic ponderomotive force, in [36] the electron motion is separated into slow (p^s) and fast (p^f) components which leads to the relativistic expression of the ponderomotive force:

$$f_P^{rel} = \frac{dp^s}{dt} = -mc^2 \bigtriangledown \bar{\gamma}, \tag{2.1.13}$$

where $\gamma = \left(1 + \frac{p_s^2}{m^2c^2} + \frac{1}{2}a_0^2\right)^{1/2}$ is the relativistic factor and p_s the momentum of the electron motion's slow component.

2.2 Laser produced plasmas

The energy which is needed for creating a plasma can be gained by different processes such as thermal excitation, electrical gas discharge, electromagnetic fields or excitation by radiation.
The exact effects of the laser pulse strongly depend on its intensity. If the intensity is high enough to ionise the electrons, the electrons start oscillating freely in the field of the electromagnetic wave. If the energy which is added to the electrons is high enough, the electrons can release more electrons by collisions with neutral atoms which likewise start oscillating in the electromagnetic field. The quantity of free electrons and positive ions starts to grow in an avalanche-manner. The electron temperature increases rapidly, which leads to an expansion of the plasma. Ionised gas can be classified as a plasma, if the following criteria are fulfilled: high quantity of particles, shielding of charge and quasi-neutrality. In the following,

characteristic lengths and periods of time in a plasma will be presented.
Considering a positive test charge $+Z_e$ in a plasma, it will attract electrons in spite of thermal motion, which tends to randomise the charge distribution. The positive test charge will be screened by the electrons which leads to electrical neutrality. Starting with Poisson's equation in one dimension and Z = 1

$$\nabla^2\phi = -\frac{\rho}{\varepsilon_0} = \frac{e}{\varepsilon_0}(n_e - n_i), \tag{2.2.1}$$

where n_e and n_i are the electron and ion density, respectively, the shielding distance can be calculated. In thermal equilibrium, the electron density follows a Boltzmann distribution and is given by:

$$n_e = n_0 exp(\frac{e\phi}{k_B T_e}), \tag{2.2.2}$$

where n_0 is the number density at $\phi = 0$, $\phi = \frac{e}{4\pi\varepsilon_o r} exp(-r/\lambda_D)$ the screened Coulomb potential, k_B the Boltzmann constant and T_e the electron temperature. Assuming ions are heavy and thus they do not move on a time scale of interest, the ion density is found to be $n_i = n_0$. For $|e\phi/k_B T_e \ll 1|$, the exponential can be expanded in a Taylor series. The region where $|e\phi/k_B T_e|$ is large does not contribute much to the sheath, since the potential decreases rapidly. Keeping only the linear terms, the Debye length can be defined as

$$\lambda_D = \left(\frac{k_B T_e}{4\pi n_e e^2}\right)^{1/2}. \tag{2.2.3}$$

This is the characteristic length at which the electrostatic potential decreases to the $1/e$-fold amount. The Debye length gives the radius of a volume which is called Debye sphere. The amount of charged particles within the Debye sphere is crucial for classifying a plasma. The charge within the Debye sphere is shielded from the outside. The number of particles within the Debye sphere can be calculated by the plasma parameter:

$$N_D = \frac{4\pi}{3}\lambda_D^3 n_e. \tag{2.2.4}$$

For $N_D \gg 1$, an ionised gas can be called a plasma. From a macroscopic point of view a plasma behaves neutrally. The electrons are oscillating around the much heavier and inert ions. The frequency of this oscillation can be derived using

Poisson's equation and Newton's second law, which yields the plasma frequency

$$\omega_P = \sqrt{\frac{e^2 n_e}{\varepsilon_0 m_e}} \cong 5.6 \times 10^4 \sqrt{n_e}[\mathrm{cm}^{-3}][\mathrm{s}^{-1}]. \tag{2.2.5}$$

For an electromagnetic wave $E = E_0 exp(kx - \omega t)$ with the wave vector $|\vec{k}| = \mathrm{k} = 2\,\pi/\lambda$, the plasma dispersion relation in a plasma can be defined as [37]:

$$\omega^2 = \omega_P^2 + c^2 k^2. \tag{2.2.6}$$

Light propagation through a plasma is only possible for $\omega_L > \omega_P$. The condition $\omega_L < \omega_P$ would lead to an imaginary wave vector, and thus light propagation would not be possible because the electrons can follow the field, which leads to a shielding of the laser light.
Using the limiting case $\omega_L^2 - \omega_P^2 = c^2 k^2 = 0$ and equation 2.2.5, the critical density can be defined as

$$n_c = \frac{\varepsilon_0 m_e}{e^2} \cdot \omega_P^2 \approx 1.1 \times 10^{21} (\lambda^2/(\mu\mathrm{m})^2)\mathrm{cm}^{-3}. \tag{2.2.7}$$

This is the density at which the plasma becomes opaque for electromagnetic waves. A plasma is underdense if $\frac{\omega_L^2}{\omega_P^2} = \frac{n_e}{n_c} \ll 1$ and overdense if $\frac{\omega_L^2}{\omega_P^2} = \frac{n_e}{n_c} \gg 1$. The density profile of a non-uniform plasma is shown in figure 2.3 as a function of the distance x. The electromagnetic wave can penetrate into the plasma until the critical density is reached. At this point, the plasma becomes overdense and the electromagnetic wave will be reflected. Due to the propagation of light the electron density n_e is changing. The refractive index

$$\eta = \frac{ck}{\omega} = \sqrt{1 - \frac{\omega_P^2}{\omega^2}} = \sqrt{1 - \frac{n_e}{n_c}} \tag{2.2.8}$$

is depending on both the critical density and the electron density.
At the critical density, electrons oscillate as fast as the wave. Propagating though the plasma, a part of the light will be absorbed and, reaching the critical density, reflection begins. Plasmas have temperature gradients, because the energy is transported in form of electron heat conduction and x-rays from the area of high density towards areas of lower density. The spatial dependence between temperature and density can be seen in figure 2.4. The plasma generated by a laser starts expanding and streams away from the surface of the irradiated material with a high velocity due to the plasma pressure which is created during the heating of the

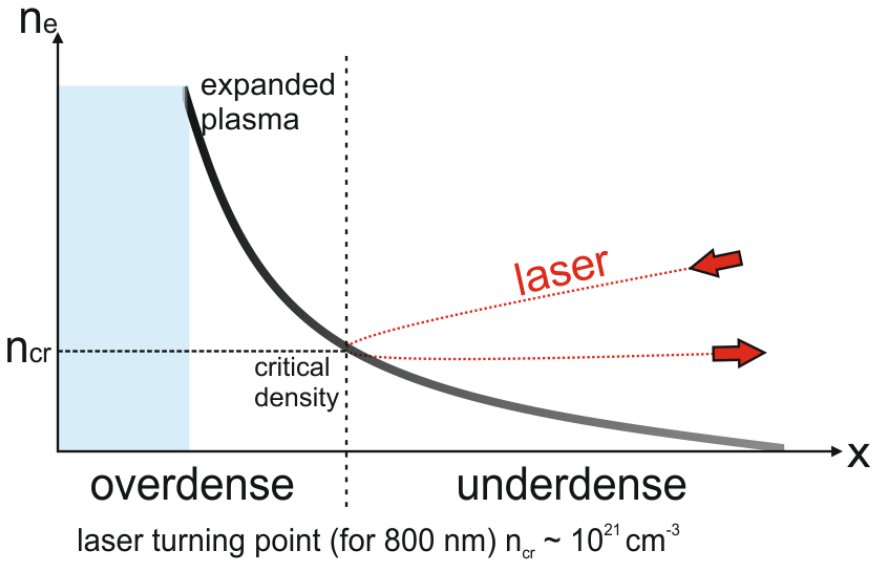

Figure 2.3: Schematic representation of light propagation in a non-uniform plasma. The plasma density is plotted against the distance x. The critical density is approximately $n_{cr} \sim 10^{21}$ for 800 nm.

material. The velocity of the expansion is almost equal to the ion acoustic velocity $c_s = (Z \times k_B T_e/m_i)^{1/2}$, where $Z*$ represents the effective ion charge and m_i the ion mass. Assuming isothermal expansion of the plasma, a decreasing density profile with a well-defined scale length is obtained [38]

$$L = c_s \tau_L \approx 3 \left(\frac{T_e}{keV}\right)^{1/2} \left(\frac{Z*}{A}\right)^{1/2} \tau[\text{Å}]. \tag{2.2.9}$$

Reaching a steep density gradient, the laser pulse immediately interacts with the created plasma.

Laser driven plasmas can be divided into two categories: thermal and non-thermal laser plasmas. The plasma pressure in thermal plasmas is rather high, thus increasing the amount of collisions between particles and favouring the energy transfer between them. The radiation within the plasma has a Planck-like spectrum. Such plasmas can convert a large part of the applied laser energy into hard radiation. Non-thermal plasmas have a lower pressure than thermal plasmas. Here, the mean-free-path is large, and thus no other considerable energy transfer between the particles can be observed except for electron collisions. There is no thermodynamical equilibrium present. The plasma temperature is inhomogeneous, since a certain part of the plasma consists of high energy electrons (20 keV - 10 MeV).

Defining the plasma temperature is only possible close to the equilibrium state.

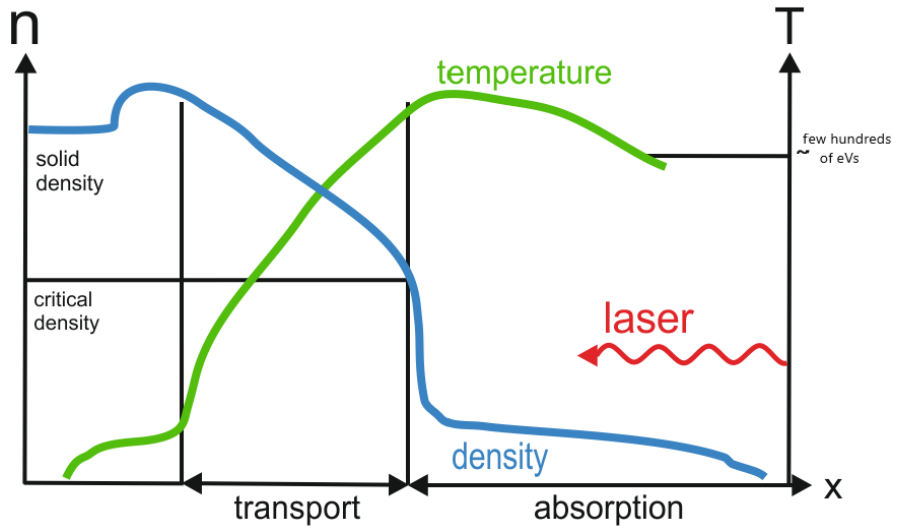

Figure 2.4: Schematics of the density and temperature spatial dependence (1D) in laser generated plasmas. Until reaching the critical density, the temperature decreases very fast and a shockwave arises.

Here, the average kinetic energy strongly depends on the temperature, hence a definition of the plasma temperature in units of the energy is only possible close to the equilibrium state. Laser produced plasmas can have temperatures of several MeV. The temperature is often given in eV and the energy corresponding to $k_B T_e$ can be derived by $k_B T_e = 1\ \text{eV} = 1.6 \times 10^{-19}$ J, which rearranged yields:

$$T = \frac{1.6 \times 10^{-19}}{1.38 \times 10^{-23}} = 11600.$$

Thus the conversion factor follows: 1 eV = 11600 K [39].
Summarising, a plasma is defined as a quasineutral gas consisting of charged and neutral particles which features collective behaviour. An ionised gas needs to satisfy three conditions to be entitled as a plasma:

- It needs to be dense enough, dimensions of a plasma L must be much larger than the Debye length λ_D ($L \gg \lambda_D$),
- The number of particles within the Debye sphere must be much greater than one to fulfil the requirement of collective behaviour ($N_D \ggg 1$),
- The last requirement can be derived by considering ω_p as the frequency of the plasma oscillation and τ as the mean time between collisions with neutral atoms. The product of the plasma frequency and the collision time needs to be larger than one ($\omega_p \tau > 1$).

2.3 Ionisation processes

To understand the phenomena which are playing a significant role in laser plasma interaction, the dynamics of the interaction between light and matter and how the plasma state is reached needs to be analysed. For the approach of describing the processes, mainly reference [36] was used.
In the following, the simple example of the hydrogen atom is going to be used to describe the relevant processes. From the Bohr model of the hydrogen atom, a threshold for the laser intensity to induce ionisation can be derived. The Bohr radius is defined as:

$$a_B = \frac{4\pi\varepsilon_0\hbar^2}{m_e c^2} \approx 5.3 \times 10^{-9}\text{cm}, \tag{2.3.1}$$

where $\hbar$ is the reduced Planck constant $\hbar = \frac{h}{2\pi}$. The electric field of the laser needs to reach and overcome the Coulomb binding potential between the electron and the nucleus of the hydrogen atom which is given by

$$E_a = \frac{e}{4\pi\varepsilon_0 a_B^2} \cong 5.1 \times 10^9\text{V/m}. \tag{2.3.2}$$

Photoionisation
The above mentioned field strength corresponds the atomic intensity

$$I_a = \frac{\varepsilon_0 c E_a^2}{2} \cong 3.51 \times 10^{16}\,\text{W/cm}^2, \tag{2.3.3}$$

which is the intensity at which the laser field is equal to the binding strength of an electron to the atom. In order to ionise an atom, the laser intensity I_L needs to exceed the atomic intensity I_a. One atom can absorb one single photon with high frequency, as can also be observed during the photoionisation process, or several photons with lower frequency, respectively. In 1905, Einstein postulated that one atom or molecule ionises by absorbing electromagnetic radiation. If the energy of the photon is higher than the ionisation energy of the particle E_{ion}, ionisation can take place. The ionisation energy is given by:

$$E_{ion} = h\nu - E_{kin}, \tag{2.3.4}$$

where the excess energy is being released as kinetic energy E_{kin} of the free electron.

Multiphoton-ionisation
Usually the energy of one photon is not enough to ionise the irradiated material.

For example, using a wavelength of 800 nm photon energies of approximately 1.55 eV can be reached. Comparing this energy to the ionisation energy of the hydrogen atom (13.6 eV), it can directly seen that the energy of one single photon is not enough and almost one order of magnitude less than needed to ionise the atom. However, the ionisation process can take place way under this threshold via multiphoton-ionisation.
The ionisation probability strongly depends on the light intensity or particularly on the photon density. The n-photon ionisation rate is given by:

$$\Gamma_n = \sigma_n I_L^n. \tag{2.3.5}$$

The cross section σ_n obviously decreases with the amount of photons n, but the I_L^n-dependence guarantees that ionisation of nth-order can occur.
An electron can escape from the atomic nucleus if it gets enough energy for the transition from the ground state to an excited state (cf. figure 2.5). At intensities

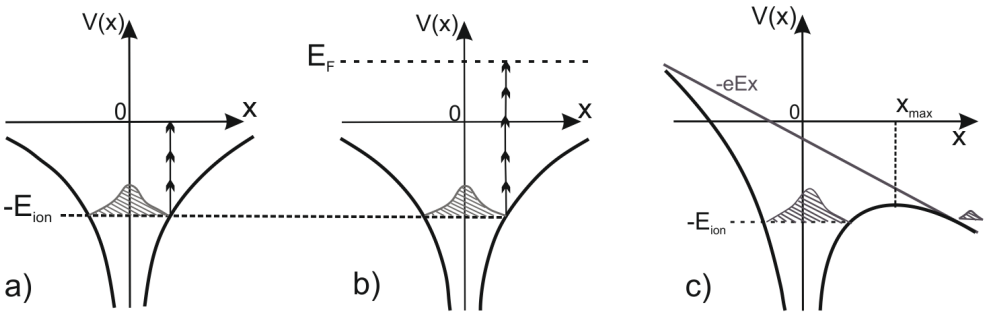

Figure 2.5: a) Schematic representation of multiphoton-ionisation. An electron with binding energy E_{ion} absorbs n photons with energy $\hbar\omega$. Subsequently it can be released from the atom. b) In the middle part of the figure the schematic representation of the above threshold ionisation is shown. Here, one electron absorbs more photons than needed for ionisation. c) Schematic representation of tunnel ionisation. The electron is able to tunnel through the potential barrier (cf.[36]).

$\gg 10^{10}$ W/cm^2, multiphoton-ionisation can be observed.

Above-threshold ionisation

At intensities up to approximately $>10^{14}$ W/cm^2, an electron can absorb more photons than needed for ionisation. In this case, electron energies far above the ionisation energy can occur, which would be expected during the interaction with one photon. This phenomenon is called above-threshold ionisation (ATI). The

kinetic energy of the electrons is given by an extended version of Einstein's formula:

$$E_f = (n+s)\hbar\omega - E_{ion}, \tag{2.3.6}$$

where n is the minimum number of photons which are required for the multiphoton-ionisation process and s the number of additionally absorbed photons.
Figure 2.5 a)-b) shows the multiphoton- and above-threshold ionisation in comparison. As can be seen in the figure, for ATI the number of photons absorbed by the electrons is much higher than needed for the ionisation process.

Tunnel ionisation

In case of multiphoton-ionisation, it can be assumed that the atomic binding potential is not disturbed by the laser field. In the high intensity regime, the laser field is strong enough to modify the Coulomb potential, thus lowering the binding energy. This allows an electron to overcome the Coulomb barrier. The effective Coulomb potential experienced by an electron at a distance x from the nucleus is given by

$$V(x) = -\frac{ze^2}{x} - eE_x. \tag{2.3.7}$$

During tunnel ionisation, the distance the electrons need to travel to overcome the Coulomb barrier decreases. This is true up to the point where the laser field is strong enough and the Coulomb potential gets distorted. Therefore, the quantum mechanical probability for electrons to tunnel through a potential barrier increases. Tunnel ionisation is the dominating process for intensities $>10^{15}$ W/cm^2.
For an atom of ionisation energy E_{ion}, the regimes of multiphoton- and tunnel ionisation are distinguished by the KELDYSH-parameter, which is defined as:

$$\gamma_K = \omega_L \sqrt{\frac{2E_{ion}}{I_L}} \tag{2.3.8}$$

where is ω_L the laser frequency and I_L the laser intensity. Tunnel ionisation outweighs for large wavelengths, high laser intensities and a KELDYSH-parameter of $\gamma_K < 1$, whereas multiphoton-ionisation dominates for $\gamma_K > 1$ [40]. In figure 2.5 c), the process of tunnel ionisation is presented. The Coulomb potential gets distorted and the distance for electrons to overcome the barrier decreases.

Barrier suppression ionisation

If the barrier falls under the binding energy E_{ion}, the electron can escape spontaneously, directly and without tunnelling. This is called over-the-barrier ionisation

or barrier suppression ionisation. This process is characterised by the appearance intensity:

$$I_{app} = \frac{\varepsilon_0 c}{2} E_c^2 = \frac{c\pi^2 \varepsilon_0^3}{2e^6} \frac{E_{ion}^4}{Z^4} \approx 4 \times 10^{19} \left(\frac{E_{ion}}{eV} \right)^4 Z^{-2} \, \mathrm{W/cm^2}. \tag{2.3.9}$$

This intensity corresponds to a threshold critical laser electric field $\mathrm{E}_c = \mathrm{E}_{ion}^2 / 4Ze^3$, at which the Coulomb potential is compensated. For the simplest case of hydrogen ($\mathrm{Z} = 1$, $\mathrm{E}_{ion} = 13.61$ eV), the appearance intensity is found to be $\mathrm{I}_{app}^H \approx 1.37 \times 10^{14}$ W/cm^2.

2.4 Absorption processes

Irradiating a target with a high intensity laser beam ionises the matter rapidly and at the surface of the target, a plasma emerges within a few laser cycles (cf. section 2.3). The subsequent interactions between laser and plasma strongly depend on the laser intensity. The energy absorption efficiency is essential for many effects and applications. Many different approaches of descriptions of absorption mechanisms were made in the last decades [41] [36].
For long pulses and rather moderate intensity regimes, collisional and classical collisionless resonance absorption are the main dominating absorption mechanisms. In ultrashort, high intensity laser pulse regimes, collisionless mechanisms such as $\vec{j} \times \vec{B}$ - heating and vacuum heating become relevant. In the following section, an overview of the most significant mechanisms will be given.

2.4.1 Propagation of electromagnetic waves

Absorption mechanisms play an important role in coupling the laser energy into an overdense plasma. In order to understand the energy coupling and the different absorption mechanisms, the propagation of electromagnetic waves in plasmas needs to be studied. For this purpose, Maxwell's equations are considered:

$$\begin{aligned} \vec{\nabla} \cdot \vec{E} &= \frac{\rho}{\epsilon_0} \\ \vec{\nabla} \cdot \vec{B} &= 0 \\ \vec{\nabla} \times \vec{E} &= -\frac{\partial \vec{B}}{\partial t} \\ \vec{\nabla} \times \vec{B} &= \mu_0 \vec{j} + \mu_0 \epsilon_0 \frac{\partial \vec{E}}{\partial t}. \end{aligned} \tag{2.4.1}$$

Furthermore, small field amplitudes and relativistic field dynamics are assumed. The motion of electrons is described by the Lorentz equation

$$m\frac{\partial \vec{v}}{\partial t} = -e\left(\vec{E} + \frac{\vec{v}}{c} \times \vec{B}\right) - m\nu_{ei}\vec{v}, \tag{2.4.2}$$

where ν_{ei} describes the electron-ion-collision frequency which is defined as

$$\nu_{ei} = \frac{4(2\pi)^2}{3}\frac{n_e Z e^4}{m^2 v_{te}^3} ln\Lambda. \tag{2.4.3}$$

Z defines the number of free electrons per atom, T_e the electron temperature and $ln\Lambda$ is the Coulomb logarithm, accounting for the limits of the electron-ion scattering cross-section. They are determined by the classical distance of the closest approach and the Debye length, respectively, leading to

$$\Lambda = \frac{b_{max}}{b_{min}} = \lambda_D \cdot \frac{k_B T_e}{Z e^2} = \frac{9 N_D}{Z}. \tag{2.4.4}$$

An induced current $\vec{J} = -en_0\vec{v} = \sigma_e \vec{E}$ is obtained, where the electrical conductivity σ_e is defined as $\sigma_e = \frac{i\omega p^2}{4\pi(\omega_L + i\nu_{ei})}$. Solving the Helmholtz equations, which result from Maxwell's equations, numerically [36]

$$\nabla^2 \cdot \vec{E} - \frac{1}{c^2}\frac{\partial^2 \vec{E}}{\partial t^2} = \mu_0 \frac{\partial \vec{J}}{\partial t} + \nabla(\nabla \cdot \vec{E}) \tag{2.4.5}$$

$$\nabla^2 \cdot \vec{B} - \frac{1}{c^2}\frac{\partial^2 \vec{B}}{\partial t^2} = -\mu_0 \nabla \times \vec{J} \tag{2.4.6}$$

the propagation of electromagnetic waves can be described. For a plane, transverse electromagnetic wave, the dispersion relation is defined as:

$$-k^2 + \frac{\omega^2}{c^2}\left(1 - \frac{\omega_p^2}{\omega_L^2(1 + \tilde{\nu_{ei}})}\right) = 0. \tag{2.4.7}$$

Arising thereby, a dielectric constant $\varepsilon \equiv \left(\frac{kc}{\omega_L}\right)^2$ is obtained, which is related to the refractive index $\varepsilon(x) = n^2(x)$.
Considering a plane wave incident on the density gradient of an inhomogeneous plasma, the propagation wave can be simplified to

$$\vec{E} = (0, 0, E_z e^{ikysin\theta}) \tag{2.4.8}$$

and the Helmholtz equation for the $\vec{E}$-field 2.4.1 reduces to

$$\frac{\partial^2 E_z}{\partial x^2} + k^2(\varepsilon - sin^2\theta)E_z = 0. \tag{2.4.9}$$

The electrical field is transverse to the plane of incidence, whereby the electrostatic coupling of s-polarised waves into the plasma is not possible. For p-polarised waves with $\vec{E} = (E_x, E_y, 0)$ and $\vec{E} = (0, 0, B_z)e^{ikysin\theta}$, there is a field component along the density gradient, which allows plasma waves to occur. The Helmholtz equation for the $\vec{B}$-field 2.4.1 reduces to the following form:

$$\frac{\partial^2 B_z}{\partial x^2} + \frac{1}{\varepsilon}\frac{\partial \varepsilon}{\partial x}\frac{\partial B}{\partial x}k^2(\varepsilon - sin^2\theta)B_z = 0. \tag{2.4.10}$$

For a slowly increasing density profile $kL \gg 1$ and a slowly changing dielectric constant $\varepsilon(x)$, the Helmholtz equations for the E- and B-field with the so-called Wentzel-Kramer-Brillouin (WKB) Approximation [36] can be solved. This approximation is only valid in the range of large scale lengths $kL \gg 1$. For femto-second-interactions, the reverse limiting case ($kL \ll 1$) is reached and the WKB-approximation cannot be used anymore. For large scale lengths, a solution for s-polarised light by using the WKB-approximation or resonance absorption for p-polarised light can be obtained. The latter one will be explained later in this section.

2.4.2 Absorption coefficient

Considering a step-like density gradient and assuming the plasma behaves like a metal surface with finite conductivity due to the effect of electron-ion collisions, Fresnel's law from metal optics can be used. Fresnel's equations for the reflectivity of s- and p-polarised light (R_s and R_p, respectively) are defined as [36]

$$R_s = \left|\frac{sin(\theta - \theta_t)}{sin(\theta + \theta_t)}\right|^2 \tag{2.4.11}$$

$$R_p = \left|\frac{tan(\theta - \theta_t)}{tan(\theta + \theta_t)}\right|^2, \tag{2.4.12}$$

where θ is the incidence angle and $\theta_t = sin^{-1}\{\frac{sin\theta}{n}\}$ the generalised, complex angle for transmitted light.
Furthermore the absorption fraction is given by

$$\eta = 1 - R. \tag{2.4.13}$$

For an arbitrary density profile, a solution by solving the Helmholtz equations can be directly found. This method is more general and leads to the same characteristic Fresnel behaviour for $\frac{L}{\lambda} \to 0$. The angular dependence of the absorption coefficient for different scale lengths is shown in figure 2.6. The main variable parameters are

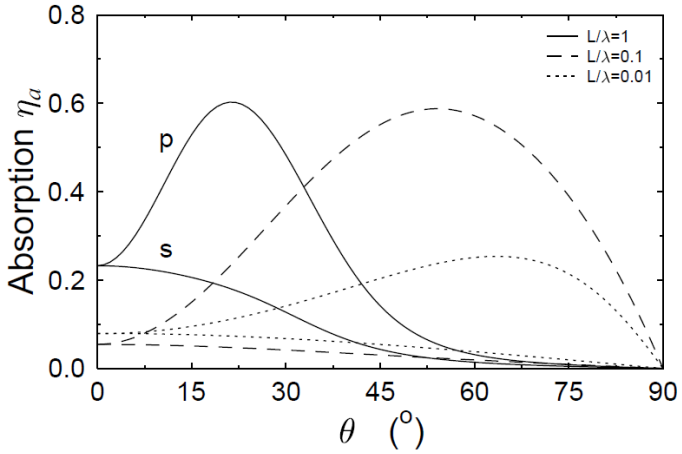

Figure 2.6: The absorption is depending on the angle. This figure shows the dependence for different scale lenghts (The following scale lengths are shown in the figure: solid line $\frac{l}{\lambda} = 1$, dashed line $\frac{l}{\lambda} = 0.1$, dotted line $\frac{l}{\lambda} = 0.01$) [36].

the scale length, the collision frequency and the angle of incidence. For a given scale length, a characteristic angular dependence of the absorption can be found. An optimum absorption for p-polarised light can be achieved for an incident angle which is getting larger with an increasing density gradient.

Collisional absorption

At very high energies, which are for example needed for laser-fusion, multiphoton effects become important. Due to oscillations in the laser field, an electron is able to absorb the laser energy. Collisions with ions lead to absorption. In the nanosecond regime, Inverse Bremsstrahlung is the dominating process with a typical scale length of $L/\lambda \sim 100$. At intensities between 10^{12}-10^{14} W/cm^2, collisions dominate the absorption mechanism. The density profile of the plasma is the main parameter determining the absorption mechanism. At a steep density profile, the laser field can propagate to much higher densities. In this regime, the plasma in general is highly collisional. Inverse Bremsstrahlung is one of the significant mechanisms for transporting laser light energy into matter. It appears that for high particle temperatures, collisions become inefficient and do not contribute to the absorption mechanism. In the picosecond regime, lengths in the region of $L/\lambda \leq 1$ would be

expected [42] [43].
The absorption coefficient for collisional absorption and s-polarised light for an exponential profile is givenby [38] :

$$\eta_{coll} = 1 - exp\left(-\frac{8\nu_{ei}L}{3c}cos^3\theta\right). \tag{2.4.14}$$

Inverse Bremsstrahlung

As long as the electrons oscillate in phase with the laser pulse, absorption cannot take place. If electrons collide with ions or atoms, they will get out of phase and their oscillation energy will be transferred to thermal energy. The absorption coefficient for Inverse Bremsstrahlung scales with

$$\eta_{IB} \sim \frac{n_e^2 Z}{T_e^{3/2}\sqrt{1-\frac{n_e}{n_c}}}. \tag{2.4.15}$$

As can be seen, the absorption is highest for high densities, highly charged ions, low temperatures and short wavelength laser light. If the medium is heating up, the absorption will cease. As the plasma temperature rises very fast, collisions become less efficient during the interaction.

Resonance absorption

The electron-ion-collision frequency decreases with increasing laser intensity ($I_L > 10^{15}$ W/cm^2). Hence, the collisional absorption mechanisms become inefficient and collisionless mechanisms become dominant [44].
In the standard picture, a p-polarised wave can tunnel up to the critical surface ($n_e = n_c$). Also, regarding the mathematical description by considering the solution of Maxwell's equations for p-polarised light incident on a steep-density gradient plasma at an oblique incidence angle, a singularity in the magnitude of the oscillating electric field can be seen [45] [46] [47]. This electric field can resonantly drive up a plasma wave. Over a number of laser periods, the plasma wave grows and is damped either by particle trapping and wave breaking at high intensities or collisions at low intensities [38].
The main feature of resonance absorption is the creation of hot electrons. In contrast to Inverse Bremsstrahlung, where all the electrons are heated, only a small part of the electrons gain most of the absorbed energy.
If a strong laser pulse is obliquely incident on a overcritical plasma, the electrons start oscillating resonantly at the critical density n_c with a velocity of $v_{os} = \frac{eE}{m\omega}$

(quiver velocity). The quiver velocity becomes comparable to the thermal velocity. Light which is able to tunnel through the plasma drives up a plasma wave. The basic principle of the resonance absorption is shown in figure 2.7. A wave incident

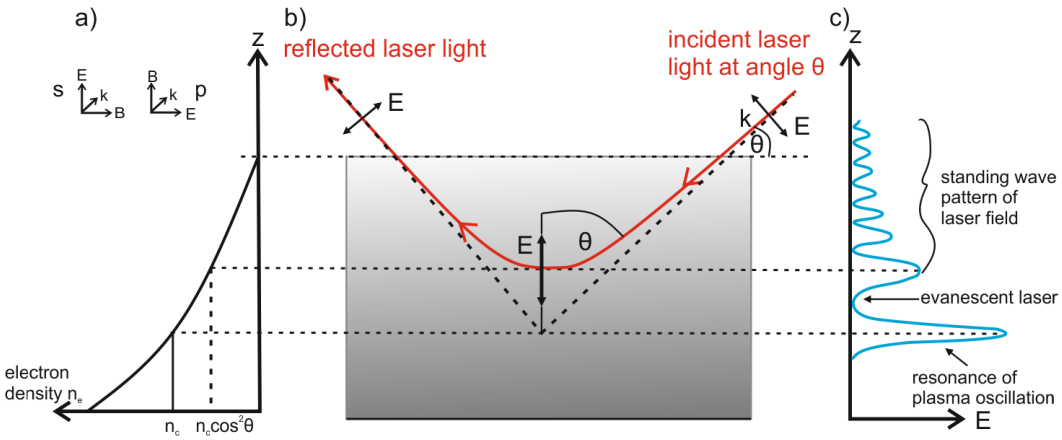

Figure 2.7: Geometry of a plane wave incident on a plasma density profile. The figure shows the standard schematic illustration of resonance absorption (b). A p-polarised wave tunnels through the critical density n_c and a plasma wave arises [36] [37]. The corresponding electron density is shown in (a) and the electric field in the plasma in (c), respectively.

on the plasma at an angle of θ will be refracted due to the density gradient. If the density gradient is smaller than the critical density, the incident wave will already be reflected at $n_e(\theta) = n_c cos^2(\theta)$. P-polarised light has an electric field component parallel to the plane of incidence. The electric field is in the plane which is built up by the k-vector and the density gradient. In this case, the electrical field is parallel to the density gradient at the *turning point*. A part of the electrical field can tunnel through the density gradient up to the critical density where it eventually resonantly drives a plasma wave. The resonance absorption is effective even if the electron-ion collision frequency ν_{ei} is small, since the damping of the plasma wave is possible by collision or collisionless processes [37].

If the electric field is perpendicular to the plane of incidence (s-polarised), there will be no component along the density gradient and therefore no plasma wave can emerge. For large angles of incidence θ, the surface of reflection is too far away from the critical surface and the area for tunnelling becomes too large. However, if the angle is too small, the component of the electric field along the density gradient will also be too small. Therefore, resonant electron oscillations are not possible anymore.

The optimum angle of incidence can be obtained by maximising the Denisov-

function. The angular dependent behaviour is shown in figure 2.8. For large scale

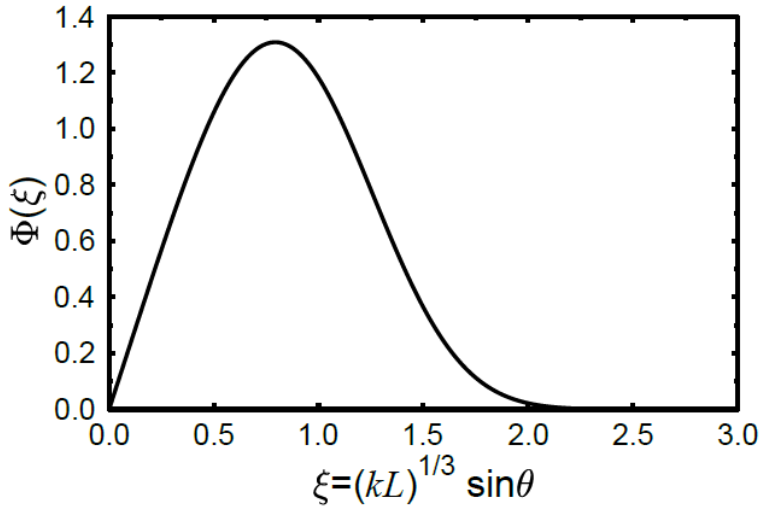

Figure 2.8: For high scale lengths the Denisov-funtion is a good approximation for the behaviour of resonance absorption. The Denisov-function is plotted against the parameter ξ [36].

lengths ($kL \gg 1$), the absorption is depending on the parameter $\xi = (kL)^{1/3} sin\theta$, where θ is the angle of incidence.
A good approximation for the Denisov-function is given by:

$$\phi(\xi) \cong 2.3\xi exp(-2\xi^3/3). \tag{2.4.16}$$

For the optimum angle of incidence

$$sin\theta_{max} \approx 0.8(c/\omega L)^{1/3} \tag{2.4.17}$$

one can get maximum absorption of about 60% [36]. With a steep density profile, which can occur at high laser intensities, short pulses and good contrast, the distance for tunnelling to reach the critical density gets smaller [36].
The absorption coefficient for resonance absorption is given by

$$\eta_R A = \frac{1}{2}\phi^2(\xi) \tag{2.4.18}$$

If a small pump-amplitude is provided, this absorption behaviour is more or less independent of the damping mechanism.

Vacuum heating
At very steep density gradients, resonance absorption ceases to work in its usual

way. To illustrate this, a plasma wave with a field amplitude E_p which is resonantly driven at the critical density can be considered. In a sharp-edged density profile, the field amplitude roughly matches with the amplitude of the incident laser field E_L. The electrons oscillate along the density gradient with an amplitude of $x_p \simeq eE_L/m_e\omega^2 = v_{os}/\omega$. If the amplitude is larger than the scale length ($v_{os}/\omega > L$), the resonance breaks down. Electrons near the edge of abrupt change in the plasma-vacuum interface will directly be exposed to the laser field. If an electron is in the laser cycle near this interface at the right moment, the electron can be dragged out far beyond the boundary layer, the so-called Debye sheath. The Debye sheath is determined by the Debye length. As soon as the field reverses its direction, the electron will be accelerated back into the plasma. Since the plasma is highly overdense, the electric field can just penetrate to the skin depth $\sim c/\omega_p$. This mechanism has the most significant contribution if the plasma density is way above the critical density [44] [48].

For this "not-so-resonant, resonant"-absorption, F. Brunel developed an analytical model (cf. [49]). To describe this mechanism, the simple case of a one-dimensional condensator is considered. The magnetic field of the plasma is neglected. Furthermore, it is assumed that the electric field of the laser E_L has a component E_d normal to the target surface. This component accelerated the electrons back and forth beyond their equilibrium state. If the wave is incident at an angle θ on a plane, reflective surface, the driving electric field can be described as $E_d = 2E_L sin\theta$. The electrons are accelerated out of the plasma with a velocity of $v_d = \frac{eE_d}{m_e\omega} \simeq 2v_{os}sin\theta$. At low intensities, for the absorption coefficient

$$\eta_{VH}^{low} = \frac{a_0}{2\pi} f^3 \alpha(\theta), \tag{2.4.19}$$

with $a_0 = \frac{v_{osc}}{c}$, $\alpha(\theta) = \frac{sin^3(\theta)}{cos\theta}$ and $f = \frac{4}{\pi} a_0 \alpha(\theta)$ is obtained.
At higher intensities, in the relativistic regime ($f a_0 sin\theta \gg 1$), the absorption coefficient scales with

$$\eta_{VH}^{rel} = \frac{f^2}{\pi} \frac{\alpha(\theta)}{sin\theta}. \tag{2.4.20}$$

In the intensity regime between $I\lambda^2 = 10^{16}$-10^{18} Wcm$^{-2}\mu$ m^2, Vacuum Heating is the dominating process at oblique incidence. At high radiation intensities and small scale lengths, absorption already saturates at 10-15%. However at an intermediate intensity regime, for example at an intensity of $I\lambda^2 = 10^{16}$ Wcm$^{-2}\mu$ m^2 and a scale length of $\frac{L}{\lambda} \sim 0.1$, an absorption rate of about 70% is obtained [36].

Sheath inverse Bremsstrahlung

The anomalous skin effect as well as the sheath inverse Bremsstrahlung are both limiting cases of the same collisionless absorption mechanism. In the regime $\omega^2 c^2 \gg \omega_p^2 v_e^2$, the sheath inverse Bremsstrahlung and in the regime $\omega^e c^2 \ll \omega_p^e v_e^2$, the anomalous skin effect are the dominating process. Other than in the anomalous skin effect process, the electron transit time trough the skin depth is larger than one laser period. Both mechanisms are complementary to vacuum heating [50] [51]. Classical inverse Bremsstrahlung is ineffective for high energetic electrons. At higher velocities, the sheath inverse-Bremsstrahlung becomes more effective. The sheath inverse-Bremsstrahlung model, which was first established in 1977 by P.J. Catto and R. M. More, can be modified by adding a $\vec{v} \times \vec{B}$-term in the equation of motion, and thus the shrinking magnetic field becomes larger than the complementary electric field. Without this $\vec{v} \times \vec{B}$-term, the absorption is mistakenly interpreted as the electron temperature [51]. In an analytical way, the absorption coefficient can be expressed as:

$$\eta_{sib} = \frac{8}{\sqrt{2\pi}} \frac{v_{te}}{c} \frac{a[(a+1)exp(a)E_1(a) - 1]}{0.5 + \frac{\sqrt{\pi a}}{2} exp(a) erfc(a^{1/2})}, \tag{2.4.21}$$

with $a = \frac{\omega^2 l_s^2}{2 v_{te}^2}$, $E_1(a) = \int_a^\infty \frac{\exp(-t^2)}{t}\,\mathrm{d}t$.

For most applications, the absorption rate is not particularly high for normal incidence. Considering two plasma layers with each a temperature of 5 keV and electron densities of $\frac{n_e}{n_c} = 5$ and 400, for the first case sheath inverse-Bremsstrahlung and for the latter one the anomalous skin effect outweighs. In both cases, the absorption is about 5%. [36]. This can be increased at oblique incident.

$\vec{j} \times \vec{B}$-Heating

Another collisionless absorption mechanism which is similar to Vacuum Heating is the $\vec{j} \times \vec{B}$-heating mechanism. Like in the Vacuum Heating mechanism case, electrons are directly accelerated by the laser field. The driving factor is given by the $\vec{v} \times \vec{B}$ component of the Lorentz force. The magnetic force is no longer negligible, which is the main difference between both mechanisms. In 2.9 both mechanisms are illustrated in comparison. Electrons are accelerated in different directions. With a linearly polarised electromagnetic wave and a field amplitude of $E = E_0 = \hat{y} sin\omega t$, the longitudinal force is obtained by[52]:

$$f_P = -\frac{m}{4} \frac{\partial v_{os}^2}{\partial x} (1 - cos2\omega t). \tag{2.4.22}$$

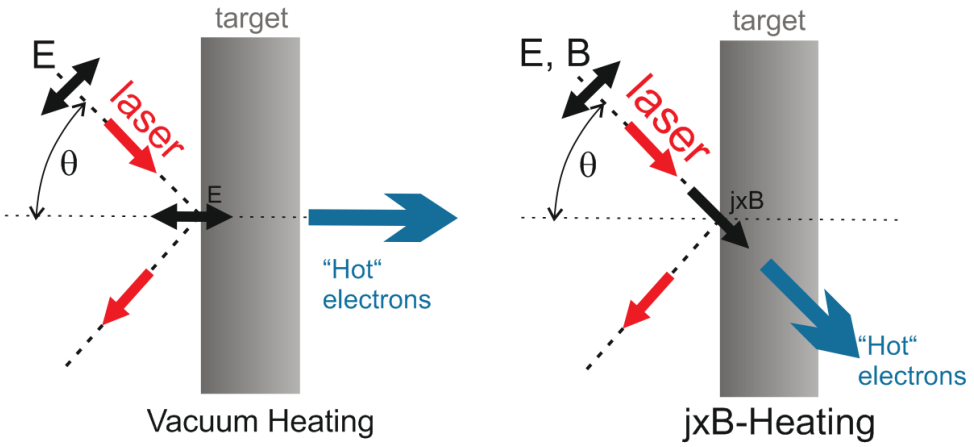

Figure 2.9: The figure shows a comparison between the vacuum heating (left) and the $\vec{v} \times \vec{B}$-Heating (right). The main difference is the direction of hot electrons (cf. [53]).

The first term on the right-hand-side represents the ponderomotive force, which is driving the electrons in the direction of the laser. The second high frequent term leads to a $\vec{j} \times \vec{B}$-term similar to the component parallel to the density gradient of a p-polarised electrical field. This component is only present for p- and s-polarised, but not for circularly polarised light and is most effective for normal incidence. The electrons are heated by the damping of the longitudinal oscillation. The $\vec{j} \times \vec{B}$-heating mechanism is including two different processes, depending on the initial conditions of the laser and the plasma. At moderate intensities, the ponderomotive force of the laser light can generate a great, resonant plasma wave at $n_e = 4\gamma n_c$. This energy is transferred to the plasma during the damping process. The resonance is ceasing for $n_e > 4\gamma n_c$, but the longitudinal component of the oscillation can lead to an absorption mechanism similar to Vacuum Heating [54].
The absorption in this regime can be estimated by:

$$\eta_{\vec{j}\times\vec{B}} = \frac{\gamma_{osc} - 1}{\pi a_0^2} N_a, \tag{2.4.23}$$

where $N_a = 2\int_{\xi_a}^{\xi_b} N_e(\xi)\,\mathrm{d}\xi$ gives the number of electrons extracted out of the density profile.
The deeper the electromagnetic wave can penetrate into the plasma, the more absorption can occur. With increasing skin depth (i.e. decreasing density and increasing intensity), the absorption is increasing. Since the ponderomotive force is modifying the density profile very fast, the skin depth and absorption rate are not

changing considerably.
At very high intensities, the $\vec{j} \times \vec{B}$-heating mechanism is the dominating process and can lead to absorption rates up to 90 % [55].

2.5 Ion acceleration by laser-plasma interaction

Since the development of the CPA technique, reaching intensities well above 10^{18} W/cm^2 on the target became possible. In this relativistic laser-plasma interaction regime, many opportunities for discovering highly interesting and new physical phenomena arise. Among these, the acceleration of high energy proton beams [20] [10] [56] has been one of the most attractive research areas. Contrary to earlier experiments [57] [58], protons are accelerated in forward direction. The characteristics of the forward emission of protons, such as high brightness, high degree of collimation and laminarity and high spectral cut-off arouses interest in fundamental research and potential applications. These include, for example, cancer therapy, plasma probing by laser-driven proton beams [14] [33], fast ignition and inertial confinement fusion [15].
In the following, the main acceleration mechanisms and physical properties of accelerated ion beams will be discussed.

2.5.1 Front and rear surface acceleration

Electrons generated during laser-plasma interaction are accelerated forward inside of the target. Due to a charge separation by a collective displacement of electrons, strong and quasi-static fields arise. These fields accelerate ions until charge neutrality is restored again. As soon as charge neutrality is re-established again, ions and electrons will move together in a ballistic way [59].
Besides the investigation of the driving acceleration mechanism, an argument about the actual region where the ions are accelerated arose.

Front surface acceleration/Radiation Pressure Acceleration
Different research groups independently published the discovery of proton beams with multi-MeV energy around the same time [56] [20] [60]. Since then, many other experimental work, reported a forward accelerated proton beam being emitted along the target normal irrespective of the angle of incidence of the laser beam on the target.
The origin of the radiation pressure lies in the momentum of the electromagnetic

wave which is delivered to a nontrasparent medium. For a plane monochromatic electromagnetic wave, the radiation pressure is given by [59]:

$$P_{rad} = (1 + R - T)\frac{I}{c} = (2R + A)\frac{I}{c}, \tag{2.5.1}$$

where R, T and A are the reflection, transmission and absorption coefficient, respectively. An electrostatic field which acts on the ions and accelerates them is created.
Analytical models show that the final ion energy should scale with $\sim (I\tau/\sigma)^{\alpha}$, where I is the laser intensity, τ the pulse duration and σ the areal mass of the target. The exponent α, is found to be $\alpha = 2$ for $v_{final} \ll c$ and $\alpha \to \frac{1}{3}$ in the ultrarelativistic regime [61].
The mechanism clearly changes for circularly polarised light. The oscillating component of the $\vec{j} \times \vec{B}$-force vanishes, thus suppressing the heating of electrons. The electrons are mostly, on a time scale of ion motion, in a mechanical equilibrium, thus the electrostatic and ponderomotive force balancing each other. The ions are accelerated by a compressed, dense electron layer. If the radiation pressure equals the restoring force given by the charge separation field, electrons and ions propagate balistically as a quasineutral plasma bunch [28]. Depending on the target thickness, two different regimes can be identified.

Hole boring regime

At the front surface of the target, the density profile is steepening as the target is pushed inwards and the surface is bend by the intense radiation pressure of the laser pulse. Commonly, this process is called *hole boring*. Note that different definitions such as "*sweeping acceleration* "[25] or "*laser piston*" [62] are also used. The process of the electron sweeping is shown in figure 2.10.
The hole boring velocity can be estimated by balancing the electromagnetic and mass momentum flows [59], which yields for the hole boring velocity and hole boring time respectively:

$$v_{HB} = \sqrt{\frac{I}{cn_i m_i}}, \quad t_{HB} = \frac{d}{v_{HB}}, \tag{2.5.2}$$

where d stands for the target thickness and $n_{mi}m_i = \rho$ for the target density.
Considering a dynamical model [63], simulations show that ions pile up into a compressed layer at the end of the skin layer and produce a sharp density spike. The electron equilibrium collapses and leads to the production of fast ions. These

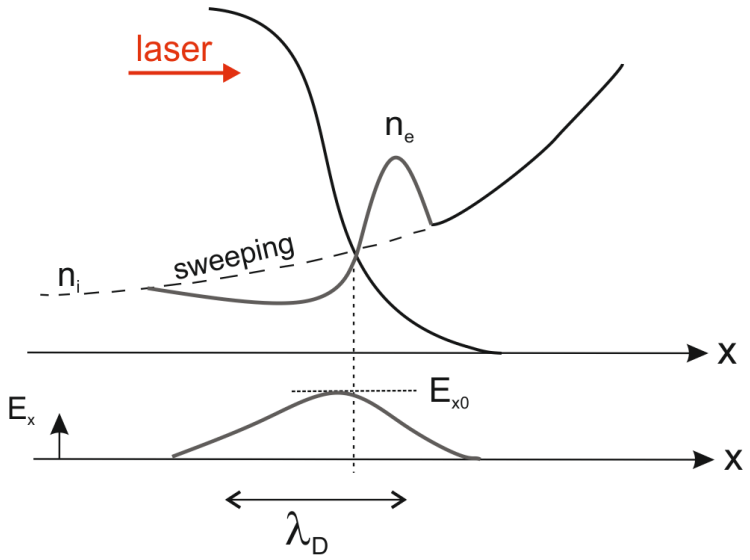

Figure 2.10: An illustration of the electron sweeping. The sweeping length is close to the Debye length λ_D (cf. [25]).

electrons penetrate into the plasma bulk with a velocity of v_{HB}. Eventually, the quasiequilibrium is restored again and the whole process repeats itself.
The proton energy can be scaled as a function of expected energy due to hole boring: $E = \frac{1}{2}m(2v_{HB})^2 = 4I/nc$, with density n and laser intensity I, as mentioned in [64]. The ion energy is found to scale linearly with increasing I/n.

Light sail regime

The hole boring regime discussed above applies for thick targets, i.e. for target thicknesses larger than the skin layer. If the target is thin enough, all ions are accelerated before the end of the laser pulse (complete hole boring). The ions are not screened by a background plasma like in the hole boring regime, thus accelerating more ions to higher energies. In other words, the light sail regime applies for targets thin enough to be accelerated as a whole. For long enough pulse durations $v_{HB}\tau > \ell$, with ℓ the target thickness, the hole boring through the target is complete and all ions are displaced [29]. The main characteristics of the light sail regime are the monoenergetic ion spectrum and the possibility to reach high ion energies.
For a thin target, the radiation pressure at normal incidence, neglecting absorption is given by:

$$P = 2R\frac{I}{c}. \tag{2.5.3}$$

Note that radiation pressure vanishes for R = 0, which is different from the thick

target case.
In a laboratory frame for the equation of motion of thin targets, the following equation is obtained [29][65]

$$\frac{d}{dt}(\beta\gamma) = \frac{2I(t_{rit})}{m_i n_i \ell c}\frac{1-\beta}{1+\beta}R(\omega'), \tag{2.5.4}$$

where $\beta = v/c$ is the velocity of the foil in units of the speed of light, $\omega' = \omega\sqrt{(1-\beta)/(1+\beta)}$ the frequency in the rest frame and t_{rit} the retarded time at the foil position.
The solution for the final foil velocity at perfect reflectivity (R = 1) is found to be:

$$\beta = \frac{[1+\varepsilon]^2 - 1}{[1+\varepsilon]^2 + 1}, \varepsilon \simeq 2\pi\frac{Z}{A}\frac{m_e}{m_p}\frac{a_0^2\tau}{\xi}, \tag{2.5.5}$$

with the surface density $\xi = \pi(n_e/n_c)(\ell/\lambda)$.
As discussed in [66], the light sail stage will dominate for thin targets and high intensities. Since in this regime $t_{HB} \ll t_L \simeq t_{LS}$,the efficiency of the light sail stage is higher with respect to hole boring. In this case, the ion energy is scaling quadratically as in $E_{ion} \sim \left(a_0^2 \frac{ct_L}{\lambda}/\xi\right)^2$ with $\xi = \frac{\ell\varrho/m_p n_c}{\lambda}$.
However, there are a number of effects limiting the energy transfer from the laser to the ions [67]. One of the limiting effects is the target transparency. In order to transfer the energy from the laser to the target efficiently, the target should remain opaque for radiation during the acceleration process. However, opaque foils have high densities and/or are rather thick, which increases the number of ions in the irradiated spot and decreases the laser energy transfer per ion. Therefore, the acceleration should be performed at the threshold of the foil transparency/opacity, which is given by the reflection coefficient. At this threshold, the opaqueness of the foil is ensured by a minimum number of ions. Thus, the condition for optimal acceleration was found to be $a(t) = \gamma(t)\epsilon_p(t)$, where $\epsilon_P = \frac{2\pi e^2 n_e l}{m_e \omega c}$ denotes the normalised surface density [67] [68]. Another limiting effect is the laser group velocity. If the effect of the laser group velocity is taken into account, the energy gain is proportional to the difference between the instantaneous foil velocity and the laser group velocity. Note that a laser pulse cannot accelerate a foil to velocities larger than its group velocity [68] [68]. Also the transverse target expansion needs to be taken into account. The target areal density is decreased by the diffraction of the tightly focused laser pulse, which terminates the acceleration. Another limiting factor is the angle of incidence of the laser pulse. Usually, off-normal incidence is

used in the experiments in order to reduce the probability of damaging the laser system by reflected light. The maximum ion velocity is given by $v_{max} = v_g cos(\theta)$, where v_g is the group velocity of the laser pulse and θ the incidence angle. At some point during the interaction, the longitudinal component of the electromagnetic wave vector vanishes due to the large foil velocity, which is giving the limiting factor for the maximum velocity. The limiting factors are reviewed in more detailed way in [67].

Rear surface acceleration

Target Normal Sheath Acceleration

The origin of the **T**arget **N**ormal **S**heath **A**cceleration (TNSA) is found to be a large charge separation generated by hot electrons heated by the laser and reaching the rear side of the target. A cloud of relativistic electrons is formed, penetrating and extending out of the target for several Debye lengths. Due to the target's capacitance, only a small part of the electrons can escape before the target is sufficiently charged [69]. The electrons which cannot escape are electrostatically confined and move back and forth through the target. An extremely intense electric field of the order of several teravolts per metre is formed on both sides of the target. At the rear surface, there is no screening plasma. Ions are accelerated perpendicularly to the surface. The electric field generated at the rear side of the target depends on the properties of the electron distribution, electron temperature, number of electrons, divergence and as well as on the density profile of the surface. Particle-in-cell simulations [21] [70] indicate that the hot electron temperature scales with the ponderomotive potential and is given by the cycle averaged oscillation energy in the laser field [59] [71] [72]

$$\begin{aligned} T_{hot} &\cong mc^2(\gamma - 1) = mc^2 \left(\sqrt{1 + a_0^2/2} - 1 \right) \\ &\approx mc^2(1 + (1 + I\lambda^2/1.37 \times 10^{18})^{1/2} - 1). \end{aligned} \tag{2.5.6}$$

Only a fraction of the laser energy is converted to hot electrons

$$n_0 = \frac{\eta E_L}{c\tau_L \pi r_0^2 k_B T_{hot}}. \tag{2.5.7}$$

The number of electrons is following a scaling with the intensity [71]:

$$\eta = 1.2 \times 10^{-15} I^{0.74}. \tag{2.5.8}$$

The electron density at the rear side of the target strongly depends on the laser intensity and is inversely proportional to the square of the target thickness

$$n_{e,0} = \frac{\eta E_L}{c\tau_L \pi (r_0 + dtan\theta/2)^2 k_B T_{hot}}, \tag{2.5.9}$$

where r_0 denotes the laser spot radius, d the target thickness and θ the broadening angle of the distribution.
When the electrons reach the rear side of the target, the much more inert ions provide a positive charge, creating a charge separation sheath which leads to the accelerating field. Protons are accelerated most efficiently, but the heavier ions can also be accelerated effectively on a longer time scale, if the number of protons is not high enough to compensate the charge of the escaping electrons. A schematic

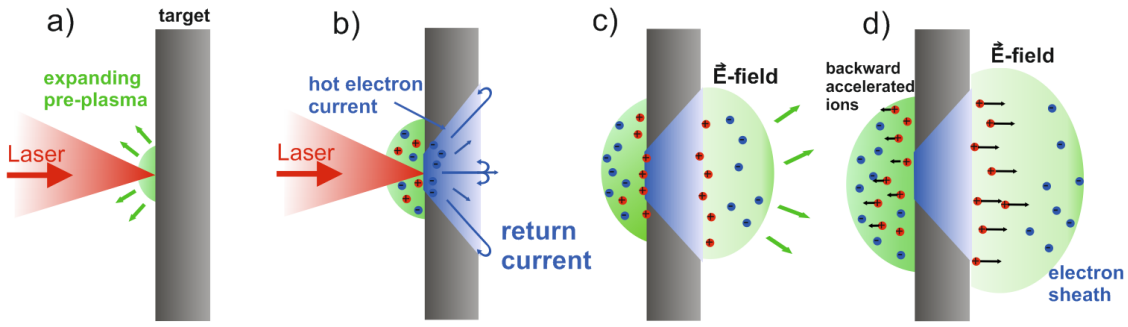

Figure 2.11: Schematic representation of the Target Normal Sheath Acceleration. a) A laser pulse is impinging on a solid thin foil target (i.e. 5 - 50 µm) and due to the prepulse of the laser, a pre-plasma is generated. b) Hot electrons are generated and pushed towards the rear side of the target. c) An electric field is built up due to the charge separation. d) The electric field is strong enough to accelerate the ions (or protons from a contamination layer) normal to the target.

description of the Target Normal Sheath Acceleration is shown in figure 2.11.
Snavely et al. [11] have already shown that the ions are emitted normal to the rear surface of the target. The maximum cutoff energy of the protons can be calculated as denoted in [71]:

$$E_{max} = 2T_{hot}\left[ln(t_p + (t_p^2 + 1)^{1/2}\right]^2, \tag{2.5.10}$$

where $t_p = \omega_{pi} t_{acc}/\sqrt{2exp}$ is the normalised acceleration time and $\omega_{pi} = \sqrt{n_{e0}Ze^2/\epsilon_0 m_p}$ the ion plasma frequency. The effective acceleration time (or limit time) is found to be $t_{acc} \sim 1.3\tau_L$ [71].

2.6 Relativistic Effects

Almost instantly after the first demonstration of a laser in the early 1960s, nonlinear effects were observed. Electromagnetic field intensities exceeding 10^{18} W/cm^2 lead to relativistic electron motion in the laser field, where $eE_0\lambda > 2\pi m_e c^2$. In this relativistic regime, matter can be moved more effectively and most importantly in the direction of laser propagation [73]. These relativistic phenomena can be utilised for various applications, e.g. the fast ignition of an inertially confined fusion target by a short laser pulse [74] [16].
In the following, the two most relevant effects for the experiments carried out in this thesis will be presented. First of all, the effects and conditions for relativistic transparency will be discussed and secondly, the condition for relativistic self-focusing will be described.

2.6.1 Relativistic Transparency

Overdense plasmas are generally opaque for laser light. The plasma reflects the laser light, because the plasma density is higher than the critical density. However, if the intensity is high enough to accelerate the electrons close to the speed of light, the mass increases by the Lorentz-factor $\gamma = \sqrt{1 - \frac{v^2}{c^2}}$, whereby the laser light observes a reduced plasma density of $\frac{n_e}{\gamma}$. The plasma becomes transparent. This process takes place within a few picoseconds [35].
Due to a change in the plasma density, the reflective index changes to $n = \sqrt{1 - \frac{n_e}{\gamma n_c}}$. At the same time, the electron density decreases because of the expansion of the plasma layer. This fulfils the condition for relativistic transparency. It determines that the effective plasma density has to be smaller than the critical density ($\frac{n_e}{\gamma} \leq n_c$) [75] [76]. Optically, the plasma changes from opaque to transparent, whereby it enables the propagation of light. The increasing mass is slowing down the motion of the electrons in such a way that they cannot shield the plasma from the incident light any more.
The effect of relativistic transparency can be seen in the reflected, as well as in the transmitted intensity profile of the laser. Considering the incident temporal profile, a temporal limit can be observed [35]. In figure 2.12, the schematic representation of the relativistic transparency is shown. An electromagnetic wave can propagate through a plasma, if the displacement current is higher than the plasma current. For intensities smaller than the limit for penetration of electromagnetic fields, the underdense plasma is fully reflecting the radiation. For higher intensities, the

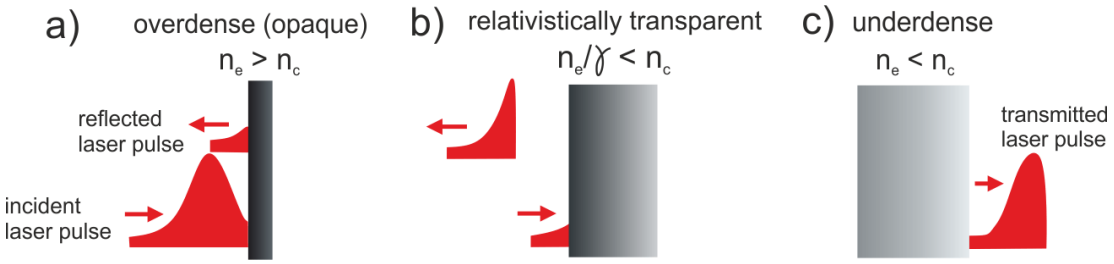

Figure 2.12: Schematic representation of the relativistic transparency. a) The incident laser pulse is heating the medium and an overdense plasma is generated. The laser pulse is reflected by the overdense plasma. b) The criterion for relativistic transparency is fulfilled and the laser pulse can propagate through the medium. c) Further expansion of the plasma leads to an underdense plasma (cf. [35]).

electromagnetic wave is propagating in form of non-linear plane waves.
In the non-relativistic regime, the electromagnetic wave can propagate under the condition $\omega > \omega_p$. If the electromagnetic wave is strong enough, the electrons will be accelerated to relativistic velocities, thus modifying the plasma frequency by relativistic effects depending on polarisation of the wave.
Since in the relativistic regime the mass of the electrons is increasing and at the same time the plasma frequency is decreasing, it is possible for intense electromagnetic fields to propagate through an overcritical plasma. For a circularly polarised wave, the $\vec{v}\times\vec{B}$-term of the dispersion relation can be neglected and the absolute values of the electric field strength and the electron velocities stay constant. The dispersion relation is given by

$$\omega^2 = \frac{\omega_p^2}{\gamma} + k^2c^2. \tag{2.6.1}$$

The propagation of an electromagnetic wave in the relativistic case is only possible if $\omega^2 > \frac{\omega_p^2}{\gamma}$.
For a linearly polarised wave, the $\vec{v}\times\vec{B}$-term must be compensated by the term which is created by the electrostatic field. The condition for transparency is $\omega^2 > 4\omega_p^2/\pi a$, where a gives the electric field strength.
In relativistic regimes, the propagation of electromagnetic waves in underdense plasmas is possible, if the field strength is exceeding a certain limit. For circularly and linearly polarised waves, the conditions are given as follows:

$$a_{circ}^2 = \left(\frac{n_e}{n_c}\right)^2 - 1 \tag{2.6.2}$$

$$a_{lin} \approx \frac{4}{\pi}\frac{n_e}{n_c}. \tag{2.6.3}$$

If an electromagnetic wave is penetrating through a plasma, it is experiencing a discontinuity in the reflective index at the wave front. Behind the edge of the laser pulse, the Lorentz factor of the electrons is larger than in the undisturbed plasma. The discontinuity works like a mirror for the incident laser light which is then reflected with a Doppler shift. The refractive index is not constant anymore.

2.6.2 Relativistic self-focusing

Generally the laser intensity in the centre of the laser beam is higher than in the outer regions. As a consequence, the reflective index has its maximum on the laser axis ($\frac{d\eta}{dr} < 0$), which corresponds to a positive (or focusing) lens. Self-focusing occurs in a relativistic plasma because of a transverse gradient in the refractive index. The radial dependence of the refractive index is given by [36]:

$$\eta(r) \equiv \frac{ck}{\omega} = \sqrt{1 - \frac{\omega_p^2}{\omega^2[1 + a(r)^2/2]^{1/2}}}, \tag{2.6.4}$$

where *a(r)* gives the profile of the laser. At relativistic intensities, the phase velocity of the focusing laser beam in the plasma on the axis is slower, thus creating a velocity difference of $\frac{v_p(r)}{c} = \frac{\omega_p^2}{8\omega^2 a_0^2 e^{r^2/\sigma_0^2}}$. The phase velocity in the plasma is shown in figure 2.13. A limiting case for relativistic self-focusing is given by the critical power:

$$P_c = \frac{m_e c^5 \omega^2}{e^2 w_{pe}^2} \simeq 17 \left(\frac{\omega_0}{\omega_p}\right)^2 \text{GW}. \tag{2.6.5}$$

The laser pulse can be self focused over a distance greater than the Rayleigh length $Z_R = \frac{\pi\omega_0^2}{\lambda}$.

Relativistic self-focusing corresponds to an instability in the filament formation. In the weak relativistic case ($|a| \ll 1$), the condition for relativistic reflection is $P > P_{cr}$. For $P = P_{cr}$, the diffractive expansion of the laser beam is compensated by the radial inhomogeneity of the reflective index of the plasma which is created because of the relativistic increasing of the electron mass. For $P > P_{cr}$, the axial symmetric laser beam is becoming a field singularity within a short time duration of $t_{s-f} = \frac{ZR}{c}\sqrt{\frac{P}{P_{cr}} - 1}$. In the very strong relativistic case ($|a| \geq 1$), the relativistic self-focusing cannot be considered separately from other dynamic processes.

Another important mechanism in the relativistic regime of self-focusing is the creation of magnetic fields. The self-focusing channel interacts with the magnetic

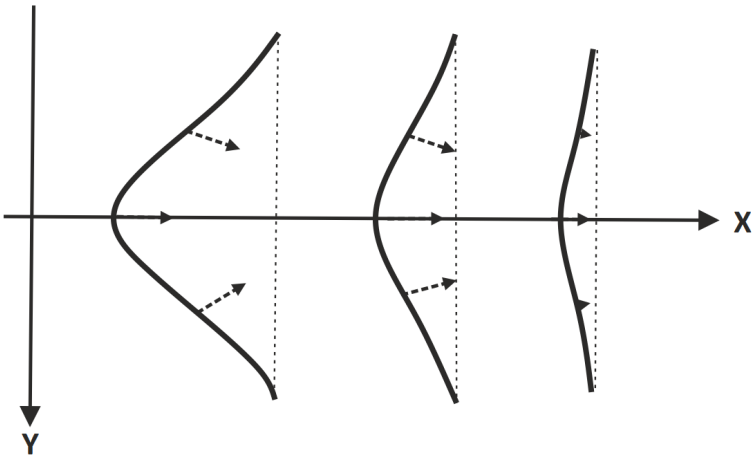

Figure 2.13: This figure shows a schematic representation of the phase front in a plasma. At relativistic intensities, the group velocity of the focused laser beam passing through a plasma is slower on axis. Due to the transverse intensity gradient, different refractive indices occur. The intensity gradient leads to different group velocities.

field. This interaction is due to the acceleration of the electrons in the self-focusing laser pulse, which is creating an electrical flux in the plasma, that is accompanied by a quasistatic magnetic field. The fast electrons are redistributed, which leads to a change in the reflective index. The plasma frequency is smallest in the regions with many fast electrons. Filaments with high intense laser radiation can merge and deliver a mechanism for the transport of laser energy over large distances [73].

3 Laser set-up and Diagnostics

A steady improvement of laser driven ion acceleration leads to a continuous increase in ion energies and fluxes which require novel, high resolution ion diagnostics. The detection of laser-accelerated ions is challenging due to high ion fluxes and short interaction times.

This chapter gives an overview about the laser system and its specific parameters. First, the generation of ultra-short laser pulses at high energies using the chirped pulse amplification technique is described. In the ultra-short, high-intensity regime, the chirped pulse amplification technique is essential. By stretching and compressing the laser pulse in the time-domain an amplification without damaging the optical components can be ensured. Secondly, the Arcturus laser system and its different components are presented. Contrast improvement with the cross-polarising wave technique (XPW) and plasma mirror set-up is going to be explained subsequently. Different diagnostics used in this thesis especially for ion detection will be presented afterwards. The main working principles of a Thomson parabola-MCP assembly and radiochromic films are going to be described. Given the particular properties of multi-MeV proton beams, they are suitable for different applications such as radiographic probing. Accelerated protons can be employed as a particle probe in order to detect electrical and magnetic fields. The high spatial and temporal resolution designate accelerated multi-MeV proton beams as supremely convenient for laser-plasma experiments.

3.1 Laser system

Chirped Pulse Amplification CPA

Amplifying very short laser pulses increases the laser power and fluence rapidly, causing distortions and/or damages in the gain medium and other optics due to undesirable non-linear effects (e.g. filamentation, self-focusing, etc.) generated by the high radiation intensity in the amplification chain. To prevent and circumvent this undesirable effect, the **c**hirped **p**ulse **a**mplification (CPA) technique is exploited [3]. The basic principle of the chirped pulse amplification technique is illustrated in figure 3.1. Short pulses are intentionally stretched several thousand times in the time-domain, lowering the fluence accordingly without changing the input pulse energy. Following this, the pulse is amplified by a factor of 10^6 - 10^{12} and is recompressed by the compressor several thousand times close to the initial

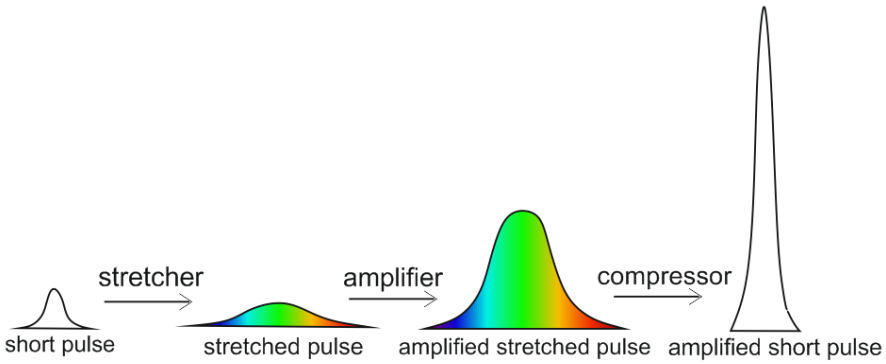

Figure 3.1: Basic principle of the chirped pulse amplification technique. Firstly the pulse is stretched to avoid non-linear effects during amplification. Subsequently the pulse is compressed to (nearly) reach its initial duration.

value. Stretching and compressing are realised by an arrangement of gratings as shown in figure 3.2. The stretcher is a pair of gratings dispersing the spectrum and shortening the optical path of longer wavelengths and elongating the optical path of shorter wavelengths, respectively. The pulse is expanded to few hundreds of picoseconds thus having a smaller intensity to be amplified without damaging any optics. The main reason for reducing the intensity is the reduction of non-linear effects which are proportional to the radiation electrical field. These non-linear effects have some undesired consequences such as spatial and spectral distortion of the laser phase and non-linear effects on the laser propagation which can result in damages.

After passing through the stretcher, the pulse is extracted from the amplifier and sent to the compressor. Here, its initial pulse duration is recovered and the dispersion which is introduced by the stretcher and amplifier needs to be compensated. Therefore, another arrangement of gratings contrary to the stretcher is needed, where rays with longer wavelengths travel a longer distance than shorter wavelengths. Hence, the dispersion can be compensated. These stretcher-compressor arrangements allow to separate the pulse generation and amplification stages. Due to thermal lensing caused by the energy from the pump beam, which leads to a radial thermal gradient in the laser rod, the refractive index increases. The laser rod acts like a positive lens and focuses the beam. Due to thermal aberrations, the beam size increases and the available intensity decreases.

Femtosecond pulses are mode-locked. This means ultra-short pulses are a superposition of many electromagnetic waves (modes). The ultra-short pulse generation is

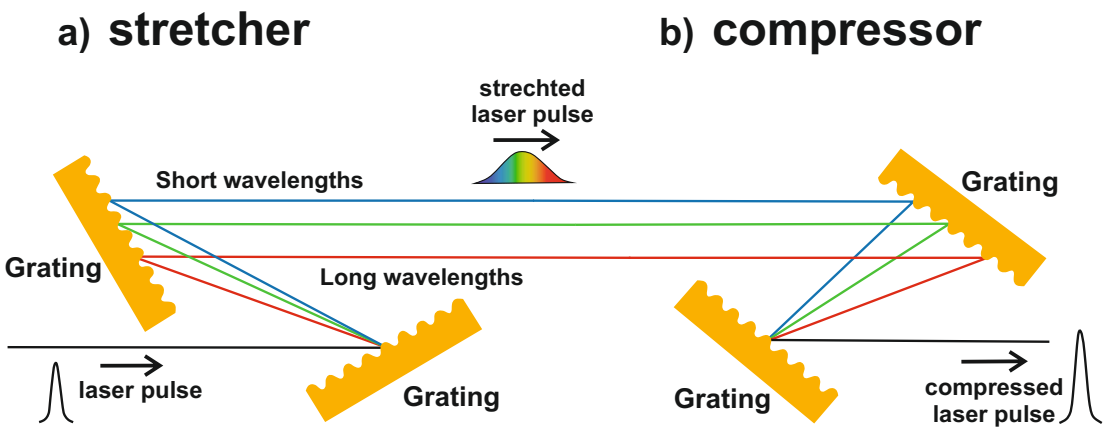

Figure 3.2: Grating arrangements for a) stretcher and b) compressor. To amplify the pulse without damaging, the beam is stretched and amplified afterwards. In order to have a short pulse again, the beam is compressed to its initial duration. In a) the arrangement of gratings for the stretcher is shown. Longer wavelength rays travel shorter distance than shorter wavelength. The short pulse is being stretched, and thus it can be amplified without damaging the optics and the laser pulse. The arrangement of gratings for a compressor (b) is contrary to the stretcher arrangement. Longer wavelength rays travel a longer distance than shorter wavelength rays.

transform- (or bandwidth-)limited by [36]

$$\tau_p = \frac{1}{\delta\nu}. \tag{3.1.1}$$

As can be seen, the limitation is highly depending on the bandwidth $\delta\nu$. To reach short pulses, a large bandwidth is essential.

3.1.1 Düsseldorf Arcturus laser system

The Arcturus laser system at the Heinrich-Heine-University in Düsseldorf in the institute of laser and plasma physics is a double beam, 200 TW commercial laser system designed by *Amplitude Technologies* based on the CPA technique described above. The system provides three separately compressible beams: two high power main beams (200 TW) and one low power beam (30 TW), which gives the advantage of flexibility of experimental parameters. The two main beams have pulse energies up to 5 J at 10 Hz repetition rate and pulse durations between 23-30 fs at a wavelength of 800 nm. Focusing the laser pulse, intensities up to 10^{20} W/cm^2 can be reached and relativistic effects become highly relevant. After an upgrade in 2017, energies up to 7 J at a repetition rate of 5 Hz and a wavelength of 800 nm can

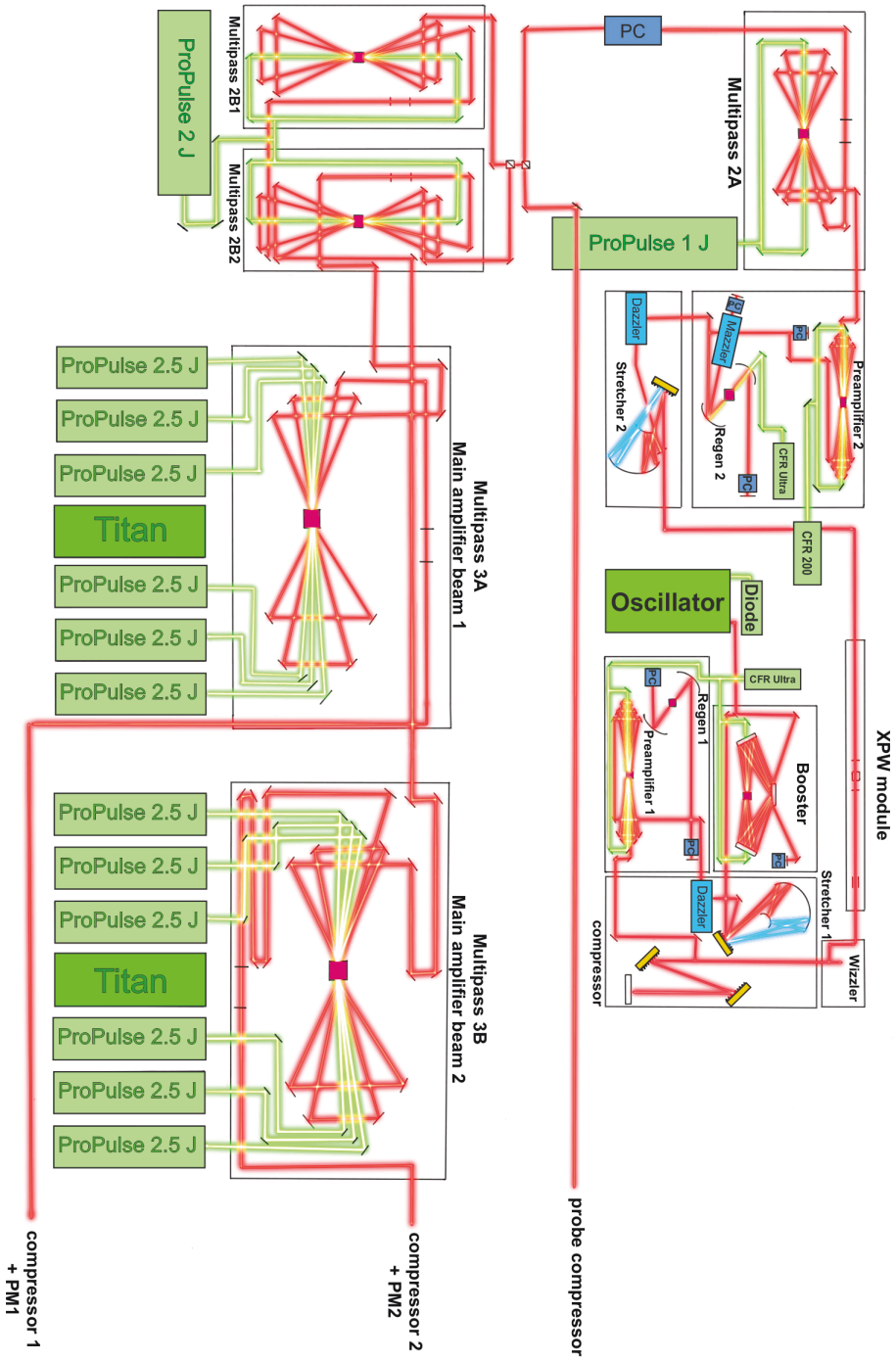

Figure 3.3: Illustration of the double CPA architecture of the Arcturus Laser facility Düsseldorf. The pulse is generated in the oscillator, preamplified and subsequently contrast enhanced in the XPW module. Before being split into two parts (or three, respectively, two main beams and one probe beam) the pulse in amplified in a second preamplifier and the multipass 2A module. The two main beams are further amplified in a main amplifier before being compressed and sent to the target area.

be achieved. The upgrade includes the installation of two more powerful additional pump lasers. However, the experiments presented in this thesis have been carried out before the upgrade.
The general architecture of the Arcturus laser system is shown in 3.3. It is divided into three different parts: the front end, the amplification modules and the vacuum compressor. The femtosecond front end and the main amplifier systems are installed on two optical tables and the different modules such as booster, stretcher etc. are set on bread-boards. The Arcturus laser facility is a double-CPA system with an XPW unit in between.

Oscillator

All three beams originate from a mode-locked Synergy titanium-doped Sapphire (Ti:Sa) oscillator by *Femtolasers*. The Ti:Sa laser is pumped through a 5 W CW-diode laser (frequency doubled to 532 nm). With a central wavelength of 790 nm (and a bandwidth of ± 50 nm) the oscillator delivers pules of about 5 nJ each at a repetition rate of 76 MHz, when mode-locked.
The mode-locked technique is realised by exploiting the non-linearity of the refractive index. The optical process of the Kerr effect allows the generation of short pulses of a few femtoseconds (Kerr-lens-modelocking). The index distribution can be written as [77]:

$$n(r) = n_0 + \frac{1}{2} n_2 I(r). \tag{3.1.2}$$

For a positive refractive index of the gain medium n_2, the refractive index increases with the light intensity I. The laser beam is self-focusing while crossing a medium with a positive refractive index. In figure 3.4, the relation between the refractive

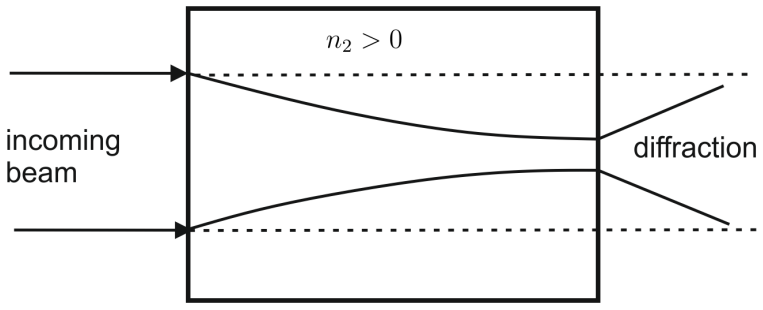

Figure 3.4: Self-focusing of a laser beam while passing through a medium with positive refractive index ($n_2 > 0$). The phase delay induced by the Kerr effect is highest on the beam axis and smaller outside the axis, which leads to the focusing of the propagating laser pulse.

index and the intensity is shown.

Booster

The beam is amplified by a compact 14-pass-amplifier up to microjoule level. It is pumped by one arm of a 33 mJ Nd:YAG laser (*CFR ultra*) manufactured by *Quantel*. The oscillator output is amplified and the temporal contrast is also enhanced by a saturable absorber at the same time. A pulse picker (Pockels cell) reduces the repetition rate to 10 Hz. A Pockels cell is an electro-optical modulator, which is used as a voltage-controlled wave plate. It can rotate the polarisation of the beam which passes through. Residual amplified spontaneous emission (ASE) background is reduced by a saturable absorber.

First CPA module

Stretcher

The pulse is stretched up to roughly 500 ps by inducing a chirp, and thus the peak intensity is reduced to avoid damages on the ensuing amplification stages. The design of the stretcher is based on an all-reflective Öffner. It is a combination composed of two spherical concentric mirrors where the first one is a concave and the second one a convex mirror. It shows a complete symmetry, and thus only spherical aberration and astigmatism can appear. Since all optical elements are mirrors, no on-axis coma and thus no chromatic aberrations can appear.

Dazzler and Mazzler

Additionally, an acousto-optical filter, the *Dazzler* by *Fastlite*, is implemented right after the Stretcher. It is used as a phase-modulator to pre-compensate the dispersion and the phase distortions, which can occur throughout the laser system. In order achieve an optimised laser output, the *Dazzler* is modulating the phase and also the amplitude of the laser pulse. To de-correlate the phase compensation and amplitude modulation, another acousto-optical device, the *Mazzler*, is used. The **Mazzler** is slightly different to the *Dazzler*. The beam is diffracted by an acoustic wave and the unwanted spectral components of the diffracted beam are sent away from the laser cavity. In the non-diffracted beam (cavity beam), a hole is created where the gain is highest, which results in gain flattening. The *Mazzler* is improving the spectrum enlargement by flattening the global amplifier gain and modulating the amplitude. The system consists of two *Dazzlers* and one *Mazzler* behind the first and the second stretcher unit and one dazzler, in the second region.

Regenerative Amplifier

The first amplification stage is a regenerative amplifier (Regen), where the stretched

pulse is amplified to an energy of 1 mJ. It consists of a cavity with a Ti:Sa crystal pumped by the *CRF Ultra Nd:YAG* laser. Two Pockels cells are used to, on the one hand, control the seeding of the stretched pulse into the regenerative cavity and on the other hand to control the outcoupling from the cavity. After passing through the regenerative amplifier, the beam is amplified by an additional five-pass butterfly amplifier. The butterfly amplifier is also pumped by a *CFR 200*.

Compressor 1
The beam is compressed by a double-pass grating compressor after the preamplifier stage.

Wizzler and XPW
Before entering the XPW module, the laser pulse can be characterised by a *Wizzler*, measuring the pulse duration and the spectral phase.
The temporal contrast of the pulses is enhanced by using a non-linear temporal filter, where the non-linear effect of generation of cross-polarised waves (XPW) is exploited. XPW generation can take place in an isotropic crystal. Typically, Barium Fluoride (BaF_2) crystals are used [78]. An intense linearly polarised wave with sufficient intensity incident on the crystal can generate a new wave with the same wavelength but a polarisation orthogonal to the incident wave. The crystal is placed between two polarisers, where the first one ensures a perfectly linearly polarised input beam and the second one distinguishes the cross-polarised wave from the fundamental wave. The less intense parts of the pulses, e.g. pre-pulses, remain unconverted and are extracted by the second polariser from the beam path, which leads to an enhancement of the pulse contrast. A hollow core fibre in front of the XPW helps to spatially filter the beam. After the XPW, the outcoupled energy is about 100 µJ.

Second CPA and main amplifier
A second Stretcher-Dazzler module follows the XPW. The operation mode is the same as in the first stretcher. The beam is amplified by a second regenerative amplifier and preamplifier with an additional *Mazzler* module (cf. above) after the stretcher.
Three Pockels cells, two for the cavity of the regenerative amplifier and one in front of the preamplifier clean the temporal profile of the pulse. The beam is expanded by a telescope before entering the next amplification stage.

Multi-pass Amplifier
Three multi-pass amplifiers are used to further amplify the beams to their final

energy. In the first amplification stage behind the front-end, the four-pass butterfly amplifiers are pumped by a frequency doubled *Propulse* Nd:YAG 1 J laser manufactured by *Amplitude Technologies*. After this amplification stage, the beam has an energy of roughly 300 mJ.
The beam is split into two arms by a beam splitter. One arm with 70 % of the energy is used for the two main beams and the other arm with 30 % of the energy for the probe beam. The probe is guided through a delay stage and to a designated compressor. Another 50:50 beam splitter is dividing the arm of the beam with 70 % of the energy equally into the beam path of beam 1 and beam 2 (main beams). Each main beam is again amplified by a four-pass butterfly amplifier pumped by a 2 J Nd:YAG *Propulse* laser designed by *Amplitude Technologies* up to an energy of approximately 300 mJ.

Main Amplifier
In the last amplification stage, each main beam is pumped by six Nd:YAG *Propulse* lasers. The beams are going through a Titanium doped Sapphire crystal which is cooled in a vacuum vessel by a Helium cryostat. Due to the high average power of the pump beams, the gain medium needs to be cooled in order to avoid thermal lensing. The cooling also ensures keeping the fluence below the damaging threshold of the crystal's anti-reflective coating (< 100 mJ/cm^2). After the final amplification stage, the beam is expanded to a diameter of 8 cm.

Compressors
Each beam is guided to its own designated compressor and is compressed to a pulse duration of approximately 27 fs. In the compressor, the beam is passing two gold gratings two times (on a different level) in a geometry which provides the compensation of the beam dispersion. To prevent non-linear effects in air and to achieve high output power, the compressor is placed in vacuum. Nevertheless, the transmission efficiency of the compressor is 50-60 %.

3.1.2 Plasma Mirror

Besides the XPW module and the Pockels cell, further contrast enhancement can be achieved by a plasma mirror. The operating principle of a plasma mirror set-up is shown in figure 3.5. It is an additional element which can easily be implemented into the beamlines if necessary. The first attempts for plasma mirrors were made in the early 1990s by Kapteyn et al [79]. The laser pulse is focused to a focal spot size of roughly 50 µm (FWHM) onto a coated glass substrate. When a high intense

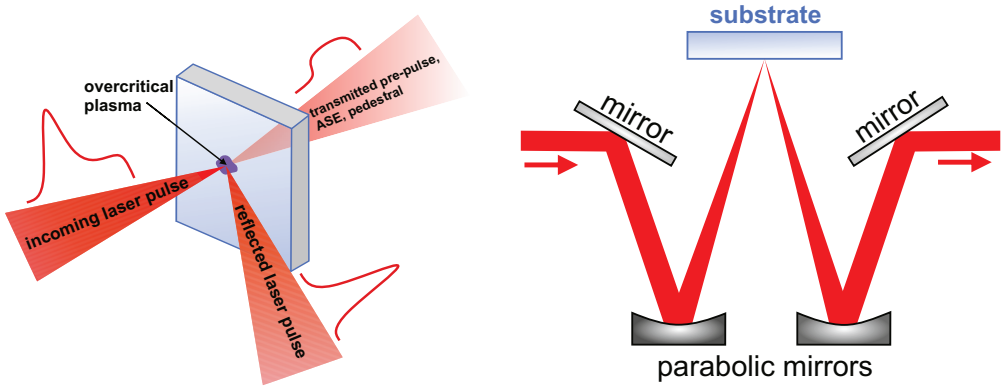

Figure 3.5: The basic working principle of a plasma mirror (left-hand-side) and the schematic drawing of the set-up (right-hand-side). The incoming laser pulse is focused on a substrate which is immediately ionised and acts like a reflective mirror. The second parabolic mirror re-collimates the reflected high contrast mirror.

laser pulse impinges on a polished surface, it generates a dense plasma which itself acts like a high-flatness mirror. These so-called plasma mirrors do not only reflect the remainder of the incident beam, but also act like active optical elements. The pre-pulsed and the ASE pedestal are still transmitted but the rising edge of the main pulse is igniting an overdense plasma reflecting the main pulse. When the electron density exceeds the critical density, the plasma becomes dense enough to screen the incident laser field and the target reflectivity strongly increases [80]. This plasma would be expected as unstable and hardly controllable, but unlike the expectations, it expands just by a small fraction of the laser wavelength. The contrast of a high power laser pulse can be improved by reflecting the laser pulse on a dielectric target which has a low reflectivity initially. The magnitude of the contrast enhancement depends on the ratio between the plasma and the initial target reflectivities [80]:

$$\triangle C = \frac{R_{plasma}}{R_{target}}. \tag{3.1.3}$$

The better the anti-reflective coating of the substrate, the better the contrast enhancement. This is why anti-reflection-coated substrates are used to improve the temporal contrast ratio.

The Arcturus laser facility has two separate, identical plasma mirror set up which can be implemented as the experiment requires. Since they are not part of the core design of the system it is convenient to adapt the module to the system. The design of the plasma mirror systems is adapted to the facilities specifications, such as space limitations, pulse duration and intensity. In the Arcturus system, the

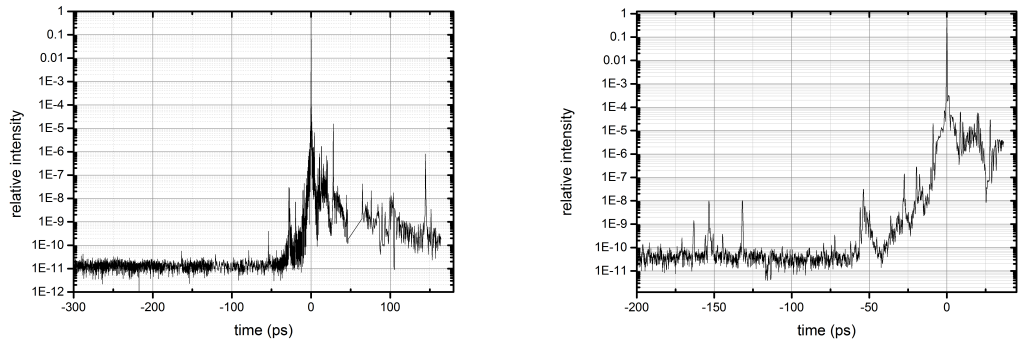

(a) B1 contrast (b) B2 contrast

Figure 3.6: Measurements for B1 (a) and B2 (b) contrast. Both graphs were obtained by a *Sequoia* measurement before the upgrade of the laser system. The contrast measurements were carried out without the plasma mirror implemented.

laser pulse is injected into the plasma mirror configuration by a turning mirror right after the compressor. It is focused onto an anti-reflective multi-layer-coated substrate by an F/22 off-axis parabolic mirror. At this stage, the laser pulse has an intensity of 10^{16} W/cm^2 and the plasma has a reflectivity of approximately 80 %. The dependence of the plasma mirror reflectivity over an intensity range of 10^{16} W/cm^2 - 10^{17} W/cm^2 is recorded in [81].
The contrast of B1 and B2 under the same conditions as in the experiments is shown in figure 3.6. The measurement is done by a *Sequoia* from *Amplitude Technologies*, a state-of-the-art technology device to measure the temporal contrast of the laser pulse. A contrast measurement with the plasma mirror system implemented can be found in [81].

3.1.3 Target Area

After the beam passes through the compressor (or the plasma mirror, respectively), it is sent through a tube system into the target chamber. The target chamber is placed in the so-called "Bunker". It is a radiation shielded bunker, which is a very important part of the Arcturus laser facility. Due to high intensities, which can be reached during the experiments, ionised radiation is generated. The radiation safety bunker is shielding the radiation and the accelerated particles.

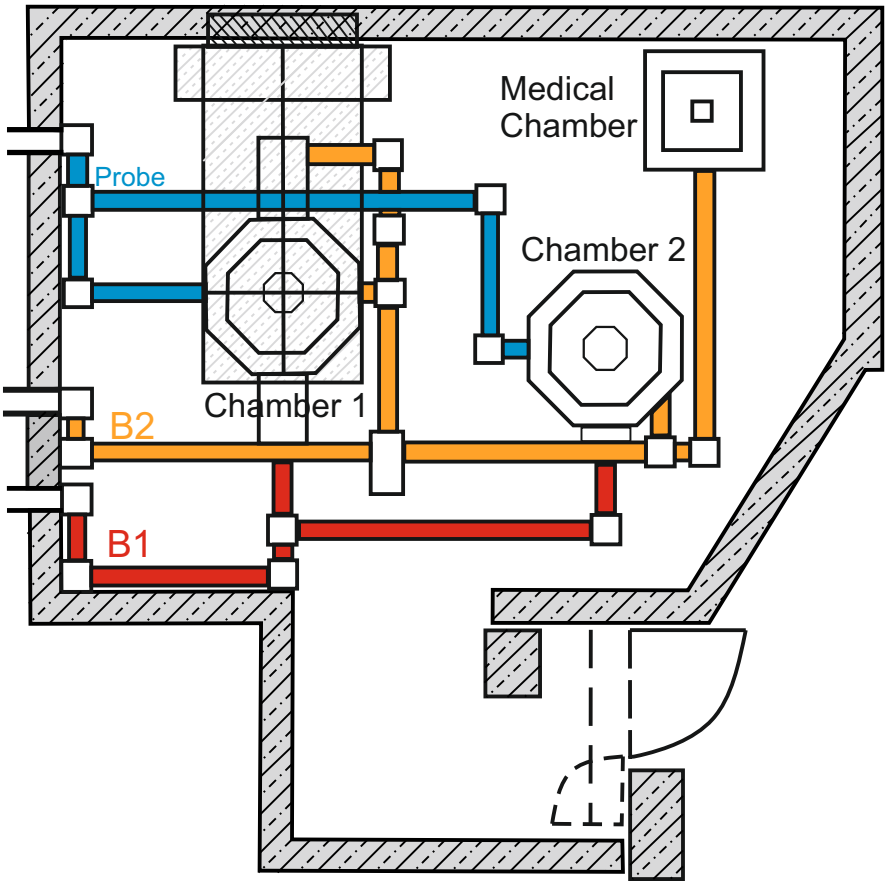

Figure 3.7: Schematic drawing of the lay out of the target area. The three vacuum chambers (chamber 1, chamber 2 and medical chamber) and the beamlines for the three different beams (two high intensity beams (B1, B2) and the probe beam) are shown. For radiation safety reasons, the walls of the target area consist of concrete with small implemented iron spheres.

Its walls consist of concrete with small implemented iron spheres which are absorbing the ionised and accelerated particles. Figure 3.7 shows the construction of the target area in the Arcturus laser facility. The experiments in this thesis were carried out in chamber 2.

3.2 Thomson Parabola - MCP assembly

For a quantitative analysis of ion beams originating from the laser plasma interaction, a Thomson parabola spectrometer can be used. The first attempts on spectrometers go back to J. J. Thomson in 1911 [82]. Nowadays, it is one of the easiest and most commonly used diagnostic methods for laser accelerated ions [83] due to the great

advantage of its simplicity in design and construction.
The equation of motion for ions passing the Thomson parabola can be described by the Lorentz force

$$\frac{d\vec{p}}{dt} = q\left(\vec{E} + \frac{\vec{p}}{m\gamma} \times \vec{B}\right) \tag{3.2.1}$$

where $\vec{p}$, q, $\vec{E}$, m, γ and $\vec{B}$ are the relativistic momentum, the charge, the electric field, the ion mass, the Lorentz factor and the magnetic field, respectively. Passing through the fields the ion's experience a drift motion. The deflection of the ions is captured on a detector. The ion traces on the detector plane perpendicular to the ion's propagation direction can be determined as a function of their initial kinetic energy and their charge to mass ration [84].
Using Newton's second law and the kinematic equations, the particle deflection in x (horizontally) and y (vertically) [85] [86] can be calculated as follows:

$$x = \frac{qEl_E}{mv_x^2}\left(D_E + \frac{l_E}{2}\right) \tag{3.2.2}$$

$$y = \frac{qEl_B}{mv_y^2}\left(D_B + \frac{l_B}{2}\right) \tag{3.2.3}$$

where l_E and l_B describe the electric and magnetic field length and D_E and D_B the drift length, respectively. This finally leads to the parabola equation

$$y^2 = \frac{qB^2 l_B(D_B + 0.5l_B)^2}{mEl_E(D_E + 0.5l_E)}x \tag{3.2.4}$$

which is true for the non-relativistic case.
Equation 3.2 shows that a Thomson parabola provides a separation of all ion species and charge states depending on $\frac{q}{m}$. Every single parabolic trace belongs to a different ion charge-to mass ratio. The deflection along the parabolic trace contains information about the ion energy [87].
A Thomson parabola spectrometer is a simple arrangement of a few components: a pinhole (here: 250 µm) at the entrance of the spectrometer to select a small fraction of the ion beam for a higher detection resolution, a magnetic field, thus accelerating the ions depending on their energy, an electric field, where the ions are separated depending on their charge to mass ratio, and a detector (Microchannel-Plate (MCP) detector coupled to a phosphor screen) to visualise the ion tracks.
The Thomson parabola spectrometer is placed in a vacuum chamber which is separated from the target chamber by a shutter, and thus the target chamber

can be vented without venting the Thomson parabola. A high vacuum (at least 10^{-5} mbar) is important to avoid a vacuum breakdown (sparking) between the two electrodes which create the electric field.

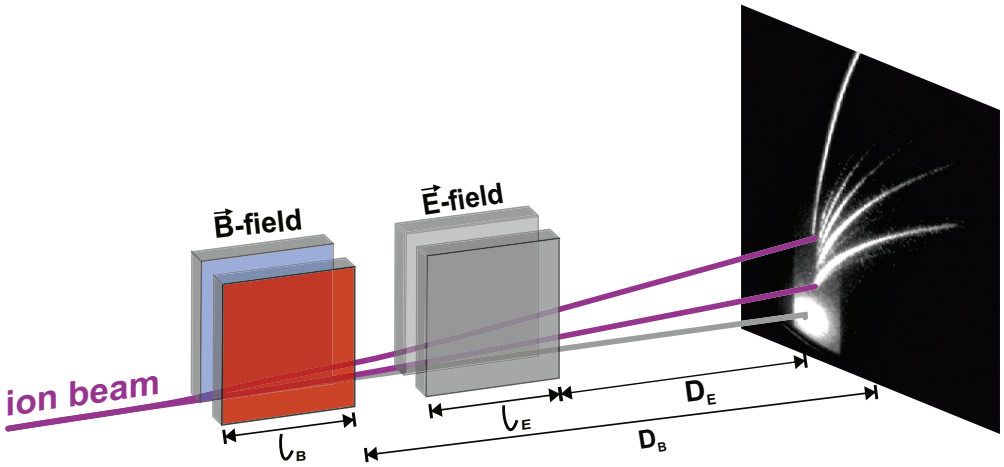

Figure 3.8: Schematic representation of the Thomson parabola arrangement. The ions are deflected while passing a magnetic and an electric field. An exemplary raw image on the detector (MCP) is shown on the right.

The set up of the Thomson parabola is shown in 3.8. As described in the figure, the Thomson parabola is based on a parallel magnetic and electric field. The fields are parallel to each other and perpendicular to the ion propagation direction. A yoked pair of permanent magnets with a length of 50 mm and a magnetic field strength of 0.5 T is generating the magnetic field. To create the electric field, two opposing electrodes (50 mm in length) with a potential of a few kV in between are used. The gap between the electrodes is 10 mm. The electric and magnetic fields can be assumed to be parallel with a gap of 7 mm between them. At the edges of the electrodes/magnets, the fields are getting inhomogeneous, but since the fields are quickly decreasing outside the electrodes/yoke, the inhomogeneity can be neglected.
The main parameters affecting the intrinsic resolution of a Thomson parabola are the drift length and the pinhole size. A stronger and longer magnetic field increases the energy resolution by higher dispersion. Increasing the pinhole size decreases the resolution since the ion beam spot size on the detector is increased [84]. Here, the pinhole has a diameter of 250 µm.
For the ion detection, a double stage MCP detector in Chevron configuration from *Hamamatsu* company is used, which consists of two MCPs rotated 90° from each other producing a v-like (Chevron) shape as shown in figure 3.9. The ion feedback in the device is reduced due to the angle between the channels. The advantage

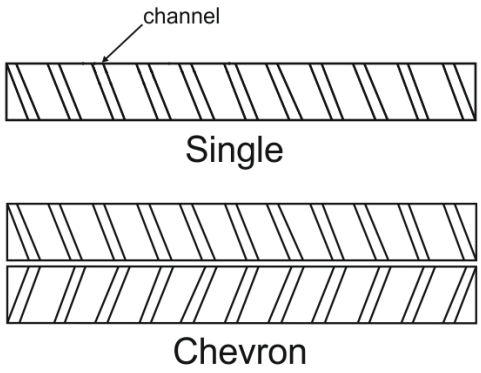

Figure 3.9: Single (top) and chevron (bottom) assembly of a microchannel plate.

compared to a single stage stage MCP is significantly higher gain at a given voltage. An electron which exits the first plate induces a cascade in the second one. The gain factor of the MCP used here is 10^6.
The schematic structure and working principle of a microchannel plate is shown in figure 3.10. A great number of glass capillaries (channels) are assembled as an

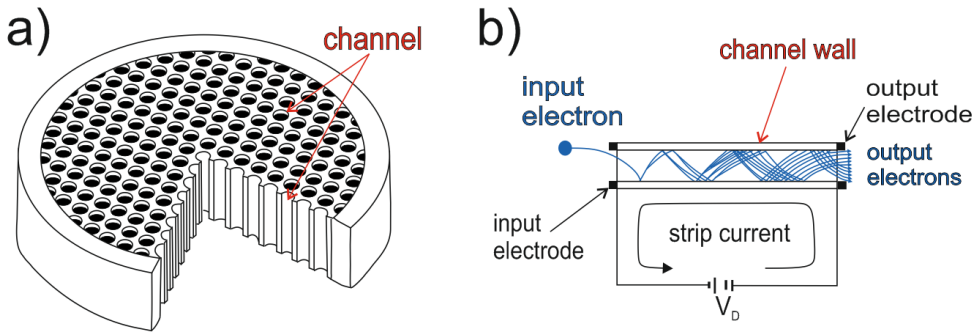

Figure 3.10: a) Schematic structure of a microchannel plate. b) Working principle of a microchannel plate.

array and form a thin disk with an effective diameter of 77 mm. Each channel has a diameter of 21 ± 0.5 µm and a channel length of 840 µm, which leads to a channel length to diameter ratio of 40:1. Their inner walls have proper electrical resistance and secondary emissive properties. The walls consist of a semiconductor material.
The charge saturation is depending on the channel diameter. A larger channel diameter leads to a higher level of charge saturation. Another option to overcome the saturation limit is the use of a two-stage MCP detector [87]. Each channel acts like a photo-multiplier itself. If an electron impinges on the inner wall of the

channel, secondary electrons will be emitted from the semi-conducting material. These electrons are accelerated by the electric field which is created by the applied voltage to the output end of the MCP. The channels are on the input and output surfaces electrically connected in parallel by thin metal electrodes. The applied MCP voltage is 1.3 kV. The accelerated electrons strike the opposite wall while travelling along the channel and produce more secondary electrons. This process is repeated many times along the channel thus increasing the number of electrons exponentially. The principle of multiplication is shown in 3.10. Since this process happens in each channel, the information about the position on the output electrode stays the same.
To prevent the electrons passing through the channel without impinging on the walls and to suppress ion back drifts from the rear side, the channels are slightly at an angle. The MCP used in the experiments for this thesis has a bias angle of 6°. At the output electrode, the MCP the electrons are converted to visible light on the phosphor screen. A voltage of 3.3 kV is applied on the screen. The screen is imaged with a *Stingray* camera. MCP detectors allow an online measurement and real time detection of the accelerated ions, which is a great advantage to other detectors such as image plates or radiochromic films.

3.3 Stopping of energetic ions in matter

Soon after the emission of energetic particles from radioactive materials was discovered, the attention and interest was drawn to the stopping of ions propagating through matter. Already in 1898, Marie Curie argued that alpha rays can loose their speed while traversing matter. Early attempts to explain the particle energy loss failed because there was not an accurate and definite model of the atom yet. After Niels Bohr presented his model of the atom in 1911 (Bohr model), a more conclusive theory could be established [88]. One of Bohr's original conclusions was that the energy loss of ions passing though matter could be divided into two components: nuclear stopping (energy loss to the medium's atomic positive cores) and electronic stopping (energy loss to the medium's light electrons) [89]. Note that the electronic contribution dominates the atomic contribution.
20 years later, Hans Bethe and Felix Bloch gave a quantum-mechanical description of the mean rate of energy loss (stopping power) for a heavy, charged particle

$(m_0 \gg m_e)$[90] [91]:

$$-\frac{dE}{dx} = 4\pi N_A r_e^2 m_e c^2 Z_i^2 \frac{Z_A}{A}\frac{1}{\beta^2}\left[\frac{1}{2}ln\frac{2m_e c^2\beta^2\gamma^2 E_{max}}{I^2}\right] - \beta^2 - \frac{\delta}{2} \tag{3.3.1}$$

where N_A is Avogrado's number, r_e the electron radius, A the mass of the absorber, Z_i the atomic number of the incident particle, Z_A the atomic number of the absorber, I the average ionisation energy, δ a density correction factor and β and γ are relativistic parameters. $E_{max} = 2m_e c^2\beta^2\gamma^2/(1 + 2\gamma m_e/m_0 + (m_e/m_0)^2)$ is the maximum kinetic energy transferable to a free electron by a projectile of mass m_0. As can be seen, the stopping power is depending on the velocity and charge of the particle and target material. Simplifying equation 3.3 to the first order ($-\frac{dE}{dx} = \frac{1}{v^2}$), it is noticed that the energy is inversely proportional to the velocity squared. Faster ions loose less energy than slower particles. The stopping power is resulting in loss of particle energy due to interaction with matter. Primarily, protons scatter due to elastic Coulomb interactions with the target nuclei and thus loose their energy. The energy loss is described by the *Bragg curve*. The characteristic feature of the *Bragg curve* is the *Bragg peak*. Usually, the stopping power increases towards the end of range and reaches a maximum. This maximum is the *Bragg peak*. Almost immediately after reaching this Bragg peak, the energy drops to nearly zero. In other words, ions are depositing their energy at almost exactly a specific penetration depth. This feature is exploited for example in radiation therapy [92].
The Bethe-Bloch formula is valid for energies between 0.1 and 100 MeV. For electrons and positrons, this formula cannot be used. Since the mass of these particles is too low, they would just be deflected, and Bremsstrahlung becomes the dominant mechanism. Using this formula for electrons, the particles would be indistinguishable.

3.3.1 SRIM

However, the Bethe-Bloch equation is not solved directly. To calculate the stopping of ions in different materials, a programme named *SRIM* (The **S**topping and **R**ange of **I**ons and **M**atter) developed by James F. Ziegler is used [93]. *SRIM* allows to calculate many characteristics of ion transport in matter. It includes software packages for different calculations which provide for example tables of stopping powers, straggling and range distribution for any ion at different energy ranges. A great advantage of *SRIM* is the possibility to do more elaborate calculations like multi-layer configurations. Different foil and stack thicknesses can be modelled and

the propagation of an ion beam through various targets can be simulated.

Exemplary the stopping range for 7.4 MeV protons in the plastic layer of an RCF

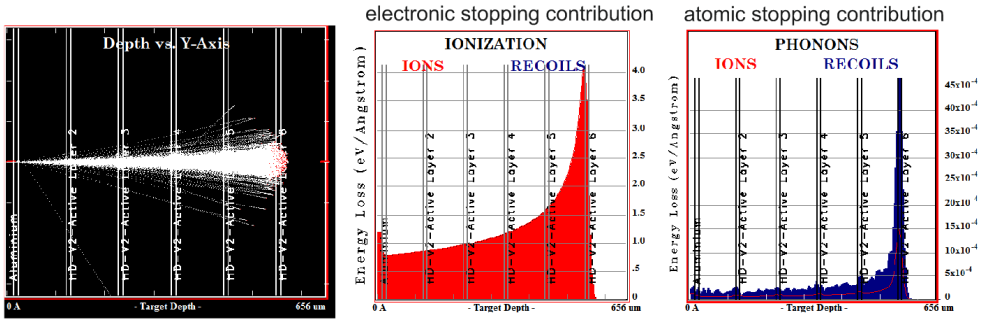

Figure 3.11: Exemplary image of a typical output of a SRIM calculation. The stopping range of 7.4 MeV protons (lhs) and the electronic (middle) and atomic (rhs) contribution to the stopping power are presented. Protons with an energy of 7.4 MeV correspond to the sixth RCF layer in a typical stack used in the experiments. For each RCF layer in a stack, SRIM calculations are performed, in order to determine the proton energy in each layer. Note that it was taken into account that the stack of RCFs is wrapped in 14 µm aluminium foil.

(mylar) is shown in figure 3.11. The same simulations are done for each RCF layer and corresponding proton energy.

3.4 RadioChromic Films

Another detector for accelerated protons, Gafchromic ® Dosimetry Films type HD-V2 manufactured by *Ashland* are used [94]. More generally, such dosimetry media are referred to as (types of) radiochromic films (RCF). RCFs are transparent plastic-based films designed for quantitative measurement of high-energy photons and are usually used in medical imaging and dosimetry applications [94]. The optical density of the films is proportional to the incident radiation dose, which means the higher the radiation, the darker green/blue the film gets. The optical density (o.d.) is related to the transmittance of a material. It is a measure for the amount of energy that can pass through matter. The optical density is given by [95]:

$$o.d. = -log_{10}\frac{\%T}{100}, \tag{3.4.1}$$

where %T is the percentage of transmission of a material upon exposure to radiation (e.g. ions, x-rays, γ-rays and electrons). The transmittance is described by the

ratio between the incident power and resulting power ($T = P_0/P$) and gives the effectiveness on transmitting radiant energy. Usually, RCFs are used for proton detection even though they can also detect electrons and x-rays. However, since electrons and x-rays are too fast, they cannot be detected in the energy range which is used in the experiments in this thesis.
Figure 3.12 a) shows the RCF structure used in this thesis (type HD-V2), which are comprised of a 10 µm active layer. The thickness can vary from batch to batch approximately between ± 1 µm and ± 0.3 µm within a batch. The active layer is the main radiation sensitive layer of the RCF. It contains the active component, marker dye, stabilisers and other components giving the film its energy-independent response and is coated on a clear polyester substrate with a thickness of 97 µm for mechanical support [94]. In this layer, the thickness can vary ± 2.5 µm.

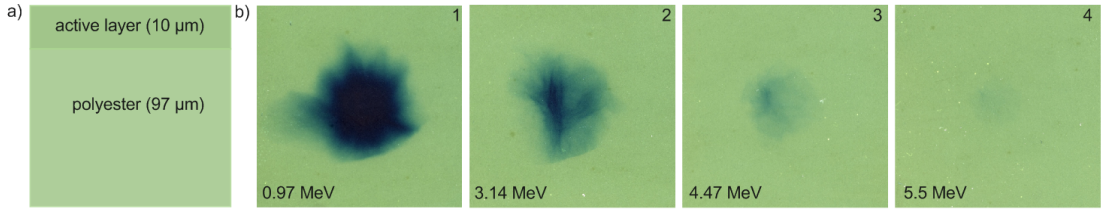

Figure 3.12: a) Structure of a radiochromic film type HD-V2. An RCF is composed of two layers, a 10 µm active layer and a 97 µm polyester layer. Both layers have similar densities (active layer: 1.25 g/cm^3, polyester layer: 1.35 g/cm^3) but different chemical compositions. b) Different colouring levels of radiochromic films in an RCF stack. Numbers on the top right corner indicate the position of the film in the stack. Accordingly, RCF number 1 is closer to the radiation source. Here, a free-standing 110 nm parylene foil (C_8H_8) was irradiated by a high contrast laser pulse with an intensity of 1×10^{20} W/cm^2 [96].

After irradiating the RCF, a polymerisation process in the active layer of the active organic dye takes place [97]. In figure 3.12 b), the different colouring levels of an RCF stack irradiated by protons which are accelerated from a 110 nm parylene foil are presented. The radiochromic film closest to the irradiation source (RCF number 1) has the darkest colouring level, and as can be shown in the SRIM calculations (see below), lower energy protons are stopped within a few µm penetration depth. Since the polymerisation reactions in the active layer do not spread between the microcrystals, a high spatial resolution in sub-µm range can be achieved [94]. The films should be read out at least 24-48 hours after the irradiation, since the colour changing process will not be completed even though the biggest change will be seen immediately after the irradiation within a few milliseconds [98].

In order to obtain information about the particle flux, the transverse profile of the particle energies and the spatial structures, a stack of RCF layers is used during the experiments. The RCF stack is covered in 14 µm aluminium foil to prevent the RCFs from being exposed to laser light and low energy ions (< 1 MeV). In the experiments usually RCF stacks of four to five layers were used.
As described above (cf. chapter 3.3), ions are stopped while propagating through matter and deposit most of their energy at the Bragg peak. Higher energy protons will travel further through the material while lower energy protons will be stopped faster. Using a stack of RCFs, each RCF layer will contain information about protons of different certain energy. The energy loss for each proton energy is depending on the target depth (i.e. different layers of the RCF stack) is calculated via *SRIM* (cf. chapter 3.3.1). Figure 3.13 shows the Bragg curves for different

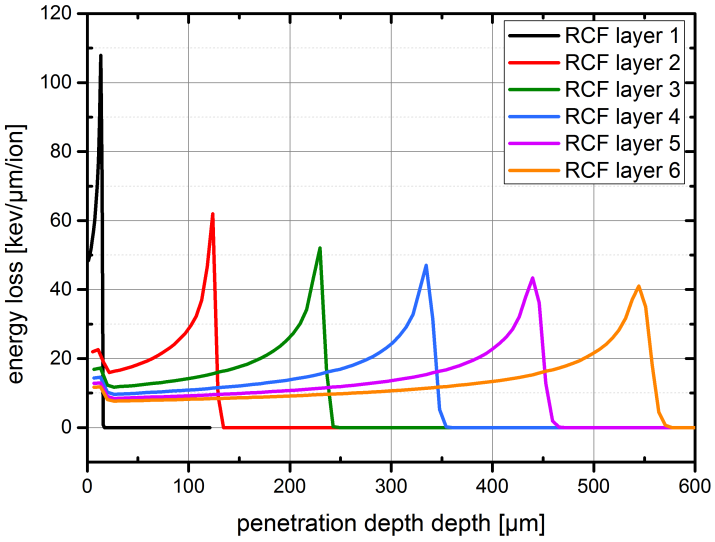

Figure 3.13: Energy deposition in each RCF layer as a function of penetration depth and proton energy. The Bragg curves are simulated with SRIM for the radiochromic films type HD-V2.

proton energies in each RCF layer.
As discussed above, the active layer of the RCFs, where the colouring dye is stored, has a thickness of 10 µm. All protons reaching the RCF within this 10 µm can activate the colouring dye. Considering for example the active layer of the second RCF layer in the stack, the proton energies will be in the range of 3.14 MeV - 3.29 MeV. However, this 150 keV difference can be neglected.
Furthermore, the width of the Bragg peak needs to be taken into account. Not

only protons with energies exactly at the maximum of the Bragg curve, but also protons close to the Bragg peak can start the polymerisation process in the active layer. This leads to an uncertainty of less than 5%, which will be considered in the analysis.

3.5 Principles of proton probing

The proton imaging technique is one of the main diagnostic tools in the experimental campaigns. This imaging technique is based on the deflection of charged particles in a probe beam. The motion of a proton passing through an electromagnetic field is described by the Lorentz equation (cf. chapter 2.1.1)

$$m_p \frac{d\vec{v_p}}{dt} = -e\left(\vec{E}(t) + \frac{1}{c}\vec{v_p}(t) \times \vec{B}(t)\right),$$

where m_p and v_p indicate the proton mass and velocity and $\vec{E}(t)$ and $\vec{B}(t)$ the time dependent electric and magnetic field, respectively.
In figure 3.14, a schematic drawing is showing the principles of imaging via proton deflection. A single proton crossing an electric and magnetic field distribution

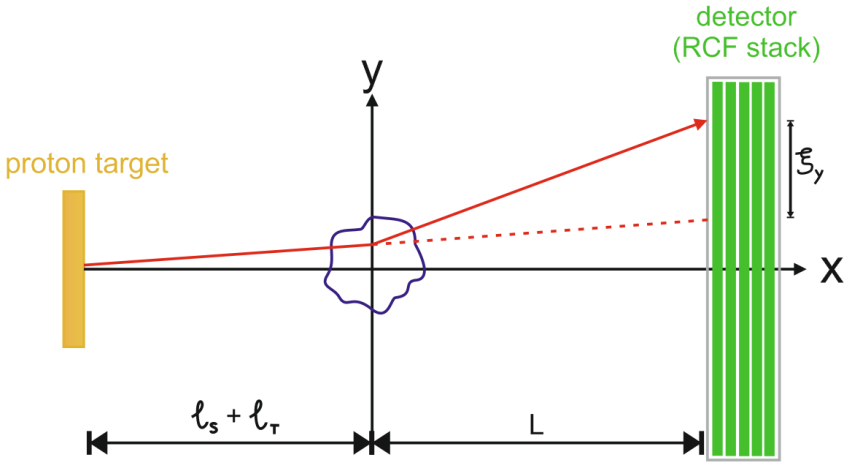

Figure 3.14: Schematic representation of the proton imaging technique. A single proton passing through the interaction area is deflected by the electric and magnetic fields.

acquires a transverse velocity. Assuming the electromagnetic field distribution is

restricted to a finite linear region, the transverse velocity is found to be:

$$\begin{aligned}\delta\vec{v}_y &= \frac{e}{m_p}\int\left(\vec{E}(t)+\frac{\vec{v}_p(t)\times\vec{B}(t)}{c}\right)_y dt \\ &\simeq \frac{e}{m_p v_p}\int_d \vec{E}(t)+\left(\frac{\vec{v}_p(t)\times\vec{B}}{c}\right)_y dx.\end{aligned} \tag{3.5.1}$$

Due to the laminar motion of the protons, the transverse motion is negligible compared to the longitudinal motion. Assuming that the deflection of the protons is small and neglecting the initial beam divergence, the longitudinal velocity can be written as:

$$v_x = \frac{dx}{dt} \simeq v_p. \tag{3.5.2}$$

Considering the time of flight of the protons $\triangle t \simeq \frac{L}{v_p}$ and an initial proton energy of $E_p = \frac{1}{2}m_p v_p^2$, the transverse displacement of the proton is given by:

$$\begin{aligned}\xi_\perp = \delta\vec{v}_p \triangle t &= \frac{eL}{2E_p}\int_d\left(\vec{E}(t)+\frac{\vec{v}_p(t)\times\vec{B}(t)}{c}\right)_y dx \\ &= \frac{eLd}{eE_p}\left\langle\left(\vec{E}(t)+\frac{\vec{v}_p(t)\times\vec{B}(t)}{c}\right)_y\right\rangle_d.\end{aligned} \tag{3.5.3}$$

For a known displacement, the averaged field along the trajectory can be written as:

$$\begin{aligned}&\left\langle\left(\vec{E}(t)+\frac{\vec{v}_p(t)\times\vec{B}(t)}{c}\right)_y\right\rangle_d \\ &= \frac{1}{d}\int_d\left(\vec{E}(t)+\frac{\vec{v}_p(t)\times\vec{B}(t)}{c}\right)_y dx \simeq \frac{2E_p}{eLd}\xi_\perp.\end{aligned} \tag{3.5.4}$$

A minimum detectable electric and/or magnetic field can be estimated from equation 3.5.3:

$$\left|\left(\vec{E}(t)+\frac{\vec{v}_p(t)\times\vec{B}(t)}{c}\right)_y\right| \simeq \frac{2E_p}{eLd}\xi_\perp. \tag{3.5.5}$$

The deflected proton beam can be detected for example via RadioChromic films (cf. chapter 3.4).

3.5.1 Experimental set-up of the Proton Probing Technique

Multi-MeV protons generated during the interaction of ultra-intense short pulses with thin solid targets can be used as a particle probe in laser-plasma experiments. Their particular properties such as small source size, low divergence, short duration and large number density make them most suitable for laser-plasma experiments [99] [100].

The first attempts of employing TNSA-driven proton beams for radiographic probing applications were realised soon after the discovery of the TNSA process [101]. The unique ability to empower single-shot spatiotemporal investigation of electric and magnetic fields induced during ultraintense laser-matter interactions makes the proton probing technique highly interesting and relevant.

The proton imaging technique provides a high temporal and spatial resolution in a point-projection scheme. Using multiple layers of dosimetric film, the broad energy spectrum of the proton beam can be exploited and a temporal multiframe capability can be achieved.

For the proton probing technique, the ability of the Arcturus laser facility providing two separately controllable ultra-short laser pulses is exploited. The typical experimental arrangement is shown in figure 3.15. An intense short pulse focused onto a

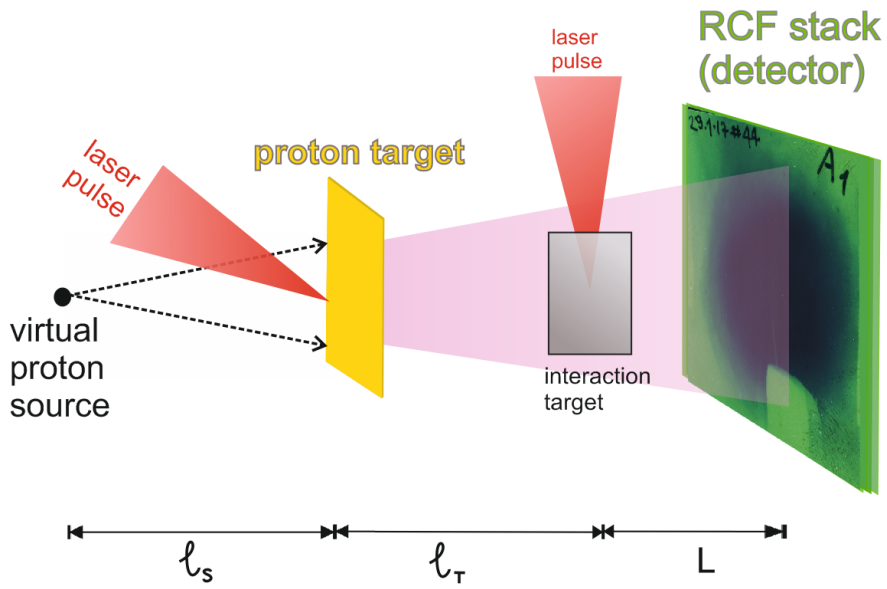

Figure 3.15: Schematic drawing of a proton probing set-up. A high-intense laser pulse accelerates a proton beam from a thin metal foil. A second target, the interaction target, is irradiated by a second high-intense laser pulse. The protons are passing through this electric and/or magnetic field and are deflected seen by the detector (RCFs).

metal foil (*proton target*) is accelerating a proton beam which is used as a charged particle probe in order to detect electric and/or magnetic fields inside/around a second target (*interaction target*). The second target is irradiated by a second intense short laser pulse.
The protons accelerated from the proton target are passing through the electric and magnetic fields of the interaction target which are generated during the interaction with a high-intensity laser pulse. A projection of the probed region is obtained, which indicates the electric and magnetic fields gradient distribution.
The physical source size at the rear side of the target was experimentally measured and is found to be approximately between 10 and 100 µm depending on the laser energy [102]. Such a small beam source size would lead to a poor spatial resolution. Nevertheless, as a consequence of high laminarity, the TNSA-driven proton beam can be assumed as a nearly point-like virtual source. The precise location of this virtual source has been experimentally shown to originate a few hundred microns from the front surface of the target (laser irradiated side) [103]. The geometrical magnification of the point projection of the probed region is given by:

$$M = \frac{\ell_S + L}{\ell_S + \ell_T} \simeq \frac{L + \ell_T}{\ell_T}, \tag{3.5.6}$$

where ℓ_S is the distance between the virtual and the physical source, ℓ_T the distance between the physical proton source and the interaction target and L the interaction point to the detector displacement. As long as the condition $\ell_S \ll \ell_T \ll L$ is fulfilled, the origin of the proton probe beam can be assumed to originate from a point-source and the magnification reduces to the expression given in equation 3.5.6.
It needs to be considered that the two beams are displaced by a few mm due to geometrical reasons. B2 is displaced by 2.3 mm in the x-direction and 4 mm in the z-direction.
In the experimental arrangement, usually ℓ_T is approximately 4.5 mm and L is between 35-45 mm. These values lead to a magnification factor between 8 and 9.
The broad energy spectrum of the proton beam allows a temporal resolution within one single laser shot. Using a capable detector, e.g. RCFs (cf. chapter 3.4), and exploiting that protons of different energies have different time-of-flights, the interaction target in only one single shot can be probed at different times. The spectral multi-frame capability yields a temporal multi-frame capability. High energy protons will reach the interaction point faster than low energy protons.

3.6 PTRACE

In order to confirm the experimental data, the particle tracing simulation code *PTRACE* developed by A. Shiavi was employed [32]. This code provides the possibility to analyse the effects of an electric field on the proton beam. The particle-tracing simulations are carried out by solving the relativistic equation of motion of a charged particle. The equation of motion of protons in the presence of an external electric (and/or magnetic) field is given by:

$$m\frac{dv_p}{dt} = e\left(E + \frac{v_p \times B}{c}\right). \tag{3.6.1}$$

The PTRACE code is solving the differential equation and computing the trajectories of the charged particles (protons). It is an effective tool for understanding the interaction of a proton beam with various filamentary structures generated during laser and plasma interaction. With this intention, a Runge-Kutta fourth-order algorithm combined with an adaptive step size monitoring is used [104]. The adaptive step-size routine guarantees smaller time steps at the examined dynamics where the acting forces are larger, which assures a regulation of the computational resources.
The C++ based programme is using different objects (functions and routines) which are acting on each other. For example, the mass and charge of the traced particle, the geometric parameters of the source and the time and space dependent force acting on a particle are specified and computed. A flow chart presenting a

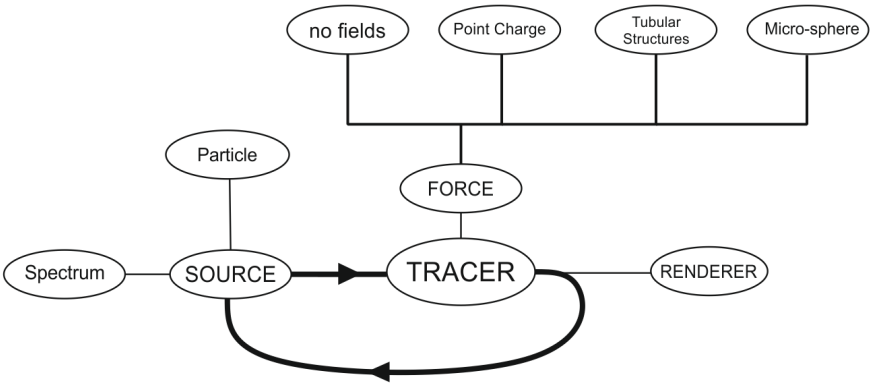

Figure 3.16: Flow chart of the particular components of the PTRACE simulation code developed by A. Shiavi *PTRACE*.

schematic diagram of the PTRACE simulation is given in figure 3.16. The code consists of a main loop and object components which can be varied. The different

objects combine functions and routines and allow to trace single particles.

4 Controlled plasma dynamics from dual beam experiments

Since the development of the chirped-pulse-amplification technique made ultra-short, high-intensity laser pulses available, the investigation of rapidly heated matter has become a particularly active research area. The acceleration of ions and the absorption of the laser energy are of special interest. The interaction between solid targets and ultra-short high-intensity laser pulses offers many possibilities for experimental and theoretical studies.

In this chapter, the experimental research concentrating on the properties of laser induced plasmas are going to be presented. Here, the studies focus on the interaction between ultra-thin foils and high-intensity, ultra-short laser pulses. Various measurements are performed, including the measurements of the absorption fraction of a high-intensity laser pulse by solid targets of different thicknesses (10s of nm), the channelling of a laser pulse through an overdense plasma and the acceleration of ions/protons.

A highly interesting behaviour of the transmission is observed. The investigations include the study of the dependence of the transmission on the delay between the two laser pulses and the laser intensity. The results indicate a notable dip in transmission at a specific delay between the pulses. Analytical calculations show that at delays investigated in the experiments, collisional absorption mechanisms become relevant. At the same delay position where the transmission reaches a minimum, a maximum in the collisional absorption is observed. Simultaneously, another exciting feature could be observed. At the same delay position, an enhancement of the proton energy is detected. With respect to single beam interaction, the proton energy is enhanced by almost a factor of two in the dual beam configuration.

Additionally, an imaging system transversal to the interaction point is employed in order to investigate the channelling of the high-intensity laser pulse through the plasma. The dependence between the channel length and the delay between the pulses and the laser intensity are recorded, respectively.

In the following, the experimental results of the interaction between a high-intensity laser pulse and an expanding plasma will be presented. The results of the various diagnostics will be discussed.

4.1 Experimental set-up

Figure 4.1 shows the experimental set-up of the dual beam experiments for the study of controlled plasma dynamics. Since ultra-thin foils are investigated, a special "ladder-like" target holder is needed, where the targets, which are attached on meshes, are mounted. On the right-hand-side of figure 4.1 the target holder along with targets on meshes is illustrated. The preparation and alignment of these targets is presented later in this chapter.

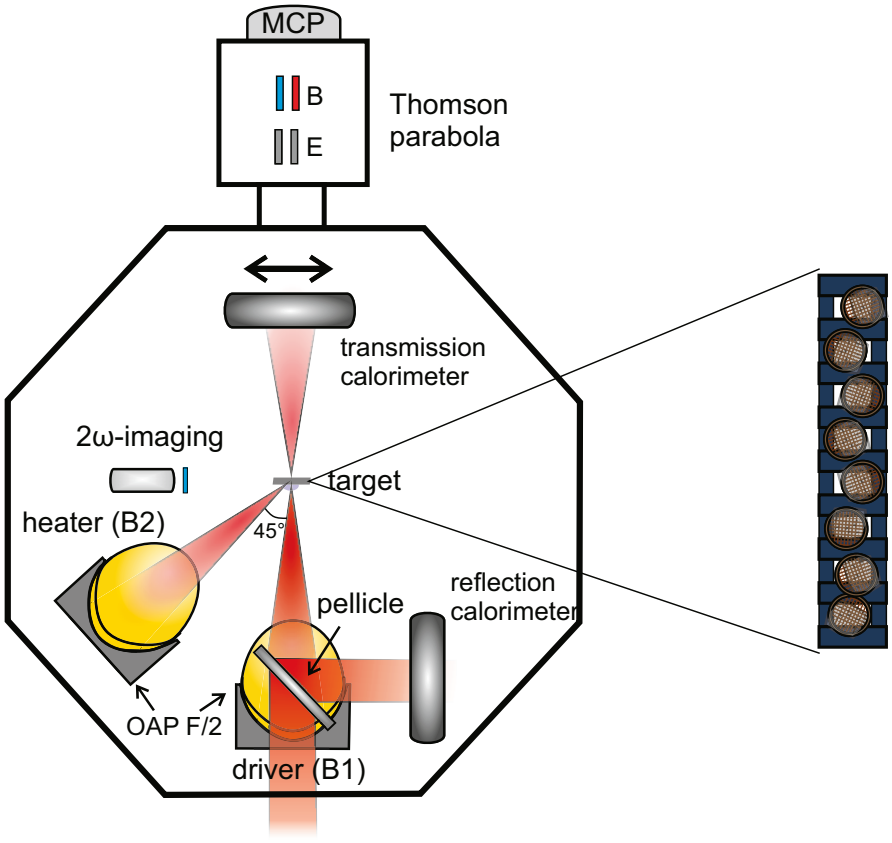

Figure 4.1: Experimental set-up of the dual beam arrangement for the the study of controlled plasma dynamics. The two off-axis-parabolas are arranged in a 45° configuration. Various diagnostics are employed as shown above: a simple 2ω-imaging system in order to observe the channelling of the laser light through the plasma, a Thomson Parabola - MCP assembly to investigate accelerated protons/ions and two calorimeters for detecting the absorbed energy fraction. Since the transmission calorimeter is blocking the Thomson Parabola, it is installed on a movable stage, which in turn means, that the transmitted energy and the ions accelerated in the laser direction cannot be observed at the same time. On the right-hand-side of the figure, a close-up of the target holder and the targets on meshes are shown.

The target and diagnostics are arranged in target chamber II. It is octogonally shaped and has a diameter of roughly 85 cm and a usable height of roughly 80 cm. At the exit of the compressor, the beam size of both beams is roughly 80 mm.
In order to enhance the contrast and have a small scale length of the preplasma, a plasma mirror is placed after the compressor, a few meters away from the target chamber in both beam lines. After the plasma mirror, the beams are guided through a tube system into the target chamber. Eventually, the beams are focused by an off-axis-parabola (OAP) to the smallest spot size possible ($\sim$ 5 µm) to attain maximum intensity. The advantage of an off-axis parabola over a plano-convex lens is that a parabola has no spherical and chromatic aberrations and provides a smaller focus size. Using an uncorrected plano-convex lens for focusing, the wave fronts get distorted and the pulse duration is elongated due to the difference between phase- and group-velocity [105]. The optimisation of the focal spot needs to be done after each pump down of the target chamber since the beam path is slightly different in air than in vacuum.
At high intensities, non-linear effects come into play. Materials which are transmitting visible light excellently fail at higher intensities. A measure for the non-linear phase shift of light is the B-integral given by $B = \frac{2\pi}{\lambda} \int nI(x)dx$. High intensities can occur when an ultrashort laser pulses is amplified which leads to a B-integral larger than 1. If the value is even higher self-focussing can occur. This non-linear lensing effect can become so strong that the beam collapses to a very small radius leading to an increase of the optical intensity and exceeding the damage threshold. Due to the group-velocity dispersion, a lens that focused visible light well may not focus an ultrashort pulse at all. Chromatic aberrations and non-trivial spatio-temporal distortions occur. Since an ultrashort pulse is broadband and the lens refractive index is disparate for different frequencies, the focusing spot for different frequencies may vary. The group velocity dispersion and chromatic aberration can be averted completely by using a mirror with a paraboloidal surface. An off-axis parabola keeps the focus out of the optical axis of the beam. The throughput of the compressor, the plasma mirror system and the beamline is approximately 25 % for both beams. The nominal amplification energy after the last amplifier is 4 J and thus the laser energy on the target is around 1 J. The best focal spot size for both beams is 5 µm and the pulse duration at Full Width Half Maximum (FWHM) is 30 fs. Hence the laser intensity on the target is I = 6.4 $\times$ 10^{19} W/cm^2. The intensity of the drive laser (B1) is varied between 9.5 $\times$ 10^{19} W/cm^2 and 1.4 $\times$ 10^{20} W/cm^2. The incidence angle of the drive laser on the target is 0° (normal incidence) and of

the heater (B2) 45°.
The beam is directed by a long working distance microscope objective (*Mitutoyo*) through a glass window out of the vacuum onto a CCD camera (*Basler*) outside of the chamber. In front of the camera are adjustable neutral density (ND) filters which allow to regulate the brightness of the incoming beam. Further optimisations concerning the brightness/gain can be done with the help of the camera's software. The vacuum pressure of the target chamber during normal operation is in the order of a few 10^{-4} mbar.
In order to quantitatively analyse ion beams emerging from the laser plasma interaction a Thomson Parabola - MCP assembly in the target normal direction is used (cf. 3.2). Two calorimeters are placed to measure the reflected and transmitted energies. Each calorimeter has a detector size of 10 cm. The calorimeter for the transmitted energy is positioned 15 cm behind the target on the axis of the driver beam. To determine the size and shape of the transmitted beam a **P**oly**t**etra**f**luor**e**thylen (PTFE)-plate is mounted in front of the calorimeter without obstructing the calorimeter's detection area. A pellicle is placed in the beamline of the driver beam as shown in figure 4.1 to measure the reflected energy. The pellicle is splitting the beam into two separate paths, thus allowing to measure the reflected laser energy. Here, a glass pellicle is used. It has a reflectivity of approximately 8% from both surfaces. This has to be taken into account for further calculations. Since the transmission calorimeter is placed in the propagation direction of the laser pulse, it is blocking the Thomson Parabola-MCP assembly. In order to investigate the ions accelerated in target normal direction, the transmission calorimeter is mounted on a movable stage.
Additionally, to measure the 2ω-self-emission, a simple imaging system is used. A microscope objective (by the company *Mitutoyo*) is placed parallel to the target. To ensure that only 2ω-light is detected, a 2ω-filter is mounted in front of the objective.

4.1.1 Spatial and temporal synchronisation

The temporal synchronisation of both beams is done by first spatially overlapping the beams on an angled thin glass slab. The position of the glass slab is fixed in the focus diagnostic of one beam and the focus diagnostic of the second beam is moved accordingly to the same focusing position at an angle of 45° .
The rough synchronisation in hundreds of picoseconds range is done with the help of a photodiode. The path of the heater is variable in length with the help of a

double-pass delay stage. The photodiode is seeing the reflection of both beams and by moving the delay stage and thus lengthening/shortening the beam path, an overlap between both beams is obtained.

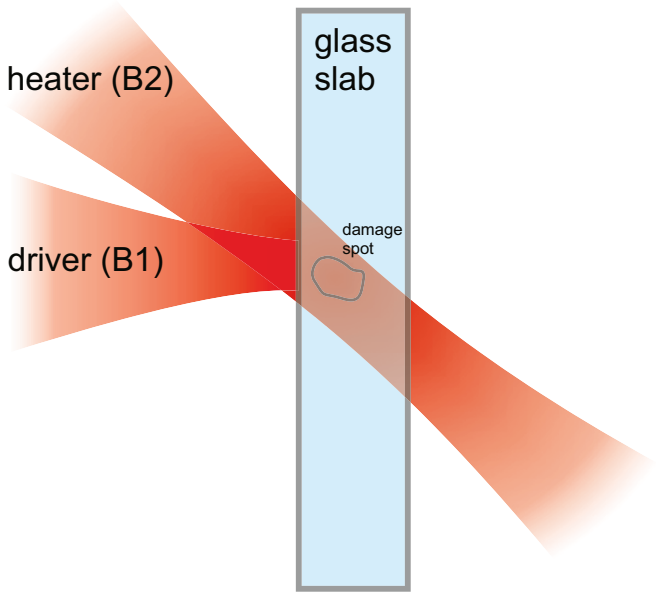

Figure 4.2: Schematic illustration of the temporal synchronisation of the two pulses. The driver is focused onto a glass slab, creating a damage spot which is imaged with the heater. The delay between the two pulses is changed until the damage spot is no longer visible. Eventually, the delay is varied further in smaller steps until the damage spot is just about to appear.

For a more precise temporal synchronisation of both beams, a small damage spot is created by focusing the driver beam on the glass slap with low energy. A schematic illustration is presented in figure 4.2. The damage spot created on the glass slab is imaged by the focus diagnostic of the heater. In order to synchronise both beams, the delay between the beams needs to be varied until the damage spot is slightly visible (as small as possible). With this method, a temporal timing in the picosecond range can be achieved.

4.1.2 Preparation and alignment of ultra-thin flat foil targets

Ultra-thin foils present a rather difficult handling and alignment procedure. However, laser-plasma experiments using ultra-thin foils is an extensively studied

research topic. As demonstrated in [65], new acceleration mechanisms with improved particle beam quality can be achieved by using targets of reduced size.
For the experiments presented in this chapter diamond-like carbon (DLC) foils with a thickness of 50 nm and 100 nm are used. DLC is a type of amorphous carbon which has characteristics similar to diamond such as chemical resistance, mechanical firmness and optical transparency [106].
The DLC foils are stored on a glass plate. Before using the foils, they need to be attached on a mount which is a small round mesh in this case. The meshes are attached on a target holder afterwards. In order to detach the foil from the glass plate the targets need to be floated in distilled water very carefully. Previous to the floating process, the target is slightly cut (in the size and shape needed afterwards) thus detatching easily from the glass plate as soon as getting in contact with water. The detached pieces of the DLC foil will float on the water [107] [108]. Afterwards the foils can be attached very carefully via adhesion on meshes. Since the targets are rather delicate, they need to be handled very carefully. The process of pumping down the vacuum chamber needs to be done very slowly. While aligning the target, the irradiation with a focused high-intensity laser pulse should be avoided. The target material is transparent, which makes it easy to image small structures such as small dust particles. These small particles support the process of positioning the target on the focal plane. Another advantage of the optical transparency of the target is that damages/holes in the target or double layers can be detected easily. The alignment process is repeated for each target.

4.2 Absorption measurements

The investigation of rapidly heated matter has become more attractive since the invention of high-intense and ultra-short laser pulses. The absorption of the laser energy takes place on a very short time scale, before significant hydrodynamic plasma motion can develop. Absorption of an intense laser pulse during the interaction with solid matter has been the topic of many experimental and theoretical papers before [109] [110] [111].
Dual beam interactions open up a new research area. Absorption processes of an ultra-short laser pulse with a preheated plasma introduce a novel and attractive research field. In order to identify the conditions for an efficient coupling of the laser energy into solid matter, theoretical and and experimental attempts have been made, concentrating on the efficent acceleration of ions [112] [113] [114].

In this section, the absorption measurements of the double beam experiment for different laser energies and delays between both beams are presented. The measurements are performed for one experimental set-up configuration: the calorimeter is positioned 15 cm behind the target on the driver laser axis. A second calorimeter is employed to measure the reflected energy. For this purpose a pellicle is placed in the beamline of the driver. The glass pellicle is splitting the beam into two separate paths. In one path of the splitted beam a calorimeter is used in order to measure the reflected energy. It has to be taken into account that both surfaces of the pellicle have a reflectivity of roughly 8 %. By varying the parameters of the driving laser, control the experimental conditions can be controlled. The driver is interacting with the preformed plasma, which is expanding freely in vacuum.
The absorbed fraction of the laser energy can be estimated indirectly by measuring the transmission and reflected energy. The total energy is comprised of the transmitted energy less the reflected energy and can be calculated by:

$$E_T = \frac{E_{transmitted}}{E_{L,on\,target} - E_{reflected}} \times 100, \tag{4.2.1}$$

where $E_{transmitted}$ gives the measured transmitted energy, $E_{L,on\,target}$ the laser energy on the target and $E_{reflected}$ the total reflected energy.

4.2.1 Experimental results

In the following, the effect of the varying delay between the driver and the heater is discussed. The experimental results are presented in 4.3. The transmitted driver energy in % is plotted against the relative delay in ps. The intensity on the target of the heater is 8.5×10^{19} W/cm^2 and the intensity of the driver is varied between 1.23×10^{20} W/cm^2 and 1.91×10^{20} W/cm^2. The target thickness is 50 nm. A larger delay between both beams leads to a higher transmission. The transmission is rising with increasing delay. For example regarding the blue curve, which corresponds to a driver intensity of 1.4×10^{20} W/cm^2, the transmission is decreasing and reaching a minimum at about 30 % at a delay of 400 ps. Soon after the minimum, the transmission is again rising rapidly. Decreasing the laser energy and comparing the transmission curves for the different energies, a similar trend can be seen. For all laser intensities, the transmission is rising and then decreasing again, reaching a minimum. The minimum in transmission is shifting with the driver laser intensity. Decreasing the laser intensity, the minimum is shifting to larger delays. For a driver intensity of 1.49×10^{20} W/cm^2, the minimum in transmission is approximately

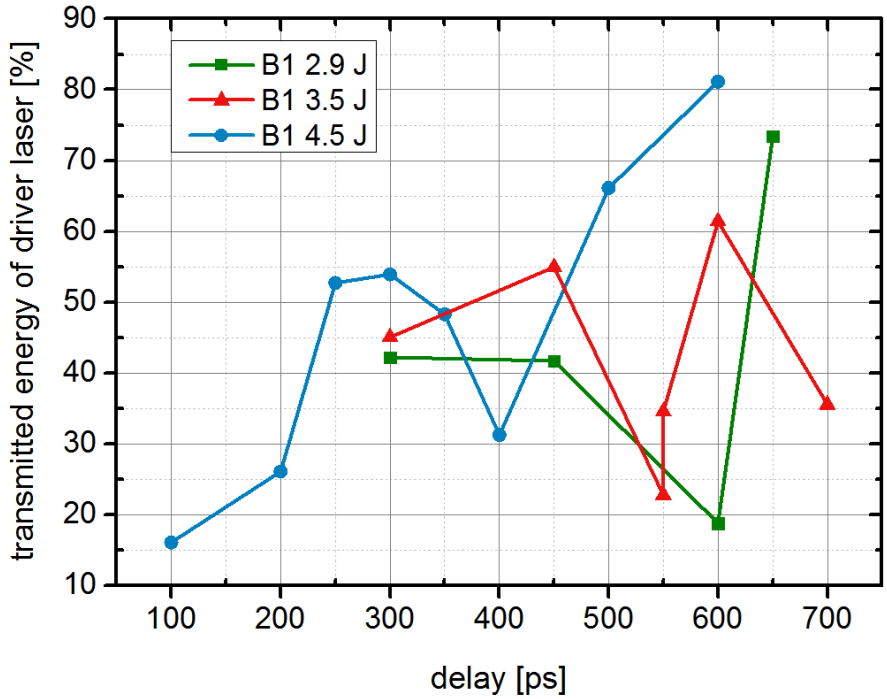

Figure 4.3: Experimentally obtained transmitted energy values of the driver beam at different times of expanded target conditions. The transmission of the driver beam is given in % and is shown against the delay in ps between the two pulses. As targets 50 nm DLC foils have been used. A clear drop in transmission is observed at different time delays depending on the laser energy. The minimum position is shifting towards earlier delays with increasing laser energy. Each data point corresponds to one single shot.

25 % and is occurring at 550 ps. Decreasing the intensity to 1.23×10^{20} W/cm^2, the minimum is shifting to 600 ps and a transmission value of 18 %.

4.2.2 Analytical model

The absorption processes are studied via an analytical model developed by A.P.L. Robinson. The purpose of this model is to assess the extent of the effect of collisional absorption on the propagation of a strongly focussed laser pulse through a plasma of a pre-heated foil target.

In order to elucidate the key physical parameters of the present absorption process, some assumptions are made to simplify the problem. A uniform plasma is treated as expanding adiabatically. Thus the temperature scales with $T = T_0(\ell_0/\ell)^{\gamma-1}$, where ℓ gives the length of the plasma, which is assumed to be essentially planar ($\rho\ell = \rho_0\ell_0$). As also the 2ω-transverse probing images indicate, the transverse

expansion of the plasma is fairly weak compared to the longitudinal expansion. The planar expansion is also confirmed by rad-hydro simulations performed by A.P.L. Robinson.
By assuming paraxial approximation given by

$$I(x) = \frac{I_0}{1 + \frac{x}{\xi_R}}, \tag{4.2.2}$$

where x is the position with the foil centred x = 0 and ξ_R the Rayleigh-length, the propagation of the laser beam through the plasma is considered to be largely undisturbed. Moreover, since the laser is assumed to be able to propagate relatively undisturbed, any absorption process is rather weak and negligible.
Using the dispersion relation and assuming weak collisions, the collisional attenuation coefficient can be obtained, which is given by

$$\mu = \frac{\upsilon_{ei}\omega_p^2}{c^3 k_L^2}, \tag{4.2.3}$$

where the electron-ion collision frequency is determined by

$$\upsilon_{ei} = \frac{Z^2 n_i e^4}{2\pi\epsilon_0}\frac{\gamma m_e}{p^3} ln\Lambda. \tag{4.2.4}$$

The electron momentum is defined by the largest velocity, either the laser quiver velocity ($\upsilon_{os} = eE_0/c\omega$) or the electron thermal velocity ($\upsilon_{th}\sqrt{3k_BT/m}$).
Considering a thermal equilibrium, the expected amount of ionisation for a certain temperature can be determined via the Saha equation [115]

$$\frac{n_i n_e}{n_a} = 2\frac{Z_i(T)}{Z_a(T)}\frac{1}{\lambda_B^3}\exp\left(-\frac{E_i - \triangle E_i}{k_BT}\right), \tag{4.2.5}$$

where $\lambda_B = \sqrt{\frac{2\pi\hbar^2}{m_e k_B T}}$ gives the de Broglie length of an electron, $\triangle E_i \approx \frac{\sqrt{2}}{4\pi\epsilon_0}\frac{e^2}{\lambda_D}$ the ionisation potential lowering and $Z(T) = \sum_m g_m \exp\left(-\frac{E_m}{k_BT}\right)$ the partition function for the ion/atom. Here, the Saha equation is solved for a carbon plasma since DLC targets are used. For each spatial position, the absorption contribution is calculated by the ratio of the plasma area to the beam waist. The plasma area is determined by rad-hydro simulations.
Figure 4.4 shows the collisional absorption (in %) depending on the length of the plasma (in µm). The problem here is expressed in terms of plasma length rather than the time (delay) as in the experimentally obtained data. However, time

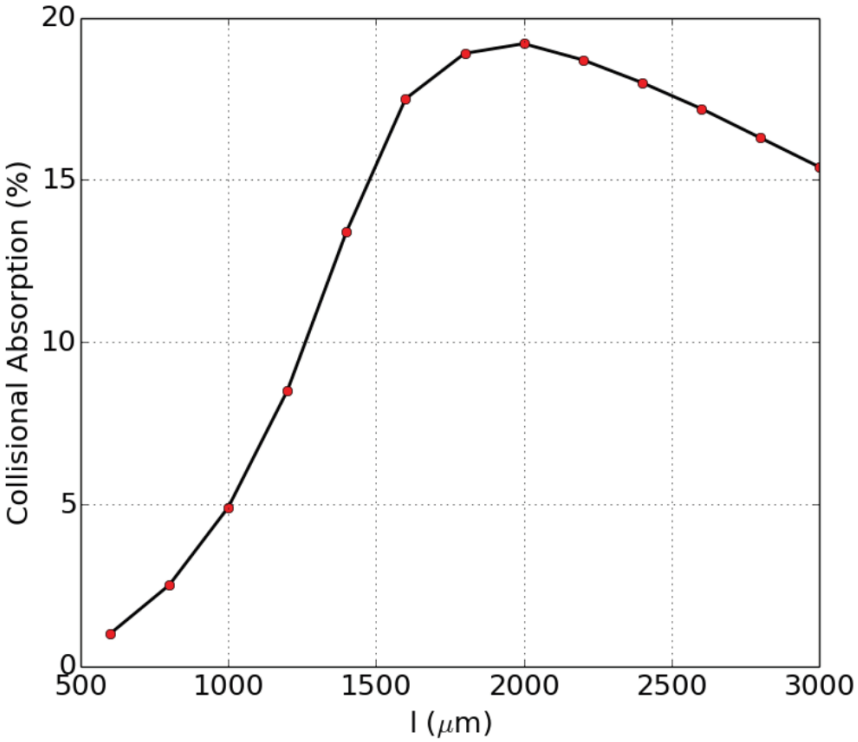

Figure 4.4: The collisional absorption fraction dependent on the plasma length. The magnitude of the absorption fraction reaches about 20 %, which is comparable to the magnitude of the minimum in transmission (cf. figure 4.3). The absorption fraction is not varying monotonically but is reaching a distinct maximum. The results are provided by A.P.L. Robinson.

can just be translated in length, as it allows the plasma to expand further. For the calculations the following parameter values are considered: $\rho_0 = 200$ kg/m^3, $\ell_0 = 1$ µm, $T_0 = 1$ keV, $\lambda = 1$ µm, $\mathrm{I}_L = 10^{20}$ W/cm^2 (at focus), $\omega_0 = 5$ µm and $\xi_R = 20$ µm. The effective area of the plasma is determined by assuming an effective area of 50 µm throughout.

The absorption fraction is increasing with increasing length of the plasma, reaching a distinct maximum. Rather than varying monotonically with the expansion time (or plasma extent), the absorption fraction reaches a maximum at around 20 %, which is comparable to the magnitude of the minimum in transmission recorded in the experiments.

The analytical calculations indicate that collisional absorption delivers an adequate explanation for the experimentally measured transmission data. Both the actual minimum in transmission (maximum in absorption) and the magnitude of the effect can be well correlated with the collisional absorption mechanism. Furthermore,

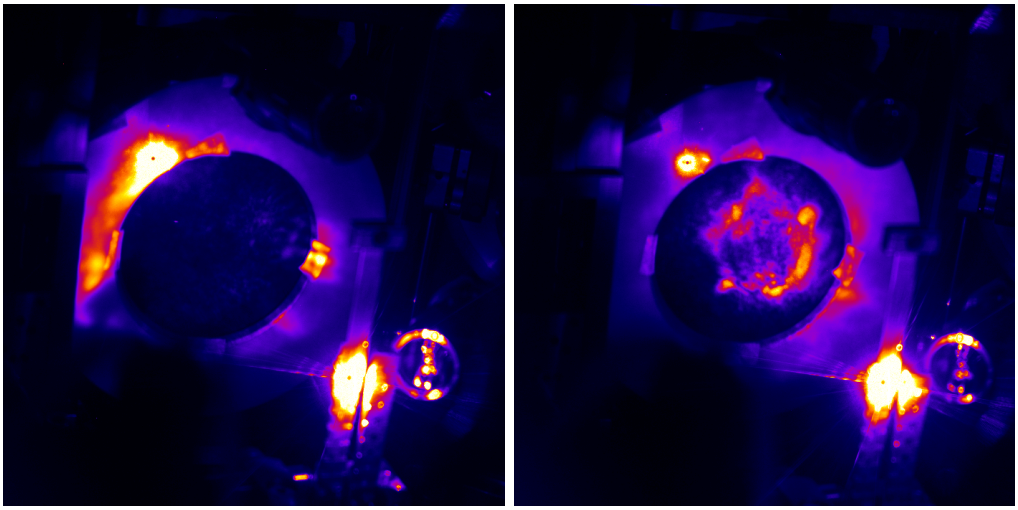

(a) 600 ps (b) 650 ps

Figure 4.5: Two exemplary images of the calorimeter surrounded by a PTFE. On the left-hand-side, the delay between both beams is 600 ps and on the right-hand-side 650 ps. Comparing to the absorption measurements, an apparent correlation can be seen. At the dip position, the beam shape and size on the calorimeter are defocused compared to the beam size at 650 ps.

other experimental diagnostics, such as 2ω-probing images and monitoring of the calorimeter, support the experimental findings.

4.2.3 PTFE

By employing a **P**oly**t**etra**f**luor**e**thylen (PTFE) screen imaged by a camera the actual beam size can be monitored. The PTFE screen is placed directly in front of the calorimeter in the forward direction (laser direction). The detector part of the calorimeter is not covered by the PTFE screen and thus the beam size and shape can be monitored while measuring the absorption.
In figure 4.5, two exemplary images of the calorimeter with the PTFE in front of it are shown. These two images show the calorimeter and the PTFE at different experimental conditions. Both images are taken for the same driver and heater intensities (driver: 1.27×10^{20} W/cm^2, heater 8.9×10^{19} W/cm^2) but at different delays. The image on the left is for a delay of 600 ps and the image on the right is for a delay of 650 ps.
It is noticeable that at 600 ps, at the minimum of the transmission curve, the imprint of the beam on the calorimeter is much weaker. This feature is in good

agreement with the measured transmission data.
The transmission is less at 650 ps and at the same delay, the beam imprint on the calorimeter is weaker which indicates a higher absorption (less transmission). Comparing to the images at other delays, it is obvious that the transmission is scaling with the intensity of the beam imprint on the calorimeter.
However it is difficult to rescale the beam size by using the PTFE images. Since the camera is integrated, it is difficult to distinguish between the background and real beam. All the scattering from the various objects inside the target chamber are contributing to the signal recorded on the camera, thus making it difficult to reconstruct the actual beam size and shape. Nevertheless, the PTFE images are a convenient indication for the interaction between the high intensity laser pulse and plasma. The pulse shape on the calorimeter implies a diverged beam profile after the interaction at the minimum transmission position.

4.3 2ω-probing

High intensity laser-plasma interactions are connected to the coupling of the laser energy into plasma electrons. The interaction of the laser with the electrons is mostly the main driver for different phenomena. For example, high harmonics can be generated due to the oscillations of electrons at the critical surface [116]. Moreover quasistatic electric fields caused by charge separation can accelerate ion beams (e.g. Coulomb explosion [117] [118], TNSA [60] or shock acceleration [119]). As already shown in [112], for very thin already exploded targets, the ion acceleration is enhanced, if the laser is able to propagate completely through the target. A channel is formed and the hot electron beam is collimated due to the electric fields within the channel. The electric fields on the rear side of the target are enhanced, which results in an enhanced proton acceleration [120] [121].
In the following, the penetration of a high-intensity laser pulse through an already exploded foil (and hence an expanded plasma) is investigated.
As already mentioned above, in this experimental arrangement, the heater (B2) is impinging on a thin foil preforming a plasma and subsequently (few hundreds of picoseconds later) the driver (B1) is interacting with the expanding plasma. Since the delay between both pulses reaches few hundreds of picoseconds, the preformed plasma has already expanded and the density has become low enough for the driver beam to propagate through. The consequent channel formation is imaged by an imaging system transverse to the driver direction, where the light collected by the

objective of the imaging system is spectrally filtered, i.e. the second harmonic of the interaction pulse. Consequently, time-integrated second harmonic emission from the plasma is also imaged onto the camera. Plasma emission is in general the generation of escaping radiation near the plasma frequency (or its harmonics) [122]. Resulting from the high energy of a plasma, the atoms and ions in a plasma are excited to higher electronic states. During the recombination from the excited state, they emit light. The 2ω-emission gets more intense after the self-focusing of the beam in a low density plasma [123].
For simplicity reasons, the propagation of the laser pulse through the plasma can be derived by assuming the circular wave-guide equation. In the following, the channel generation and the obtained experimental results will be discussed.

4.3.1 Channel formation

The formation of a channel in a plasma is depending on the electron acceleration length. For near-critical density targets the acceleration length is determined by the laser depletion length. This is the length at which all the laser energy is converted into electron energy [124] [125].
Considering the interaction of an intense laser-pulse with a near-critical density target, it can be assumed, that the walls of the self-generated channel will have high density. Thus the laser pulse will not be able to penetrate these. Therefore, the laser pulse will be contained completely inside the self-generated channel. Hence, the laser pulse energy can be estimated by using the well-known solution for the propagation of an electromagnetic wave inside a waveguide [126] [127].
Assuming the laser pulse energy is equal to the energy transferred to the plasma by the electrons, the channel length can be derived. The laser pulse energy inside a self-generated plasma waveguide is given by [124]:

$$E_L = c\tau_L \pi R^2 K m_e c^2 n_c \left\langle a^2 \right\rangle, \tag{4.3.1}$$

where R is the channel radius at the intensity $1/e^2$ and for linear polarisation $\langle a^2 \rangle$ is found to be $\frac{1}{2}a_o^2$ (the maximum value of the laser pulse dimensionless vector-potential). The factor K is dependent on the spatial and temporal profiles of the laser pulse. It is a result from the integration over the laser pulse volume [120].
The energy transferred to the plasma electrons is given by:

$$E_e = \bar{\epsilon_e} n_e \pi R^2 d, \tag{4.3.2}$$

with d the channel length and $\bar{\epsilon_e}$ the energy of an electron gained in the laser field. For electrons being accelerated out of the channel in the transverse direction, the electron energy can be estimated by $\bar{\epsilon_e} = a_0 m_e c^2$ [124].
Using equations 4.3.1 and 4.3.2 and assuming the electron energy to be equal to the laser energy, the channel length can be easily derived:

$$d = K c \tau_L \frac{a_0}{2} \frac{n_c}{n_e}. \tag{4.3.3}$$

Therefore, the channel length is proportional to a_0 and is depending on n_e.
Usually, laser light is unable to propagate through an overdense plasma, since the plasma density is greater than the critical density ($n_e > n_{cr}$). If the laser intensity is high enough, the electrons oscillate at close to the speed of light. This leads to a reduced plasma density and switches the plasma from optically opaque to transparent. The laser is then able to propagate though the plasma.

4.3.2 Experimental results

Employing a simple imaging system, the channel formation can be monitored. Figure 4.6 shows experimentally obtained transverse 2ω-probing images for different time delays. The interaction target is a 50 nm DLC foil and the laser energy on the target is 1.5×10^{20} W/cm^2. The interaction is shown for 450 ps (a), 600 ps (b) and 700 ps (c). The accuracy of the spatial overlap between the two beams is 10 µm. It is noticeable, that both beams are not impinging on the same spatial point. The distance between the beams is 15-20 µm. However, since the heater (B2) is coming earlier, the second beam (driver, B1) is interacting with an already expanded almost homogeneous plasma. The spatial overlap between the two beams will not cause a big error in the measurements since the expanded volume of the plasma is greater than the accuracy in spatial overlap between the two beams.
A stronger signal in the 2ω-channel implies a stronger electron signal. More electrons are interacting with the plasma channel and more self-emitted light can be observed. A stronger signal indicates a stronger self-focusing of the laser beam. Comparing the images in figure 4.6, it is striking, that for larger delays a stronger signal can be seen. The stronger signal is occurring at the same delay as the dip position in transmission is observed and a strong correlation between these two values can be concluded. Since the beam is stronger focused while passing through the plasma at a specific delay, more energy is absorbed and a drop in transmission is observed. The experimentally obtained data is presented in figure 4.7. The second

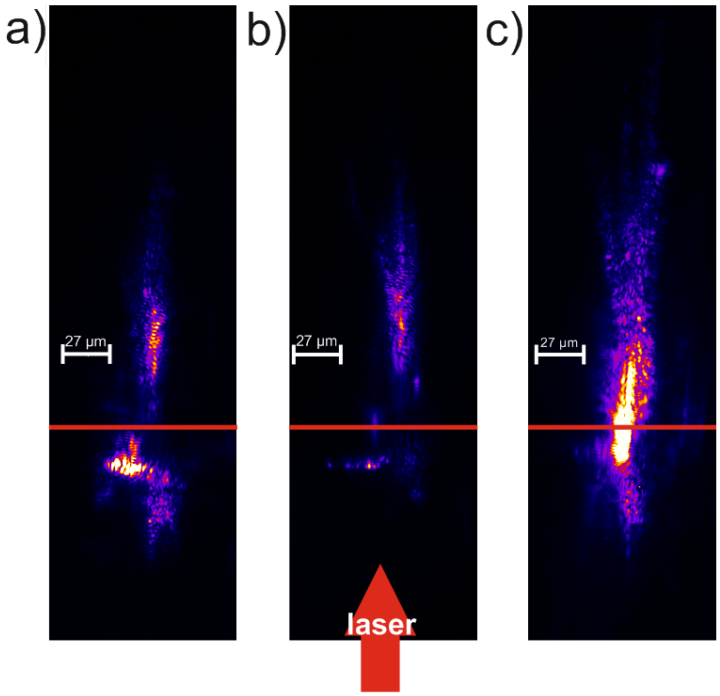

Figure 4.6: Experimentally obtained 2ω-transverse probing images showing the channel formation at different time stages of the interaction. Exemplary, the interaction is shown at a) 450 ps , b) 600 ps and c) 700 ps . All three images are taken at similar experimental conditions: the target thickness is 50 nm DLC and the laser intensity on the target is $1.5 \times 10^{20} W/cm^2$. With increasing delay, the longitudinal channel length is also increasing. A significant increase in transversal channel width is not visible. A stronger focusing of the laser beam can be observed at larger delays. The red arrow is indicating the direction of the laser beam and the red bar is illustrating the position of the target.

beam (heater) is always coming earlier than the interaction beam (driver). At a fixed laser intensity, the longitudinal channel length is increasing with increasing delay. The transversal channel length is not changing considerably with increasing delay between two pulses.

Changing the laser intensity at a fixed delay also shows an increase in the longitudinal channel length with increasing laser intensity. In figure 4.8, the channel length is plotted against the dimensionless laser parameter a_0. In both cases, the longitudinal and transversal channel formation, the channel length is increasing with increasing a_0. Increasing the dimensionless parameter implies increasing the laser intensity. With increasing intensity, the laser pulse can propagate longer through the plasma and thus the channel length is larger. For the longitudinal case,

the dependency is much clearer. The transversal channel length is not changing significantly.

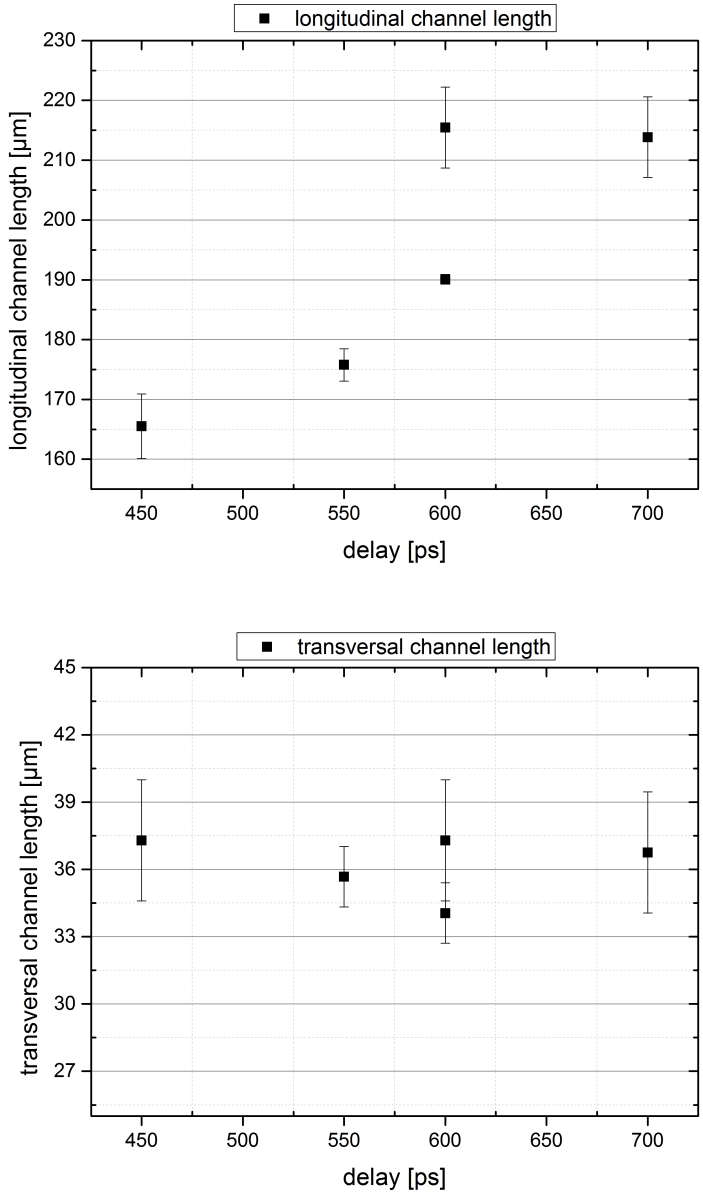

Figure 4.7: The graphs are showing the 2ω-channel length obtained during the interaction of a high-intensity laser pulse with a pre-heated target. On the top, the longitudinal channel length is presented with respect to the delay between the heater and driver beam, whereas on the bottom, the transversal channel length is demonstrated. A significant behaviour can be identified regarding the two lengths. While the longitudinal channel length is increasing with the delay, the transversal channel length is not changing significantly.

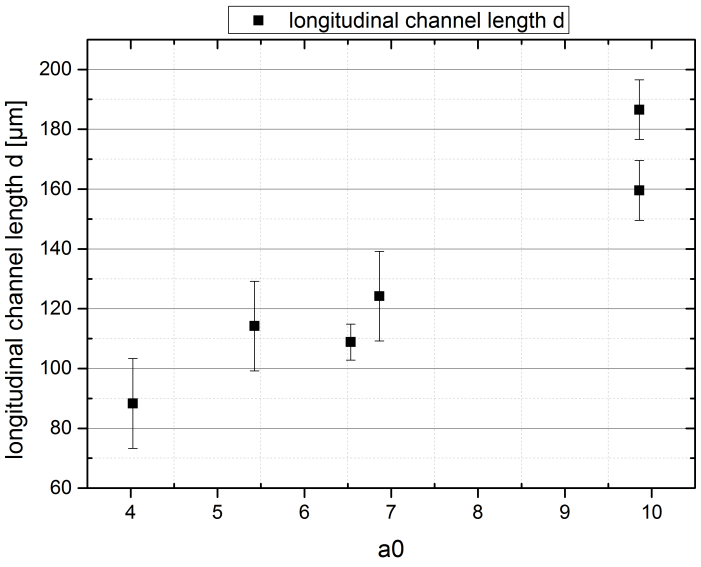

(a) Longitudinal channel length.

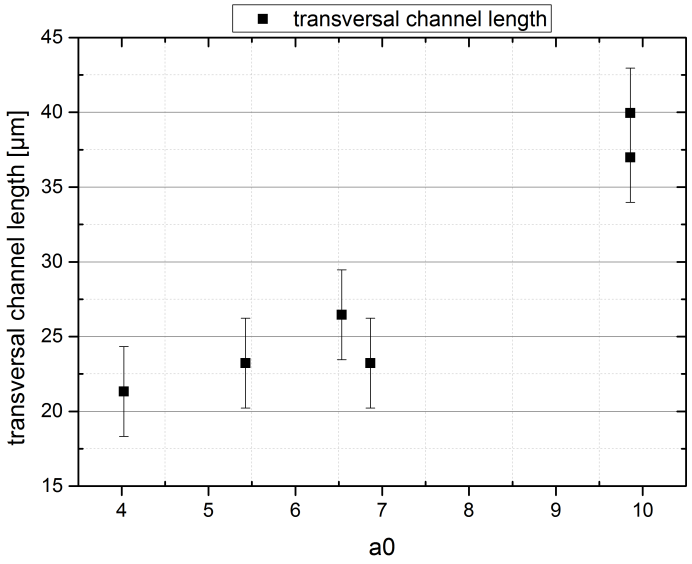

(b) Transversal channel length.

Figure 4.8: The two graphs are showing the longitudinal channel length (top) and the transversal channel length (bottom) with respect to the dimensionless laser parameter a_0. The channel is increasing in both cases with increasing dimensionless parameter a_0. The longitudinal channel length is increasing more significant with a_0 than the transversal channel.

As the delay between both pulses is increasing, the density of the plasma is

decreasing and the plasma becomes underdense enough, and thus the penetrating laser pulse can be self-focused. The limiting case for self-focusing can be determined by formula (cf. equation 2.6.2). Therefore, the plasma density needs to be estimated, which can be done using the formula 4.3.1. By assuming cylindrical geometry, the volume of the expanding plasma can be calculated. As a starting volume, a laser spot size of $1/e^2 = 1.35$ µm is chosen (almost 4 times larger compared to FWHM = 0.5 µm). Assuming that the initial number of electrons stays the same, the electron density at different delays and accordingly different stages of plasma expansion can be calculated. For a laser energy of 1.35 J, the laser power on the target is 45 TW. Compared to the critical power at a time delay of 450 ps which is about 6.5 TW, the laser power on the target is above the threshold for relativistic self-focusing. For early time delays, relativistic self-focusing cannot be observed, since the plasma density is too high. As already seen in figure 4.3, the absorption of the laser energy is higher at early time delays. Depending on the laser energy, the plasma density at a specific time delay is low enough, and thus relativistic self-focusing can occur. Due to relativistic self-focusing, the γ-factor is increasing and changing the effective plasma frequency.

4.4 Ion acceleration

Laser-accelerated ions/protons are detected by a Thomson parabola spectrometer assembled with an microchannel plate (MCP). The proton cut-off energies can be derived from the traces obtained on the MCP (cf. chapter 3.2). For this purpose, a MatLab code provided by A. Alejo Alonso is employed. For each recorded image on the MCP, the ion traces are simmulated by the MatLab code by adjusting the ion energies, ion species and parameters of the Thomson parabola settings. Subsequently, the cut-off energies of each trace can be extracted.
In the following, the dependence of the proton cut-off energies on the two laser pulses is going to be discussed. Different parameters such as laser pulse energy and delay between both beams are varied.

4.4.1 Single beam interaction

Firstly, the single beam interaction will be presented. As mentioned above, the intensity of the driver (B1) is varied between 1.23×10^{20} W/cm^2 and 1.91×10^{20} W/cm^2 the intensity of the heater (B2) is kept constant at 8.5×10^{19} W/cm^2. In both cases, 50 nm DLC targets are used. Exemplary MCP images for both cases are

shown in figure 4.9.

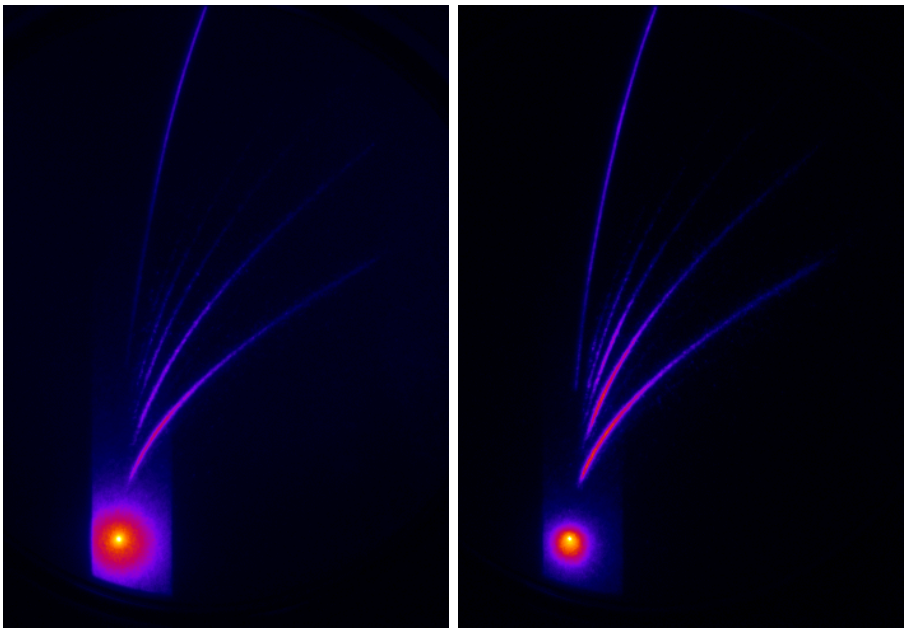

(a) Reference image for driver. (b) Reference image for heater.

Figure 4.9: Ion traces on MCP for single beam interaction for one single shot. The image on the left gives a reference for the driver and the right one for the heater.

Here in this example, the laser energy on the target is $E_d = 0.85$ J for the driver and $E_h = 0.48$ J for the heater. The different traces belong to different ions being accelerated by the laser pulse. Both beams accelerate protons and carbon ions, which originate from contamination layers on the foil target. The higher intensity of the driver leads to a higher proton cut-off energy. Protons accelerated by the driver reach a cut-off energy of $E_p = 2.8$ MeV and protons accelerated by the heater $E_p = 3.4$ MeV.
Nevertheless, the main driver in the dual beam configuration is the heater (B2), since in the experiments the heater is always coming earlier than the driver (B1). In the following, the results for the proton/ion acceleration in the dual beam configuration are going to be presented.

4.4.2 Dual beam interaction

An exemplary MCP image recorded during a dual beam interaction is shown in figure 4.10.

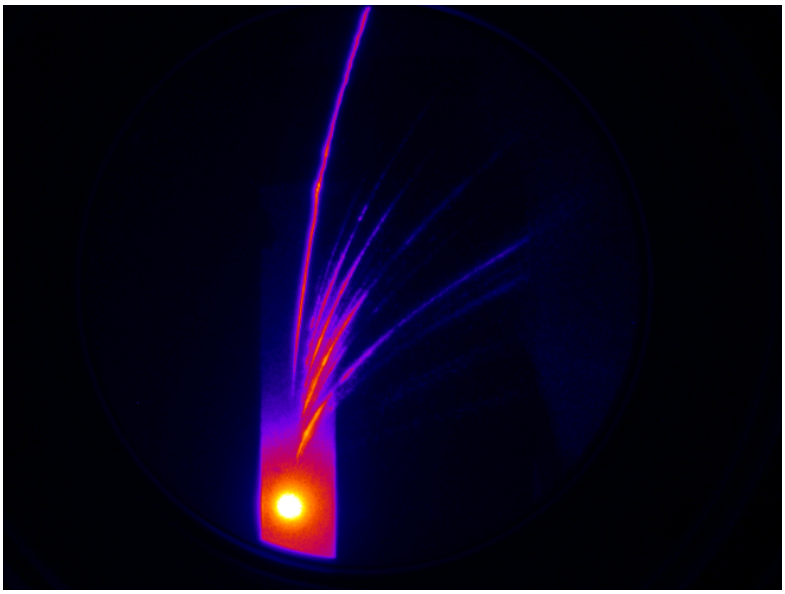

Figure 4.10: Accelerated ion traces on the MCP in a dual beam arrangement recorded for one single shot. The delay between the two pulses is 600 ps.

The experimental conditions are comparable to the conditions during the absorption measurements. As a target a 50 nm DLC foil is chosen, which is irradiated by the two pulses with an energy (on the target) $E_d = 0.775$ J for the driver and $E_h = 0.55$ J for the heater. Here, the delay between both beams is 600 ps.
Comparing the images to the single beam interaction a difference in the accelerated ion traces can be seen. In case of dual beam interactions more ions traces seem to appear. Apparently a larger fraction of the ions on the contamination layer are accelerated during the dual beam interaction than in the single beam interaction.
Another striking feature of the dual beam interaction can be seen in the accelerated proton energies. Figure 4.10 shows an exemplary MCP image of the double beam interaction. The maximum cut-off energy of the protons is 5.9 MeV in this case. An enhancement of approximately a factor of two is achieved.
As in the transmission measurement scan, the dependence of the proton (ion) energy on the delay between the two pulses is investigated.

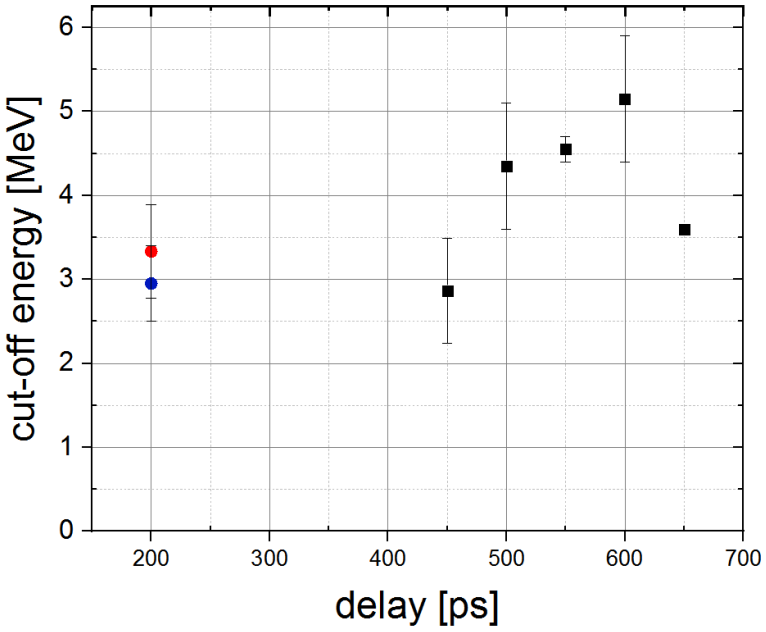

Figure 4.11: Cut-off energies dependent on the delay. The energy of the heater on the target is 0.5 J and of the driver 0.75 J. The red and blue spot show the energies for a single beam shot for the driver and heater, respectively. In order to provide a convenient resolution, the single beam shots are presented at a delay of 200 ps. The energies are averaged over several shots.

In figure 4.11, the maximum achieved proton energy dependent on the delay is shown. The delay is varied in a picosecond-range up to 600 ps, where the heater (B2) is always coming earlier. At late delays, the proton energy already exceeds the energy of the accelerated protons with only one beam. Comparing the energy of a single beam shot with only the heater and a double beam shot at 600 ps, it is notable that the proton energy almost enhances by a factor of 2 with respect to the single heater shot. Even though higher proton energies can be achieved with the driver (since the intensity/energy is higher compared to the heater), the single beam interaction with only the heater needs to be considered. Since the heater is coming a few hundreds of picoseconds earlier than the driver, B1 has little/no chance to accelerate protons via TNSA.

Interestingly, the maximum proton energy is coinciding with the dip position of the transmission measurement. Figure 4.11 shows the accelerated proton energy dependent on the delay between the two pulses. The same target and laser conditions as shown in figure 4.3 are valid. Intriguingly, it can be seen that at the same delay of 600 ps, where the minimum in the transmitted energy could be measured, the maximum proton energy is recorded (cf. green curve in figure 4.3).

Previous studies as in [128] demonstrated the efficient acceleration of protons from already exploded foil targets. Generally, in laser-solid interactions the most energetic ions are accelerated from the rear side of the target by the well-established TNSA mechanism (cf. section 2.5.1). A strong electrostatic field on the rear side of the target is generated by fast electrons, which is accelerating the protons. Compared to the robust TNSA mechanism, an enhanced efficiency of the laser-driven protons and ions is reported from already exploded foils. As discussed above, the plasma density is quite low due to the already irradiated and expanded target (cf. section 4.2). This low density leads to a heating of the electrons in a rather large volume, which is yielding a higher absorption of the laser energy. A higher absorption at a particular delay was confirmed experimentally as already presented in the previous section.
At these low densities, ions are most likely accelerated via a shock-like mechanism. This regime strongly depends on the features of the density gradient. In [128] [129], the dependence of this shock-like acceleration mechanism on different target and laser parameters was studied. The influence of the plasma scale length, target density and length of the plasma on the efficiency of the acceleration process is reported. For example, the maximum proton energy (in MeV) is given depending on the target density. It was shown that a maximum in proton energy is found at a target density around $0.15n_c$ [114]. As also shown in [130], a collimated multi-MeV ion beam was observed at high laser intensity in case of low density gas targets (i.e. $0.1n_c$).
In [112], the acceleration of laser-driven protons is studied for different target thicknesses. The highest energies of laser accelerated protons are observed for solid density foil targets and near-critical-density targets. Two effects are found to conduce to the reduction of the accelerating field in thin targets. For thinner targets, larger rear-surface gradients are observed and lower target densities reduce the absorption fraction of the laser energy.
Similar ultra-thin foil targets are used in the experimental investigations presented in this chapter. As already shown in figure 4.11 for a distinct delay (i.e. distinct plasma density), an enhanced ion energy is observed. The absorption measurements revealed that for this particular delay, collisional absorption comes into play, thus diminishing the limiting factor of less absorption of the laser energy. Since the laser is able to propagate through the plasma as observed in the 2ω-probing images, more electrons can efficiently be generated at the rear side of the target/plasma and the proton accelerating field (sheath) can be increased locally.

Collisionless shock acceleration

High intensity laser pulses incident on a plasma can induce the formation of strong electrostatic shocks.

Macroscopically, a shock can be described as a change of the medium along the propagating transition layer [131]. Collisionless electrostatic shocks are propagating for Mach numbers $M > 1$. The Mach number is a dimensionless quantity in fluid dynamics, which is giving the ratio of flow velocity to the (local) speed of sound of the surrounding medium ($M = \frac{v}{c_s}$). A shock wave can also be characterised by a sheath moving through a plasma. The idealised potential of a shock wave is shown in 4.12. The potential function $\phi(x)$ would be consistent in the frame moving with

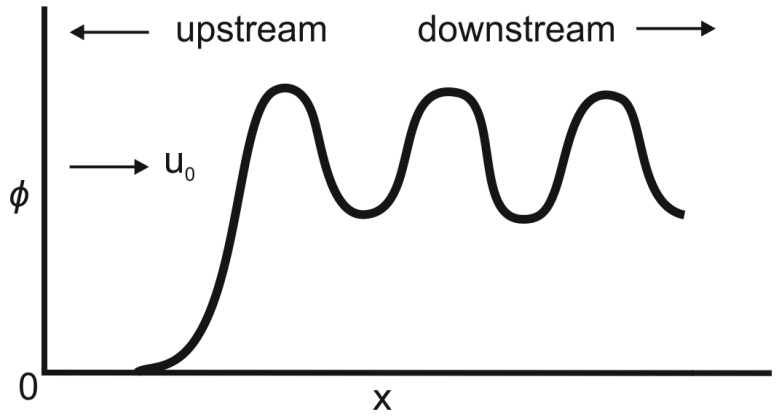

Figure 4.12: Idealised potential distribution of an ion acoustic shock wave. The wave is moving to the left and ions stream into the wave in the frame of the wave. This potential is given for a soliton solution (cf. [39]).

the wave and ions would stream into the wave front with a velocity u_0.

The radiation pressure of the laser light acts like a piston driving the shock. The shock velocity can be estimated by a flow momentum balance ($m_i(n_i v_p \sim I/c)$), yielding [131]

$$v_p = \left(\frac{I}{m_i n_i c}\right)^{1/2} = \left(\frac{Z}{A}\frac{m_e}{m_p}\frac{n_e}{n_c}\right)^{1/2} a_0 c. \tag{4.4.1}$$

Note that the velocity of the ion piston is determining the shock velocity. For a shock to be able to propagate through a hot plasma, $v_s \approx u_p$ needs to be given, which is the case for $u_p > c_s$. Also, fast electron heating can drive a shock by generating a strong density gradient.

Ions, which are ahead of the shock front, are reflected by the moving potential ϕ, depending on the barrier height and initial ion energy. Initially at rest and $Ze\phi_{max} > m_i v_i^2/2$, ions can reach velocities up to $2v_s$ by elastic reflection from the

moving barrier.

A combination of the collisionless shock acceleration and the target normal sheath acceleration is reported in [113]. This combined mechanism is called low density collisionless shock acceleration (LDCSA). In this acceleration mechanism, the shock front acceleration mechanism is combined with the volumetric low density TNSA mechanism and is most effective for low density plasmas with large scale gradients. The shock is generated not by the laser but by the protons propagating downwards the density gradient [113].
Firstly, ions are accelerated in the same way as in the TNSA mechanism described in a previous chapter (cf. section 2.5.1) due to a sheath field generated by the hot electrons. At the rear side of the target, a smooth density gradient is built up. The electric field is decreasing monotonously and thus ions in the lower density region are experiencing a lower electric field. An electrostatic shock front is formed as ions from higher density regions overtake ions from lower density regions. Ions which are ahead of the shock can be reflected by the shock front as described above. Note that ions accelerated by collisionless shock acceleration are quite broadband due to the non-uniformity of the plasma and the non-uniform velocities of the ions ahead of the shock front, leading to a non-monoenergetic ion beam.

4.5 Previous simulation studies

Simulations performed in [112] showing the maximum accelerated proton energy accelerated from a low density plasma are demonstrated in figure 4.13. The 1D PIC simulations show the dependence of the proton energy and the absorption fraction on the density. On the left-hand-side in figure 4.13 the maximum proton energy (black circles, left scale) and the absorption fraction (green triangles, right scale) are shown against the density profile, respectively. The simulations are carried out at a peak density of $0.1n_c$. With an increasing density profile, the absorption fraction is increasing while the maxium proton energy is decreasing. Note that these simulations are 1D and different factors such as laser propagation through a thin exploded target are not considered. Contrary to the results presented above, the simulations do not show a maximum in the absorption fraction which might be because collisional absorption processes are not considered. However, it is shown in figure 4.13 b) that the maximum proton energy is strongly dependent on the density profile of the plasma. The sharper the profile, the higher are the accelerated proton energies. In [114] the evolution of the maximum proton energy is presented

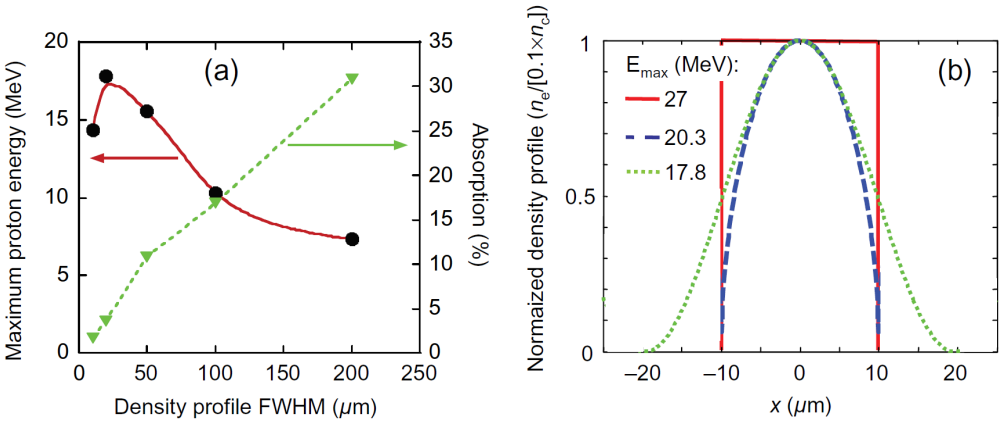

Figure 4.13: Simulations showing the maximum proton energy accelerated from a low density plasma. On the left-hand-side of the image a)) the maximum proton energy (left scale, black circles) and the absorption fraction (right scale, green triangles) are presented against the density profile. On the right hand side, the normalised plasma density profile is presented. The absorption fraction and the maximum proton energy are strongly dependent on the density profile. The highest proton energies are achieved with a sharp plasma density profile [112].

as a function of target density. Figure 4.14 shows the 1D PIC simulation results. The simulations reveal that the shock like acceleration regime strongly depends on the density gradient. As can be seen in figure 4.14, higher proton energies can be achieved with lower density. A sharp density gradient, as in the TNSA mechanism, the most energetic protons are accelerated at the back surface of the target. For an intermediate density gradient, the most energetic protons are accelerated via a shock-like acceleration mechanism. The protons are accelerated in the decreasing density ramp. If the density gradient is too small, wave breaking is observed and becomes the dominant acceleration mechanism.

The experimental data is comparable to the previous works mentioned above. However, the absorption fraction in the previous papers is not coherent with the ones measured in the experiments in this thesis. For future simulations and investigations the collisional absorption processes, which seem to play an important role as described above, need to be taken into account.

4.6 Conclusion

In this chapter the plasma dynamics from a dual beam experiment employing two high-intensity, ultra-short laser pulses were presented. Various diagnostics

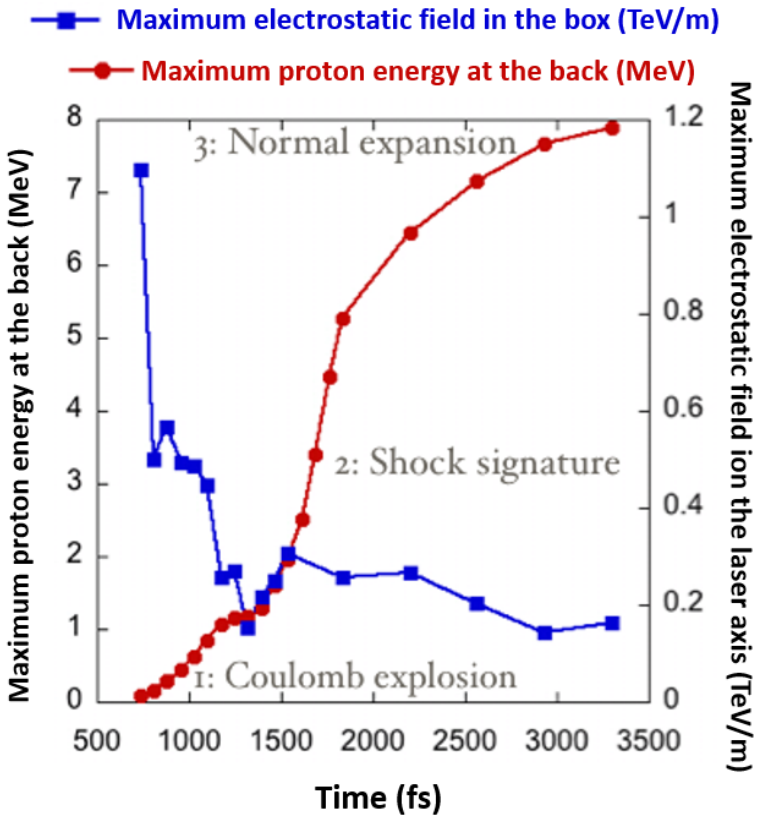

Figure 4.14: The maximum proton energy (left scale) and maximum electrostatic field on the laser axis (right scale) depending on the target density. The time gives the expansion time of the target and thus translates to the density of the target. Later times mean more expansion and thus lower density. The maximum proton energy is increasing with decreasing plasma extent. The simulations are performed in [114].

were used, in order to receive a broad analysis of the dynamics. Highly interesting features which are confirmed by the different diagnostics could be observed. Varying the delay between the two pulses, it was possible to investigate the interaction between an expanding plasma and a high-intensity laser pulse. Considering rather late delays where an already expanded and rather underdense plasmas would be expected, the transmitted laser energy is reaching a minimum point. Analytical calculations revealed that collisional absorption mechanisms become relevant at late delays. The time delay between the two pulses just translates to the extent of the expanded plasma. A maximum in the calculated absorption fraction is found, which can explain the minimum in the experimentally measured transmission.
The results from previous studies [112] [114] [129] are comparable to the experimental study presented in this thesis. However, future investigations should hold out the prospect of performing simulations with the target parameters used in the

experiments presented in this thesis, since these were slightly different in the above mentioned papers. Additionally, collisional absorption processes should be taken into account, since they seem to play an important role determining the absorption fraction.
Another striking feature is observed in the accelerated ion/proton energies. While the transmission is reaching a minimum, the energy of the accelerated protons is reaching a maximum. Compared to the single beam interaction, the cut-off energy of the accelerated protons is increased by almost a factor of two.
Employing an imaging system transverse to the interaction direction allows to monitor the channel length of the laser pulse propagating through an expanding plasma. By varying the delay between the two pulses, different stages of the preheated target could be observed.

5 Parametric study of laser-driven electromagnetic pulses on solid surfaces

Previous studies revealed positive charging of a laser irradiated target up to MV potential range [100] [132], which is due to the escape of relativistic electrons from the irradiated area. The following charge separation leads to a surface electromagnetic pulse along the target. This electromagnetic pulse travels from the interaction point towards the ground at nearly speed of light [132] and the targets are discharging. Using two intense laser beams allows generating the electromagnetic pulse with one beam and use the second beam to generate a proton beam for probing. Here, the ultra-fast dynamics along a wire are analysed which allows controlling the interaction. By folding the wire, the travelling path of the electromagnetic pulse can be adjusted, and thus the interaction can be timed in such a way, that it can be captured in the field of view of the probing protons. As discussed above, the unique properties of a proton beam provide a temporal study of the transient electromagnetic field. Another valuable advantage of the proton probing technique is the visualisation of the interaction. It simplifies the analysis and illustrates splendidly the dynamic process of the charging of a wire target.

An improved understanding and knowledge of the electromagnetic pulse will be a guidance for the post acceleration mechanism [133] [134] [135] [136]. An analytical model presented in [133] indicates an optimum laser pulse duration and a strong dependence of the electromagnetic pulse amplitude on the laser energy.

Particle-tracing simulations are carried out by using the particle tracing code PTRACE [32] in order to define the linear charge density. The particle tracer allows identifying the charge at a fixed probing time and a certain position on the wire target, taking the arrival time and time of flight of the probing protons into account.

This chapter will present a detailed study of the parameters influencing the electromagnetic pulse which are essential for an efficient post-acceleration mechanism. Additionally, the studies will set a benchmark for the scaling of the acceleration efficiency at short pulse multi-petawatt laser facilities available in near future, e.g. [137] [138]. Some parts of this chapter are already published in [139].

5.1 Experimental set-up

The set-up for the experimental study of the electromagnetic pulse is shown in figure 5.1.
In a dual beam configuration, one of the ultra-intense laser pulses is irradiating a 6 **µm** aluminium foil attached to a 80 µm Aluminium wire, while the second ultra-intense pulse is irradiating a 10 µm gold foil generating the probe proton beam. The angle of incidence on the target attached to the wire (*interaction target*)

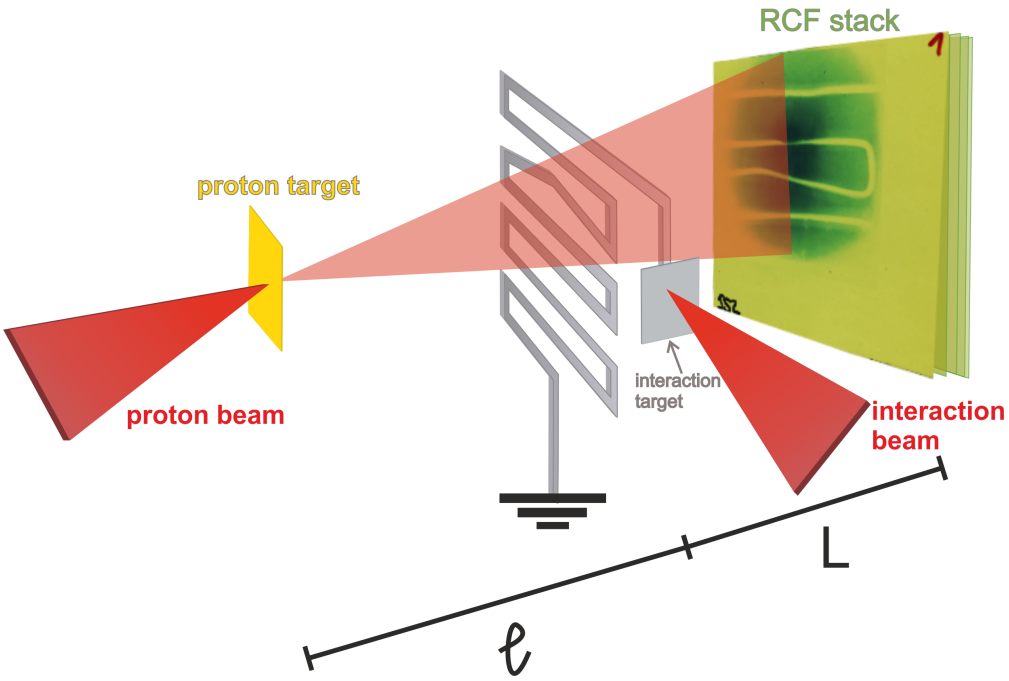

Figure 5.1: a) Experimental set-up for probing of the electromagnetic pulse. Two beams are employed to accelerate protons and to generate the electromagnetic pulse, respectively. The square wave pattern of the wire target allows observing more in the field of view of the proton beam.

is 25°. The beam is focused by an off-axis F/2 parabola to a Gaussian focal spot of $\sim$ 4 µm focal spot size at FWHM. This beam hereafter will be called *interaction beam* in this experimental arrangement. The intensity of the interaction beam on the target is varied between 4.3 $\times$ 10^{18} W/cm^2 - 1.1 $\times$ 10^{20} W/cm^2. The energy and pulse duration are varied to investigate the effect on the electromagnetic pulse amplitude. The second beam used for accelerating protons from a thin foil for probing is also focused to a $\sim$ 4 µm focal spot size at FWHM by an F/2 off-axis parabola, which will be called *probe beam* hereafter. The resulting intensity on the proton target is I = 2 $\times$ 10^{20} W/cm^2. The angle of incidence on the proton target

is also 25°.
A particular target (wire) design (as shown in figure 5.1) is used to investigate the electromagnetic pulse relatively far away from the interaction region. In order to maximise the observable wire length within the field of view of the probing beam, the wire is folded to a square wave pattern (SWP). This shape of the target allows to delay the electromagnetic pulse. The spatial confinement of the electromagnetic pulse can be controlled and thus it can be captured in the field of view of the proton beam.
As shown in figure 5.1 b), the SWP wire is folded into eight segments. Each horizontal segment has a length of 5 mm ± 200 µm and each vertical one has a length of roughly 500 µm ± 50 µm, and thus the spacing between two segments is < 500 µm. The distance between the interaction foil and the top of the first winding of the wire in the SWP arrangement is approximately 3.5 mm.
The geometrical magnification can be calculated as described in section 3.5. Considering L (the distance between the detector and the interaction point) to be $\sim 40 \pm 1$ mm and $\ell = 4.5 \pm 0.5$ mm (the distance between the proton target and the interaction point) leads to a magnification of $M \simeq 1 + \frac{L}{\ell} \approx 8 - 9$.
As a detector, a stack of RCFs with a size of 5×5 cm is used, positioned in the direction of the probing beam (cf. chapter 3, section 3.4).

5.1.1 Spatial and temporal synchronisation

The spatial and temporal synchronisation in this experimental configuration is performed by firstly overlapping both beams spatially. For this purpose, a thin wire ($\sim$ 20 µm Aluminium) is imaged in the focus diagnostic of the proton beam. Subsequently, the position of the focus diagnostic and wire are fixed. The same wire is imaged in the focus diagnostic of the interaction beam which is at an angle of 45° to the proton beam. In this way, a spatial overlap between both beams in µm-range is ensured.
A rough temporal synchronisation between the two pulses is determined with a fast photodiode and oscilloscope. This method delivers a rough timing in nanosecond range. A fine temporal synchronisation of the two beams is done by creating a plasma in air with one beam and optically probing it with the other beam. A plasma is created with one beam (from here on: proton beam) at low energy and imaged by the focus diagnostic of the other beam (from here on: interaction beam). By varying the delay between the two pulses, the evolution of the plasma created in air can be observed. Similar to the temporal synchronisation with a glass slab

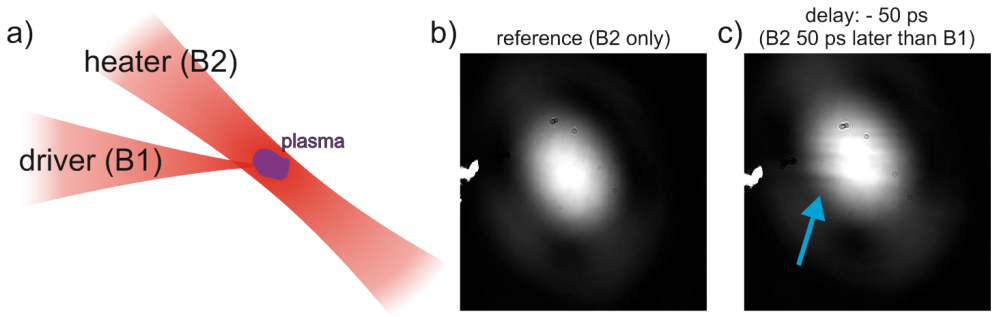

Figure 5.2: a) Schematic illustration of the temporal synchronisation of the two pulses in air. A plasma is generated with one of the two high-intensity pulses by focusing with low energy in air. The second high intensity pulse is employed as an imaging beam. By varying the delay between the two pulses, a plasma in air at different stages of expansion can be imaged. The delay is varied until both pulses reach the interaction point at the same time. Images b) and c) show probing images at different probing times. The reference image in b) shows the imaging beam without the second beam (and thus no interaction is observed). In c), the probing beam is reaching the interaction point 50 ps later than the interaction beam and a plasma can be observed which is indicated by a blue arrow.

as presented in chapter 4, the delay between the two pulses can be adjusted via a double-pass delay stage in the beamline of the interaction beam, which can be varied in µm steps. Images b) and c) in figure 5.2 show the interaction at different probing times. In figure 5.2 b) a reference image without the interaction beam (B1) is shown. If the probing beam reaches the interaction point later than the interaction beam, a plasma/some filament can be observed as shown in figure 5.2 c). Here, the probing beam is 50 ps later than the interaction beam. A blue arrow indicates the observed filaments. The delay is varied until the plasma generated in air is no longer visible in the imaging line of the proton beam. Hence, a temporal synchronisation in picosecond range is obtained.

5.2 Electromagnetic pulse generation and its characteristics

5.2.1 Generation mechanisms

Before demonstrating the experimental data, an overview of the generation mechanisms of the electromagnetic pulse will be given. For this section mainly the

references [140] [141] [142] [143] are used.
The electromagnetic pulse generated during the interaction between a laser pulse and solid target contains two different spectral components. One is due to the ejection of fast electrons from the target and the second one is due to the neutralisation current flow [140] [141] [142] [143]. Different parameters such as the hot electron temperature, laser heating, hot electron collisional cooling and the hot electron ejection govern the electromagnetic pulse's amplitude shape and temporal profile. The interaction between an intense laser pulse and a solid target leads to electron acceleration and heating. While some of these hot electrons are ejected from the target, others dissipate their energy inside the target [143]. A fraction of the electrons is travelling to a distance of the order of their Debye length. They are ejected out of the target front surface, leaving a sheath potential. Additionally to the sheath potential, another potential which is due to the net positive charge on the target surface, is contributing to the potential barrier. Only the high energetic electrons can escape this barrier and constitute an electric current which is charging the target positively [143].
A simplified energy distribution can be described by a Maxwell-Juttner distribution function [143]:

$$f_h(E_e, T_h) = \frac{\gamma p}{\curlywedge} exp(-E_e/k_B T_h), \tag{5.2.1}$$

where γ is the relativistic factor, p the electron momentum, and $\curlywedge$ a normalisation factor. Electrons with an energy greater than the potential barrier ($E_e \geq e \triangle \phi$) can escape the target.

5.2.2 Hot electron temperature

In the high-intensity regime, the escaping hot electrons are the energy carriers in the collisionless absorption mechanism. Since the temperature of these hot electrons strongly depends on the absorption mechanism, a scaling law for the temperature using the absorption models can be derived. Depending on the laser pulse intensity, duration and contrast, various mechanisms become dominant. Thus different mechanisms contribute to the scaling laws.
Different approaches were made in order to estimate the hot electron temperature. In [36], a short summary of different hot electron temperature measurements in femtosecond laser-solid experiments is presented. Figure 5.3 summarises the experimentally measured temperatures in comparison with various models such as: [72], [49] and [44]. Generally, a dependence of the hot electron temperature on the

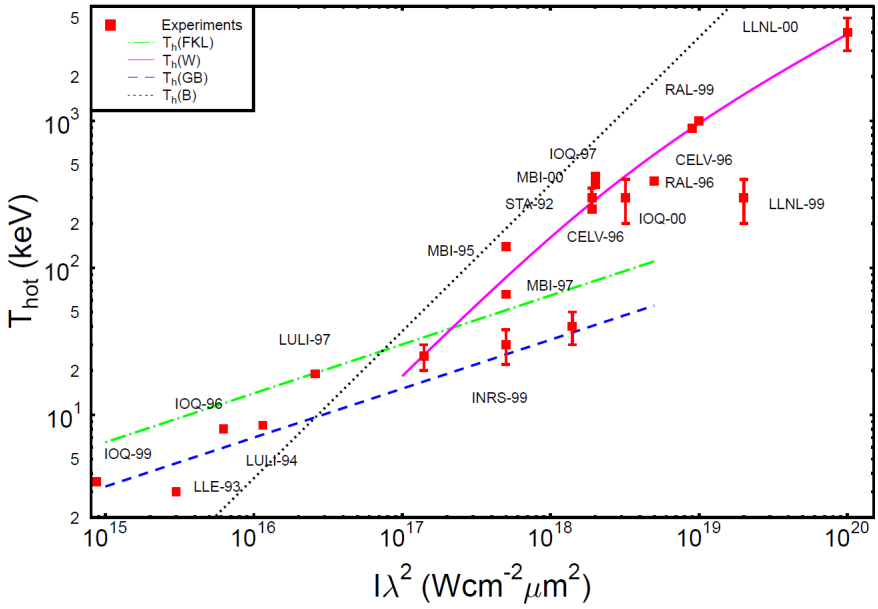

Figure 5.3: Hot electron temperature for sub-picossecond laser-solid interactions as a function of irradiance. Here, a comparison between different models is presented. A detailed description of the scaling laws and experimental conditions is given in [36].

product of $I\lambda^2$ is predicted in all models. For intensities exceeding 10^{18} W/cm^2, the relativistic regime is reached. As in stated [21], the scaling for the hot electrons is not given by resonance absorption but by the ponderomotive potential, which leads to a relativistic Maxwellian distribution. The effective hot electron temperature is thus found to be:

$$T_{hot} \cong mc^2 \left(1 + \frac{2U_P}{mc^2}\right)^{1/2} . \tag{5.2.2}$$

As can be seen, the hot electron temperature is scaling with the ponderomotive potential U_P[eV] $= 9.33 \times 10^{-14}$ I [W/cm^2] λ^2 [µm^2]. For the parameters in the experiments presented here in this chapter (I $= 2 \times 10^{20}$ W/cm^2, $\lambda = 800$ nm $= 0.8$ µm) the hot electron temperature is found to be $T_{hot} \cong 3.53$ MeV. Other models for the prediction of the hot electron temperature, e.g. by Haines et al. [144], are based on a fully relativistic approach which principally is more appropriate for interactions in the high intensity regime. The scaling by Haines et al. provides a slightly lower electron temperature than the ponderomotive scaling given by Wilks et al. However, both estimations yield electron temperatures of a few MeV Nevertheless, in general the scaling by Wilks et al. is more established in the experimental interpretation. Therefore, the scaling by Wilks with an exponential electron spectrum is chosen. Moreover, as will be discussed later, a more thorough approach for modelling the

hot electron spectrum is used in the analytical model included in the ChoCoLaT II code, considering appropriate scaling models for different intensity ranges and relativistic effects at high intensities. Since the analytical model is in agreement with the simulations no significant variations using the Haines model are expected.

5.2.3 Hot electron dynamics

During the interaction of a high-intensity laser pulse with solid targets, a large quantity of hot electrons is generated. Some of these hot electrons can escape the target and leave behind a significant positive charge resulting in a strong electromagnetic pulse. Three main effects modify the dynamics of the hot electrons: laser heating, hot electron collisional cooling and hot electron ejection. These three different effects modify the total energy of the hot electron cloud which is given by the product of the cloud temperature and the number of electrons [143]. These effects will be briefly described in the following.

Laser heating

The hot electrons generated by laser heating follow a Maxwell-Juttner distribution at a temperature T_0. Assuming a linear hot electron production within the pulse duration, the total number of hot electrons is defined by the ratio between the laser energy and the initial hot electron energy [143]:

$$N_{tot} = \frac{\eta_L E_L}{\langle E_e \rangle_0}. \tag{5.2.3}$$

The hot electron production rate can be estimated by $\partial_t N_h = \frac{N_{tot}}{\tau_L}$, which is valid for $t < \tau_L$. N_h notes the electron number and τ_L the laser pulse duration.
During the pulse duration (injection period), the hot electron average energy and temperature are constant following the energy conversation.

Hot electron collisional cooling

The hot electrons transfer their energy to the bulk electrons via collisional processes. The collision time can be calculated by the ratio between the electron diffusion length and the thermal speed and is averaged over the electron energy distribution. First, assuming a constant temperature, the number of hot electrons is reduced due to collisions with cold electrons. Some electrons disappear even before the laser is completely gone for $t_{mff} \ll \tau_L$, where t_{mff} is the mean free flight time (scattering radius divided by the averaged hot electron speed). The reduction of number of

electrons results in a loss term [143]:

$$\partial_t N_{tot} = -\frac{N_h}{t_{life}}, \tag{5.2.4}$$

where t_{life} indicates the mean free flight time plus a cooling time [1]. The loss term is valid for $t < \tau_L$.
Furthermore, the hot electron temperature is reduced linearly due to collisions. The temperature of the electrons is then defined as:

$$\partial_t T_h = -T_h / t_{mff}, \tag{5.2.5}$$

which is valid for $t > \tau_L + t_{mff}$. For $t > \tau_L$ the mean energy of the electrons is reduced instead of the number of electrons as in the case for $t < \tau_L$.

Hot electron ejection

Hot electrons with an average energy higher than the potential barrier can escape the electron cloud. The flux of the escaping electrons is defined by the current [143]:

$$J_h = e\Omega_\beta n_{hot} \pi R_h^2 \int_{|w\triangle\phi|}^{\infty} f_h v d\epsilon, \tag{5.2.6}$$

where $\Omega_\beta = (1 - cos\beta)/2$ is the solid angle of the ejected electrons and R_h the radius of the hot electron cloud.
The ejection of energetic electrons reduces the number of hot electrons in the hot electron cloud, which can be described by the ejection current:

$$\partial_t N_h = -J_h / e. \tag{5.2.7}$$

The temperature of the hot electrons is proportional to their average energy $T_h \propto \langle E_e \rangle$. The reduction of the energy of the hot electron cloud is given by:

$$\partial_t E_h = -J_h \frac{\langle E \rangle_{hot}}{e}, \tag{5.2.8}$$

which leads to the energy reduction of the hot electrons:

$$\partial_t \langle E_e \rangle = -\frac{\langle E_e \rangle J_h}{N_h e} \left(1 - \frac{\langle E_e \rangle_{hot}}{\langle E_e \rangle} \right). \tag{5.2.9}$$

[1] t_{life} is the time interval in which the temperature decreases from T_0 to 0.01 T_0 (i.e. $t_{cool} = \int_{0.01T_0}^{T_0} \frac{t_{mff}}{t} dx$)

The hot electron ejection is limited by the number of hot electrons which have an energy high enough to escape the barrier.
On the one hand, the ejection current cannot be higher than the ejectable electrons and on the other hand, there is a maximum number of ejectable electrons.
Summarising, the dynamics of the hot electrons generated during the interaction of a high-intensity laser pulse and a solid target are affecting the target charging and therefore the electromagnetic pulse. The charge is accumulated, since the hot electrons heated in the laser plasma are leaving the target. This ejection time is defined by the hot electron cooling time, which is mainly due to collisions with the electrons and ions in the target. Therefore, it can be deduced that the accumulated charge depends on the target material and it is decreasing with increasing target density.

5.2.4 Experimental raw data

Now, having a general overview of the generation processes of the electromagnetic pulse and its characteristics, the experimentally obtained data is presented and described. Figure 5.4 shows a selection of raw data obtained in one single shot. The state of the folded wire is described by the different layers of the RCF stack. On each RCF layer, the propagation of the electromagnetic pulse along different segments of the folded wire at different probing times can be seen. The colouring level on the RCFs is proportional to the incident proton flux. A general formula for the relative probing time of a proton with given initial energy crossing the wire and arriving on the RCF stack may be expressed by:

$$t_{rel}(E_p) = t_a(E_p) - t_0, \tag{5.2.10}$$

where $t_a = \ell\,(m_p/2E_p)^{1/2}$ with ℓ the distance between the proton target and the interaction point, t_0 the delay between the interaction and probing pulse an E_p the proton energy.
Figure 5.4 b) shows for example that the wire in segment number 2 appears positively charged, while the consecutive segment remains electrically neutral. The conical shape of the charge (proton deflected region) is highlighted by red dashed lines. The electric field is rising as the positive charge is flowing towards the ground. The charge starts to rise from the side where the interaction target is connected. Regarding later probing times (in the same shot) (cf. figure 5.4 c)), the width of the proton depleted region in segment number 3 is increased. This is an

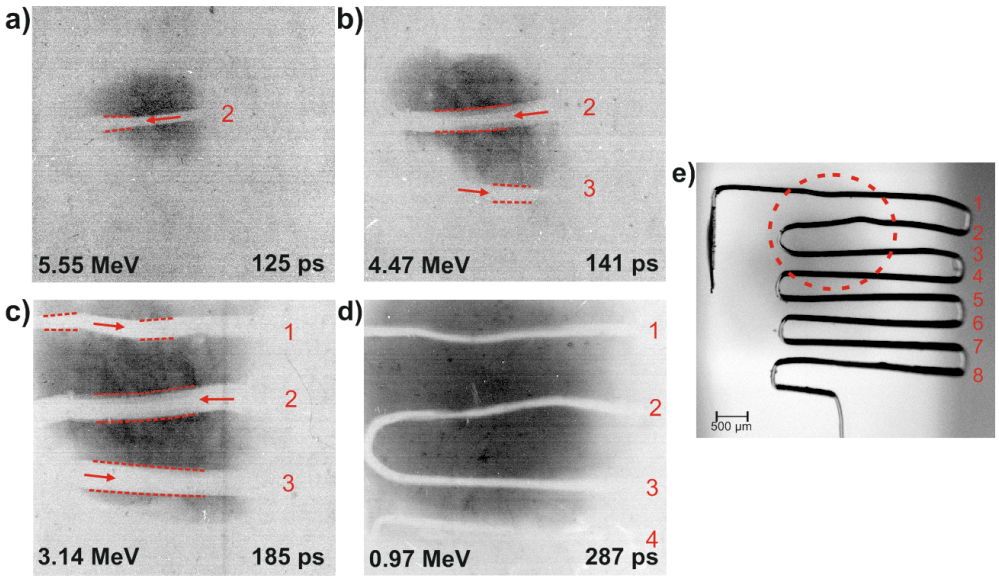

Figure 5.4: Exemplary probing images of the electromagnetic pulse flowing along the SWP at different probing times (a)-d)). These raw images were obtained in a single shot. Each image corresponds to one RCF layer in the stack detector, and to one proton energy accordingly (cf. labelling in the bottom left corner of each image). The probing time in the bottom right corner corresponds to the arrival time of the protons of respective energy given by the time of flight of different energy protons passing through the interaction region. The arrows indicate the direction of the charge flow and the dashed lines provide a guideline for the eye in order to identify the width of the proton depleted regions. Image e) shows a reference image of the SWP target with a dashed red circle representing the field of view of the probing proton beam. The length of each horizontal wire segment in the SWP is ~ 5 mm and the vertical spacing between each segment is $\lesssim 500$ µm.

evidence that this segment has become charged by some positive potential. The charge has moved from segment number 2 to segment number 3 within the time difference between the two RCF layers. Apparently as can be seen in figure 5.4 c), the wire in segment number 1 is going back to be electrically neutral as the shape of the proton deflected region takes a conical form being narrower towards the laser irradiated target side. Previous observations [132] [145] confirmed a surface electromagnetic pulse generation and propagation. The positive charge is carried towards the ground, lowering the target potential towards neutrality. The velocity at which the charge moves along the wire has been measured to be approximately close to the speed of light [132].

The proton signal deposited in the first layer is associated with late probing times,

being generated by lower-energy protons.
Probing an electrically neutral metal wire, the shadow of the wire would be visible. This shadow is a proton depleted region due to multiple small angle scatterings of the probing protons in the wire. For a positively charged wire, the protons will experience a strong Coulomb deflection. The extent of the depleted region observed on the RCF is dependent on the strength of the electric field generated around the wire and the energy of the probe protons. The probe protons experience an electrostatic force as they encounter a charged region and are deflected away. The protons are accumulated around the electrical field region which leads to a depletion at the electrically active region. The RCFs show an evidence for the presence of an outwards-pointing radial electric field decaying with distance from the wire surface. Protons farther from the target experience a weaker deflection due to the field distribution. The deflecting fields are travelling along the wire towards the ground. This is why the proton deflections are visible across the entire field of view, but not all segments of the wire have the same deflection.
A qualitative description of the characteristics of the electromagnetic pulse will be presented in the following section.

5.2.5 Characterisation of dynamic wire charging

The observed transient charging of the wire shown in figure 5.4 is quantified by using the particle tracer PTRACE (cf. section 3.6). The spatial nature and temporal evolution of the quasi-static fields is inferred by finding a best match between the experimentally measured proton density (n_p) an the particle tracer simulation. A metallic wire with a constant linear charge density is probed by monoenergetic protons. The energy of the protons and the distance between the proton source and the wire are set according to the experimental set-up. For each RCF layer, the value of the linear charge density $\lambda_c(t)$ is varied repeatedly until a best-match between the experimentally measured and simulated proton density behaviour is attained. In figure 5.5, an illustrative example of the best-match obtained for the RCF layer corresponding to a probing time of 185 ps is presented. A comparison between the experimentally measured and particle tracer simulation output of the proton density n_p modulation across the wire is performed. The best-match between the experiment and simulation is achieved by varying the value for the linear charge density until the deflection matches the experimentally measured value. Following this procedure, the linear charge density can be obtained for each segment and RCF layer. A temporal picture of the rise and decay of the electrical field can

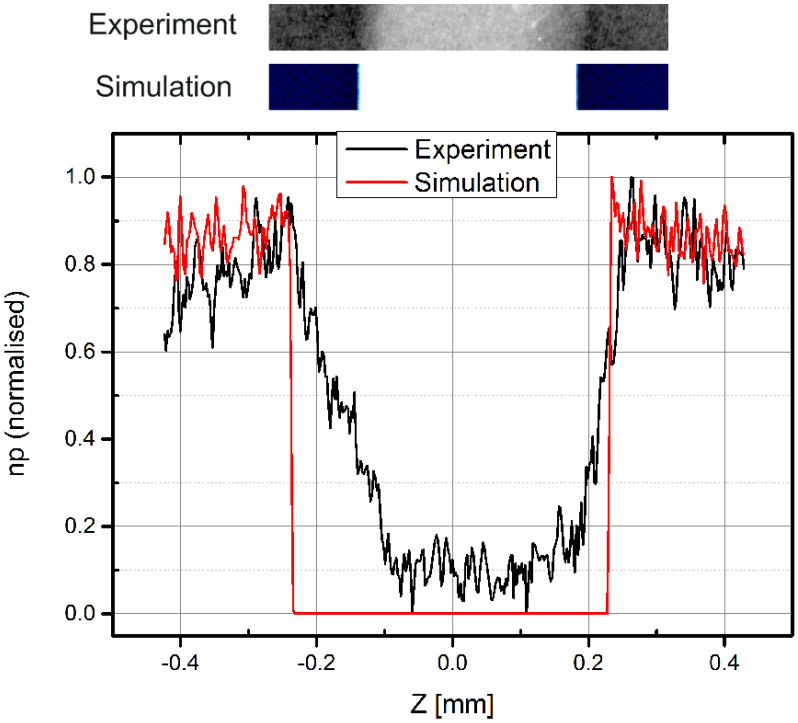

Figure 5.5: Comparison between experimentally measured and particle tracer simulation output of the proton density modulation across the wire. A line out shows the best match between simulation and experiment. Since in the simulations monoenergetic protons are used ($E_p = 3.14$ MeV), the profiles look a bit different. The profile obtained from the experimentally measured deflection is not uniform due to the multi-energy and non-uniform proton beam flux. The value for the linear charge density was varied until a best match between the experiment and simulation was achieved. In this case, the linear charge density was set to 4.74 µC/m.

be determined. Since the multi-energy proton beam flux in the experiments is non-uniform, the density modulation across the wire differs from the simulated line-out. In the simulations, monoenergetic protons are used, which in this case correspond to an energy of $E_p = 3.14$ MeV.

Temporal profile of the electromagnetic pulse

Quantitative information about the temporal profile of the electromagnetic pulse can be obtained from the raw data shown in figure 5.4 by following the charging and discharging of the wire in the square wave pattern in different RCF layers. The proton energies (E_p) on each RCF layer are calculated with SRIM and refer to protons reaching their Bragg peak in each RCF layer. The probing times correspond to the time of arrival of the proton with the energy at their Bragg peak at the centre of its field of view (cf. section 3.5). Due to the divergence of the probing proton beam, the probing time of each proton varies within a few ps on the SWP. The absolute probing time at a given point P(x,y,z) can by calculated by

$$t_{proton}(E_p, x, y, z) \simeq \sqrt{\frac{x^2 + y^2 + z^2}{2E_p/m_p}}. \tag{5.2.11}$$

As estimated in [134], the velocity of the electromagnetic pulse along the wire is found to be $v_{charge} = 0.96c$. Now assuming the electromagnetic pulse is travelling with constant velocity, the arrival time of the electromagnetic pulse at the point P(x,y,z) can be written as $t_{charge} = \ell_{charge}/v_{charge}$, where ℓ_{charge} is the distance of the wire between the probing point and the proton source. For each analysed point on the SWP, the travelling distance of the charge (ℓ_{charge}) is measured directly from the reference image of the target. The reference images are taken prior to each shot as can be seen in figure 5.4 e).

Accordingly, the electromagnetic pulse profile can be obtained by measuring the linear charge density at different points on the wire and plotting the linear charge density with respect to the relative probing time. The relative probing time is given by $t = t_{proton} - t_{charge}$. Therefore, the linear charge density at different probing times needs to be determined by particle tracing simulations using PTRACE. In that way, the temporal profile of the electromagnetic pulse can be reconstructed as shown in figure 5.6. Although having a number of limited snapshots of the charge, the shape of the electromagnetic pulse can be defined broadly as having a full width at half maximum of ∼25 ps which is consistent with previous measurements [100] [132] [134] [135].

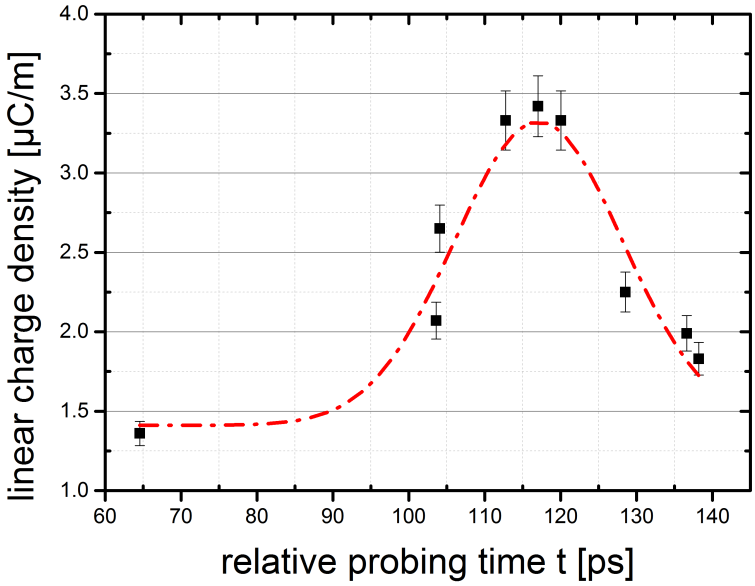

Figure 5.6: Temporal profile of the electromagnetic pulse travelling along a thin aluminium wire. The linear charge density is plotted against the relative probing time t = $t_{charge} - t_{proton}$. Here, t_{charge} is the arrival time of the peak of the electromagnetic pulse at a given point on the wire and t_{proton} the probing time of the protons at that given point. The red dashed curve is a Gaussian fit and a guideline for the eye.

Electrical field growth and decay

Using the linear charge density presented in figure 5.6, the electrical field strength can be determined. The electrical field strength within the wire can be quantified by assuming a cylindrical geometry. Applying Gauss's law now and using the amount of free charge per unit length $\lambda_c(t)$ determined via PTRACE, the electrical field strength may be calculated by

$$E_s(t) = \frac{\lambda_c(t)}{2\pi\epsilon_0 r_w} \propto \frac{1}{r_w}, \tag{5.2.12}$$

with r_w the wire radius. The value of $\lambda_c(t)$ is varied repeatedly in the particle tracer until a best match between experimentally measured and the simulation is achieved (cf. above).

In figure 5.7 a graph detailing the highly-transient electrical field growth and decay as inferred from particle tracing simulations is presented. Over a temporal window of $\sim$ 40 ps the electrical field is present in the wire surface is rising to its peak magnitude of 1.2 GV/m and decaying subsequently below a measurable level. Note

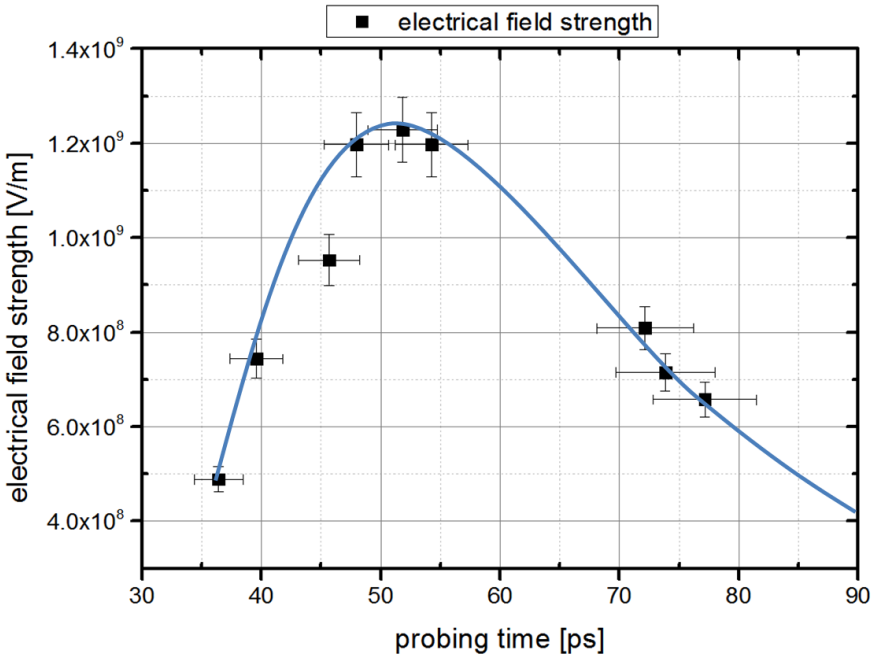

Figure 5.7: Electrical field growth and decay. The graphs presents the electrical field strength for varying probing times. The blue line provides a guide for the eye.

that following Gauss's law, the free charge is most likely to be concentrated within a very shallow skin layer close to the wire-vacuum interface. If $\rho_{Al} = 2.82 \times 10^{-8}\Omega$m [146] is the resistivity of Aluminium in vacuum, μ_0 the permeability of free space and dt the duration of charge-discharge cycle, the skin depth can be estimated to be:

$$\delta \simeq \sqrt{\frac{2\rho_{Al}dt}{\pi\mu_0}} \simeq 0.535\mu\text{m}. \tag{5.2.13}$$

Hence the free charge and the related current are localised within a very small skin layer at the wire surface. The electric and magnetic field will be zero in the bulk of the wire. For $r > r_w$, where $r = \sqrt{x^2 + y^2}$ is the radial distance from the wire, the electrical field strength is decaying as $\frac{1}{r}$ as shown in equation 5.2.5.

5.3 Parametric study for optimising the electromagnetic pulse

As discussed in other studies before, analytical models indicate an optimum pulse duration at a pulse duration of few hundreds of fs [133] [134]. Furthermore, the electromagnetic pulse is strongly dependent on the laser energy and laser pulse

duration. In order to study these dependencies, a detailed parametric study is performed. These studies should also set up a benchmark for the scaling of the acceleration efficiency at short pulse multipetawatt laser facilities which will be available for experiments in the near future at ELI and APOLLON facilities [137] [138]. The experiments are concentrating on the effect of the laser pulse duration and laser energy on the electromagnetic pulse. The pulse duration is varied up to 200 fs and the laser energy onto the target up to 400 mJ (in FWHM of focus spot). In the following, the experimental and analytical findings are going to be presented.

5.3.1 Effect of laser pulse duration

The effect of the laser pulse duration on the peak charge density of the electromagnetic pulse for two different laser energies is shown in figure 5.8. In order to

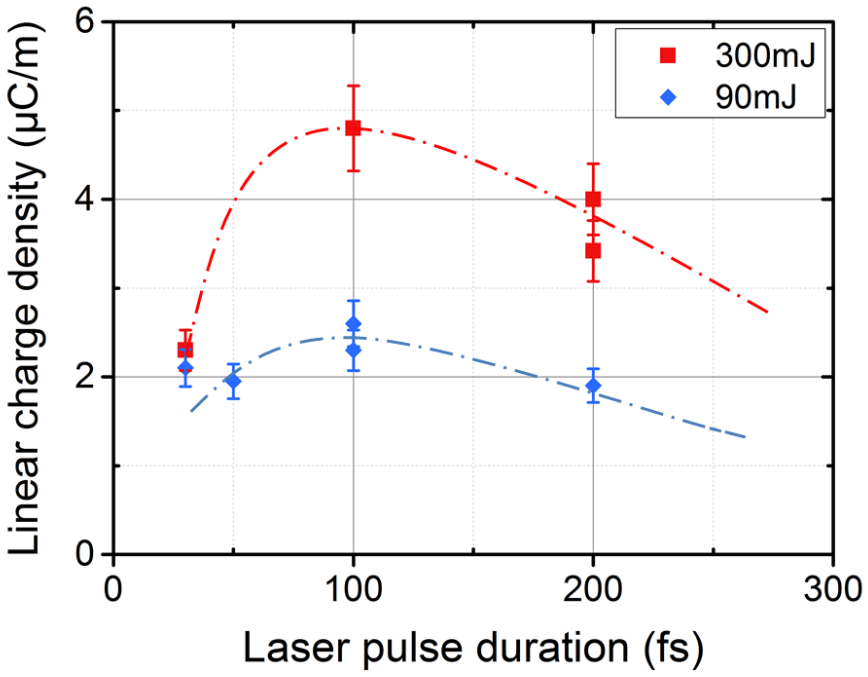

Figure 5.8: Dependence of the laser pulse duration on the linear charged density at a fixed energy (cf. [139]). The dependence is shown for two different energies on the target: 300 mJ (red squares) and 90 mJ (blue diamonds). The dashed lines provide a guidance for the eye.

achieve different pulse durations, the compressor gratings of the interactions beam are moved slightly (cf. section 3.1). For measuring the laser pulse duration a Spider module from *Amplitude Technologies* was used. However, the Spider module cannot measure pulse durations above 100 fs. For that reason, the laser pulse duration of

30 fs was set to zero and the gratings were moved (in μm precision) accordingly for the other investigated pulse durations. Two measurements for two different laser energies, 300 mJ (red squares) and 90 mJ (blue circles) (onto the target) are performed to investigate the effect of the pulse duration at different energies.
For a laser energy of 300 mJ on the target, the maximum linear peak charge density of roughly 5 μC/m is found at 100 fs. Decreasing the laser energy to 90 mJ, the linear charge density is also decreasing to roughly 2.4 μC/m. In this case, the maximum linear charge density is not as obvious as in the 300 mJ case. However, as the guidance indicates, a slight peak is visible again at 100 fs. It is in good agreement with the predicted scaling [133].
The electron spectrum can be assumed to be a simple exponential function $dN/dE = (N_0/U_p)\, exp\,(E/U_p)$, with $U_p = k_B T_e$ the ponderomotive potential of the incident laser pulse, k_B Boltzman's constant and T_e the hot electron temperature. N_0 is given by $N_0 = \eta \times E_L/k_B T_e$, assuming an exponential spectrum, where η is the laser to electron conversion efficiency and E_L the laser energy on the target.
For lower intensity interactions a much lower U_p and higher N_0 is obtained. For an infinite target this would mean a much higher number of escaping electrons. However, for a target of finite size, a saturation of charging is reached depending on the self-capacitance of the target C_{tar}. By calculating the potential barrier for the maximum charge the saturation of the charging can be verified. The number of escaping electrons can be mathematically written as:

$$N_{esc} = (\eta E_L/U_P) exp(-e\phi/U_P), \tag{5.3.1}$$

where ϕ can be obtained from the energy balance equation

$$eN_{esc}/C_{tar} = \phi, \tag{5.3.2}$$

with $eN_{esc} = Q = \int_{-\infty}^{\infty} \lambda dl$ where λ is the linear charge density per unit length. The potential barrier is found to be

$$\phi = \frac{Q}{8\epsilon_0 r_{tar}}, \tag{5.3.3}$$

where ϵ_0 is the permittivity of free space and r_{tar} the radius of the target.
The effect of the laser pulse duration on the linear charge density can be understood analytically and will be discussed in the following.
Decreasing the intensity at a given energy (for instance by increasing the pulse

duration), the total number of hot electrons (N_0) generated during the interaction is enhanced with a lower average energy. As a consequence, the net escaping charge Q and the target potential ϕ are increasing. However, at low intensities, the electron energy is less than the target potential and the net escaping charge reduces, since fewer hot electrons overcome the potential barrier. For a given laser energy and varying intensities, equation 5.3.1 provides that a maximum number of escaping electrons is reached for $e\phi = U_P$, which in turn yields the condition for a maximum hot electron escape

$$U_P[MeV] = \sqrt{0.37\eta e_L / C_{tar}[\mathrm{pF}]}. \tag{5.3.4}$$

Assuming that approximately 30% of the laser energy is transferred into hot electrons [147] [148], the maximum temperature for a laser energy of 300 mJ is found to be roughly $\sim$ 700 keV, which corresponds to a laser pulse duration of $\sim$ 150 fs. Regarding these estimated calculations, the experimentally obtained numbers in figure 5.8 are in broad agreement.

5.3.2 Effect of laser energy at fixed pulse duration

Due to the escape of hot electrons, the target potential is temporally evolving, which leads to a dynamic process of the electrical charging of the target during the interaction. In principle, the collisional cooling of the hot electrons inside the target can lead to a considerable loss of the electrons mean energy over several picoseconds of the charging period.
Assuming 27 nC for the maximum charge and the foil target radius of $r_{tar} = 1.15$ mm, which can be calculated by assuming a circular disk equivalent to a square-shaped target of 2.3×2.3 mm^2 as was used in the experiment, the potential barrier discussed in equation 5.3.1 is found to be 0.339 MeV. For various laser energies studied in the experiments, the potential barrier is given in figure 5.9. The experiments are carried out for three different laser pulse durations: 30 fs, 100 fs and 200 fs. With increasing laser energy, the potential barrier is also increasing linearly. The potential barrier is highest for a laser pulse duration of 100 fs and is also increasing the fastest comparing to the other investigated pulse laser durations. The potential barrier is significantly smaller than the hot electron temperature estimated above. It is found to be a few mega-electron-volt by using the ponderomotive scaling. Therefore, it is plausible to assume that the target size does not affect the electron escape.

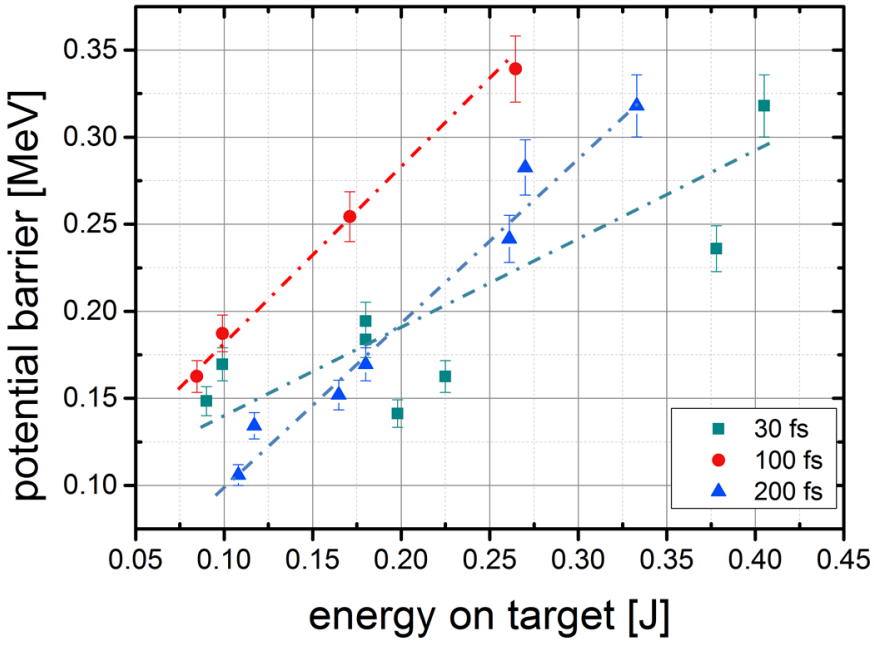

Figure 5.9: Potential barrier for various laser energies investigated in the experiment. The amount of charge (or the linear charge density, respectively) was obtained using PTRACE. Three different pulse durations are presented, where the cyan square stands for 30 fs, the red circle for 100 fs and the blue triangle for 200 fs, respectively. The dashed lines are a guidance for the eye.

As stated in [143] for long pulse durations ($\gtrsim ps$) the collisional electron cooling can lead to a significant loss in the electron's mean energy. The duration of the charging process depends, as discussed above, on the lateral target size and the cooling time of the hot electrons [133], the net charge escape from a 2 mm wire is modelled using the ChoCoLaT code [143]. The target charging at different laser pulse durations was modelled predicting an optimum pulse duration to be between 100 - 200 fs for a typical target size of a few mm. In the picosecond regime it can be seen that the charge is reducing sharply. The duration of the electromagnetic pulse is found to be roughly 25 ps ($FWHM$) for laser pulse durations between 30 and 600 ps. Two independent experiments carried out at the Arcturus (30 fs) and Taranis (600 fs) laser facilities confirmed that the electromagnetic pulse duration does not depend on the laser pulse duration [133].
Since the potential calculated above is significantly smaller than the hot electron temperature estimated by the ponderomotive scaling to be a few mega-electron-volt it is reasonable to assume that the target size does not affect the electron escape. Consequently, for a sufficiently high electron temperature such that $e\phi < U_P$, an

increasing laser energy would lead to an enhanced charged accumulation at a fixed pulse duration. Equation 5.3.1 can be expressed as

$$N_{esc}(E_L) \sim k_1\sqrt{E_L(1 - k_2\phi\sqrt{E_L})} \tag{5.3.5}$$

by assuming a typical $I^{1/2}$ scaling for the hot electron temperature [59]. In this case, k_1 and k_2 are constants. This assumption implies that the target potential scales with $\sqrt{E_L}$ and consequently the charge also scales with $\sqrt{E_L}$, which is in agreement with the experimentally obtained data.

Keeping the pulse duration fixed, the effect of the laser energy on the linear charge density can be determined. Figure 5.10 shows the linear charge density as a function of the laser energy on the target. Consequently, the collisional cooling makes a significant contribution for long pulse durations ($\geq ps$), as suggested in the theoretical models in [143] and [149]. Using the numbers for the stopping range of electrons with an energy of 3.5 MeV obtained via ESTAR [150], the maximum range is calculated to be 1.15 mm. A cooling time of $\sim$ 0.5 ps can be found for these parameters which is significantly larger than the pulse durations discussed here. Consequently, it is reasonable to neglect the electron cooling. The linear density is determined for three different pulse durations, namely 30 fs, 100 fs and 200 fs. The green diamonds stand for 30 fs, the red squares for 100 fs and the green triangles for 200 fs laser pulse duration. A linear dependency for all three pulse durations is observed for the time scales and laser energies observed in the experiments. Keeping the pulse duration fixed and increasing the laser intensity (laser energy on the target), the linear charge density is increasing linearly. The increase of the linear charge density (or total charge if integrated over the pulse length) is mainly due to the enhancement of the hot electron population. However, considering a larger range of energies, a more generic trend for the dependency can be obtained. For instance, figure 5.11 shows the dependence of the total charge on the laser energy. The total charge used here in this graph is obtained by simulations using the ChoCoLaT II code which will be discussed in more detail in the following section. Figure 5.11 depicts the dependence of the total charge which follows a power law scaling, i.e. $Q \sim E_L^{0.65}$ with almost the square root of the laser energy (as discussed above) as expected for a dynamically evolving target potential. For the energy range regarded in the experiments in this thesis a linear dependence can be assumed, as can be concluded from the graph in figure 5.11.

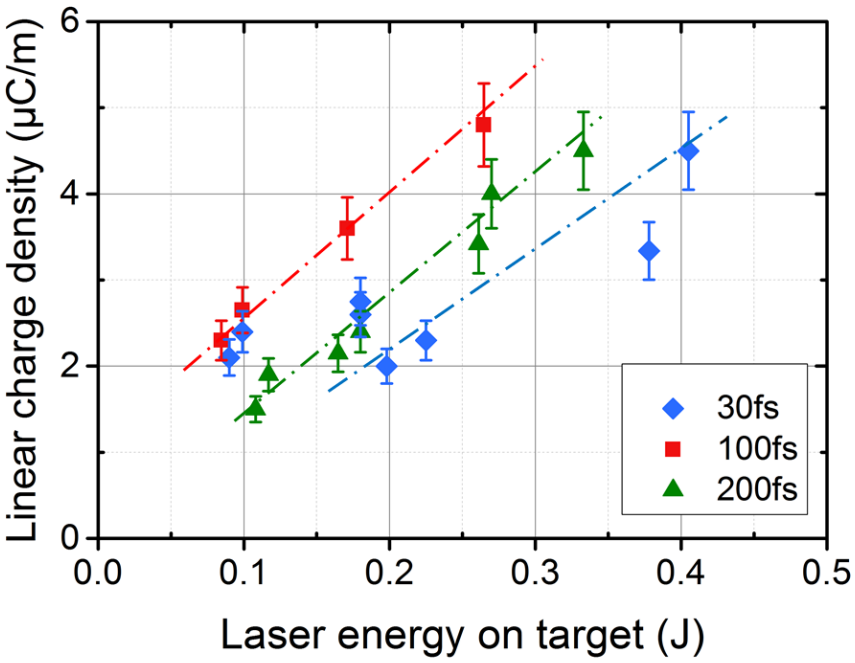

Figure 5.10: Dependence of the laser energy on the linear charge density at a fixed laser pulse duration (cf. [139]). Three different pulse durations are demonstrated: 30 fs (blue diamonds), 100 fs (red squares) and 200 fs (green triangles). A linear trend is observed for all three pulse durations. The dashed lines provide a guidance for the eye.

5.3.3 Effect of laser energy at fixed intensity

In order to decouple the effect of the laser pulse duration and the laser energy, the laser energy and the pulse duration are varied to keep the resulting laser intensity fixed. In figure 5.12, the correlation of the amplitude of the electromagnetic pulse and the laser energy at a fixed intensity of 8.5×10^{18} W/cm^2 is shown. The graph in figure 5.12 shows the linear charge density plotted against the laser energy on the target. In order to keep the intensity of the laser pulse constant, the laser energy is increased for longer pulse durations. As shown in the graph, the linear charge density is increasing linearly with the laser energy on the target. However, at higher energies (300 mJ on target and pulse duration of 200 fs), the linear charge density is higher. Although the laser intensity is kept constant for all data points, the linear charge density is increasing with the laser energy. At a fixed incident laser intensity (i.e. fixed ponderomotive potential), a higher laser pulse energy leads to an increasing flux of the hot electrons. Higher flux of hot electrons consequently means a higher positive potential on the laser irradiated target.
The effect of the laser intensity on the linear charge density is shown in figure 5.12.

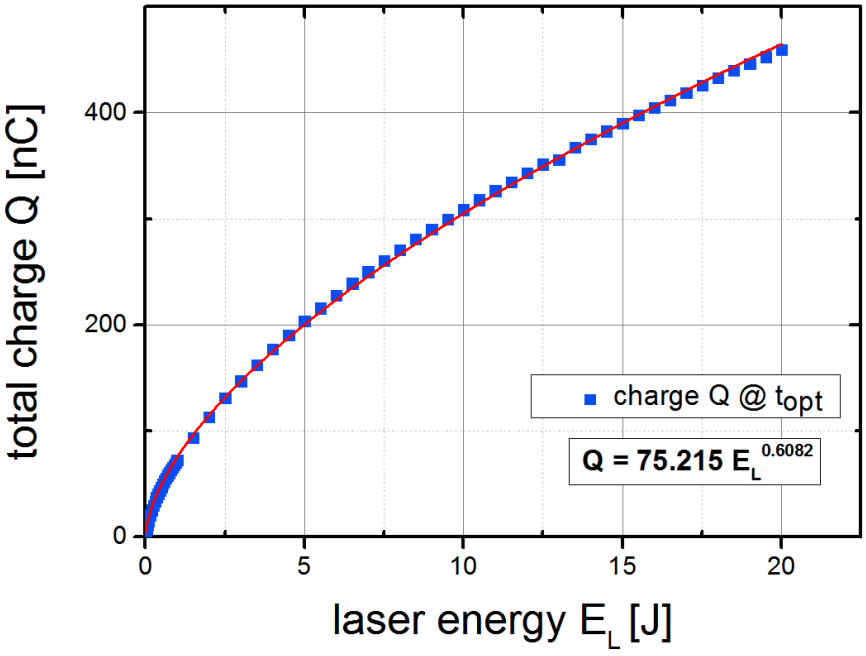

Figure 5.11: Scaling of the total charge Q of the electromagnetic pulse with a laser energy E_L. The blue data points are the total charge obtained by the ChoCoLaT II code which are shown in figure 5.14. The red line is the fit using a power law. As also shown in the graph, the total charge Q scales with $\sim E_L^{0.65}$.

The linear charge density is plotted against the laser energy on the target at three different fixed pulse durations (30 fs, 100 fs and 200 fs). By varying the laser pulse duration and laser energy at the same time, the effect of the laser intensity on the total amount of charge can be decoupled from the laser energy. As can be seen, increasing the laser intensity at a fixed pulse duration is leading to an increase in the linear charge density. Comparing the three different pulse durations, the linear charge density is increasing faster in the 30 fs case.

5.4 Analytical model

Simulations provided by A. Poyé considering the experimental parameters are presented in this chapter. The effect of the laser intensity on the total charge is studied in comparison to the experimentally obtained data. The simulations are performed by using the semi-analytical target charging model employing the ChoCoLaT II code [149]. A flowchart in figure 5.13 describes the schematic processes of the equation solver. The main purpose of the programme is to solve the equations for the evolution of a hot electron cloud during the interaction of a thin target with

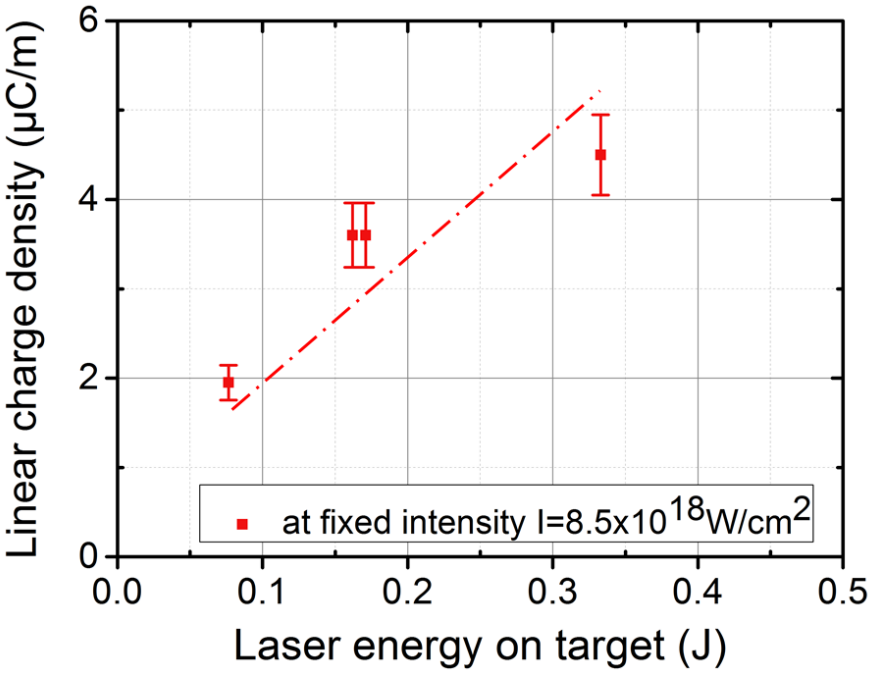

Figure 5.12: Linear charge density depending on the laser energy on the target (cf. [139]). In order to keep the laser intensity constant, the laser energy was varied according with the pulse duration. Here, the laser intensity on the target is fixed at $I = 8.5 \times 10^{18}$ W/cm^2. The dashed red line provides a guidance for the eye. At a fixed intensity, the linear charge density is increasing linearly with the laser energy on the target.

a laser and calculating the amount of ejected electrons. Therefore, three different physical phenomena are considered: hot electron collisional cooling, hot electron ejection and hot electron creation by laser (cf. section 5.2.1). The ChoCoLaT II code has a similar architecture as its previous version [143]. The temporal scheme of the solver is a simple Euler's scheme. However, in order to be conform with the physics evolution, the different contributions are split. First, static values such as the energy distribution of hot electrons in the target, the temperature or the lifetime of hot electrons are calculated before iterative calculations of the distribution function are made and averaged. Eventually, the potential and ejection currents are calculated. The calculations stop when the hot electron cloud is empty thus not affecting the charge anymore [149].

Figure 5.14 illustrates the comparison between experimentally obtained data and simulations. The simulations are carried out for three different pulse durations (30 fs, 100 fs, 200 fs) which were also investigated in the experimental studies. The total amount of charge is calculated for assuming a pulse duration of 25 ps as shown

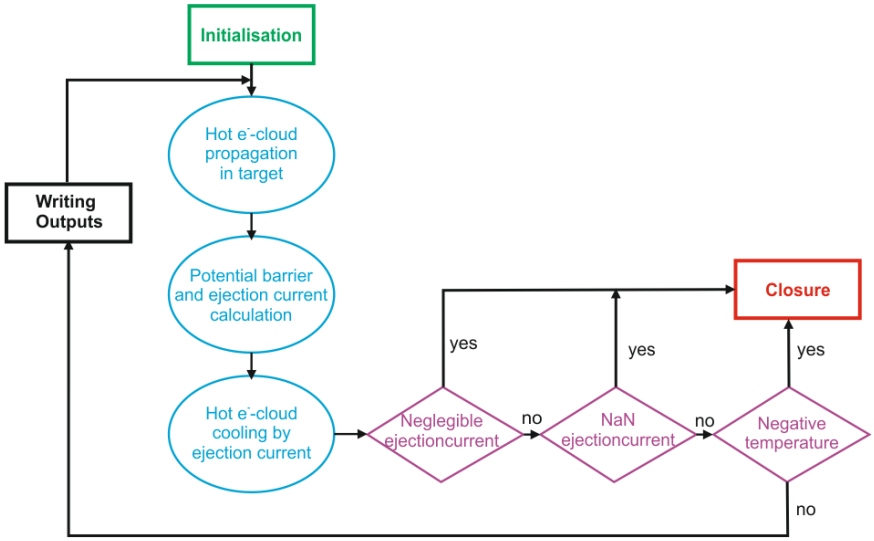

Figure 5.13: Schematic description of the processes of the equation solver of the ChoCoLaT code (cf. [143], [151]).

in figure 5.6 and also reported in [133], [136] (for picosecond and femtosceond lasers). As illustrated in the graph in figure 5.14, the estimated total charge which is recorded by performing simulations with the semi-analytical target charging model is in good agreement with the experimentally obtained data. Keeping the pulse duration constant and increasing the laser intensity on the target in the simulations, the same behaviour as seen in the experiments is obtained.
With increasing laser energy, the total amount of charge is also increasing. At a fixed laser pulse duration the linear charge density is increasing with the laser energy on the target. The total charge scales with $I^{0.54}$ similar to the phenomenological model discussed above.
Motivated by the agreement between the experiment and simulations a parametric study of the total charge for a range of laser energies and pulse durations is performed by using the ChoCoLaT II code. Figure 5.15 illustrates a parametric map of the total charge obtained using the ChoCoLaT II code. The total amount of charge contained in the electromagnetic pulse is increasing with increasing laser energy. However, for a given laser energy, an optimum pulse duration can be found. The solid black line in the map highlights the optimum laser pulse duration for different laser energies at which the charge of the electromagnetic pulse reaches its maximum. The simulations are done for a 10 µm gold target, as used in the experiments. The parameter range covered in the experiments is marked by dashed white lines. For laser energies available in upcoming facilities such as

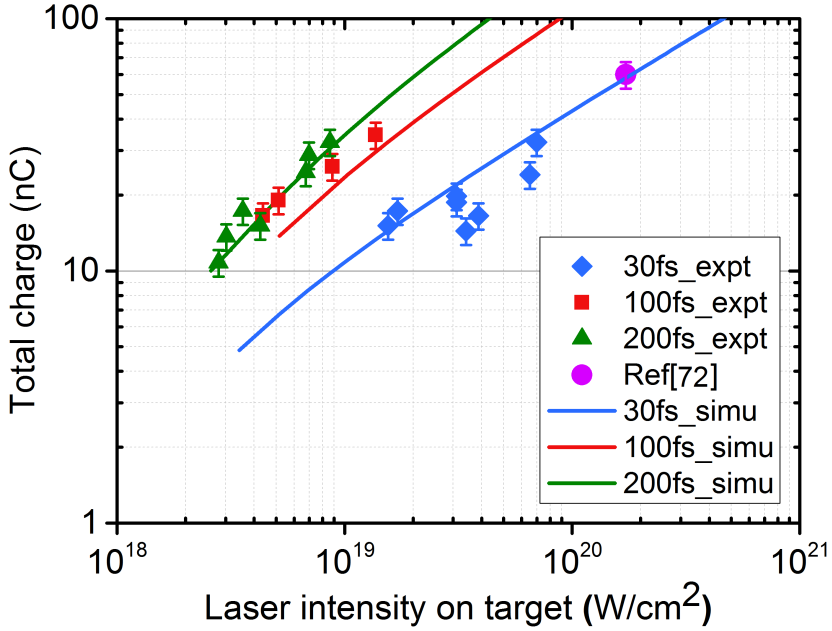

Figure 5.14: Dependence of the total charge on the laser intensity for three different laser pulse durations, viz. 200 fs (green triangle), 100 fs (red square) and 30 fs (blue diamond)(cf. [139]). The purple circle is provided by the experiments carried out in [133]. Since the experimental conditions are the same, it can be used here to show the tendency. The solid lines are obtained from the ChoCoLaT II code. The experimentally obtained total charge is in good agreement with the simulations.

ELI-Beamlines, ELI-NP and APOLLON [137] [138], optimum pulse durations of few ps are suggested by the simulations. As also discussed in [133] [134], higher laser intensities lead to a larger acceleration gradient for post-acceleration of proton beams. In order to maximise the total charge it is therefore necessary to vary the laser energy (intensity) at the optimum pulse duration.

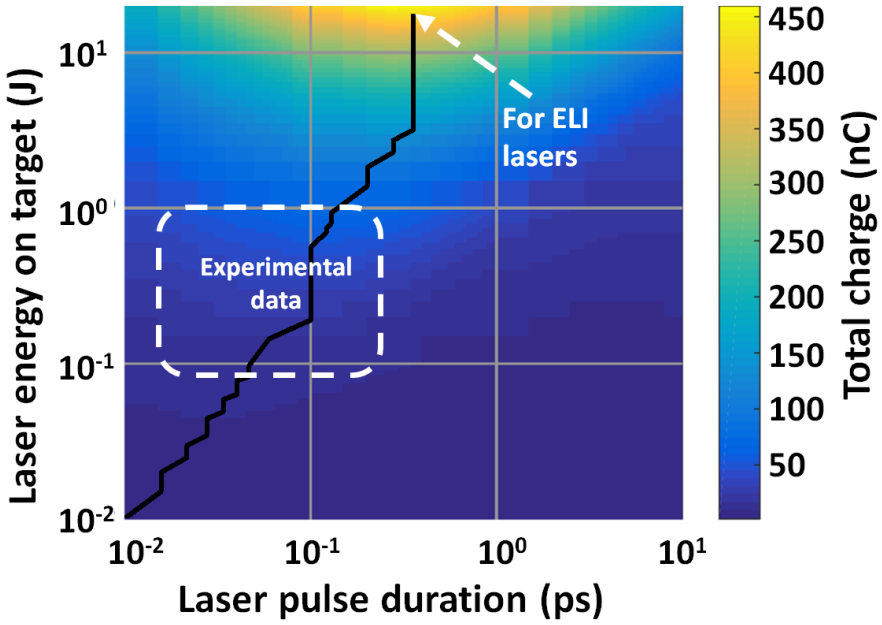

Figure 5.15: Parametric scan of the total charge for various laser energies and pulse durations obtained by using the ChoCoLaT II code (cf. [139]). The white dashed square represents the parameter range for the current and previous experiments. The solid black line marks the pulse duration needed to maximise the total charge at a given laser energy. A white arrow indicates the optimum pulse duration for ELI-class lasers. The extended range of pulse durations and laser energies require a varied step size on each axis in order to ensure a good resolution. On the time axis, for the time intervals (10 fs, 100 fs), (100 fs, 1 ps), and (1 ps, 10 ps), the simulation step sizes were 5 fs, 50 fs and 500 fs, respectively and similarly on the energy axis, the step sizes for the energy ranges (10 mJ, 100 mJ), (100 mJ, 1 J), and (1 J, 20 J) were 5 mJ, 50 mJ, and 0.5 J, respectively.

5.5 Conclusion

In this chapter, the examination of the highly transient charging of a thin aluminium wire irradiated by an ultraintense laser pulse was presented. Employing the proton probing technique, a time resolved analysis of the transient electromagnetic pulse was performed.

Furthermore, a detailed parametric study of the electromagnetic pulse was carried out. Different laser parameters including energy, pulse duration and intensity are varied in order to study the influence of these parameters on the amplitude of the electromagnetic pulse. The experiments revealed that the amplitude of the electromagnetic pulse strongly depends on the incident laser energy and pulse

duration. The amplitude of the electromagnetic pulse is increasing with the laser energy. An optimum pulse length for a given laser energy could be found. The amount of total charge associated with the travelling electromagnetic pulse was obtained with the particle tracer PTRACE. The experimental investigations demonstrated that the net charge is dependent on the laser intensity. Compared to a semi-analytical/empirical model, the experimentally obtained data is in good agreement with the data predicted by the model. Simulations using the ChoCoLaT II code confirmed the optimum laser pulse duration and maximum amount of total charge. The optimum laser pulse duration is simulated over a large range of laser parameters in order to predict and optimise the electromagnetic pulse for future laser facilities.
The dynamics of the charging of the wire are important for different applications, e.g. post-acceleration of proton beams [133] [134] [135] [136]. Investigating the dynamics of the charging process improves the understanding of the parameters significant for post-acceleration.

Contribution of the author

The results presented in this chapter are already published in [139]. All of the experimental data presented in the figures and text were recorded and analysed by the author. The text was adopted and rephrased only partially with adaptations from the manuscript mentioned above. Some figures (figs. 5.8, 5.10, 5.12, 5.14 and 5.15 (also marked in the text)) are adopted with small changes from the already published manuscript. All other figures are either referenced elsewhere or are unpublished material all elaborated by the author. As a guide for the analysis mainly references [133] [134] [135] [136] are used. The semi-analytical simulations are provided by A. Poyé.

6 Proton imaging of laser and ultra-thin foil dynamics

The acceleration of Multi-MeV protons via the interaction of short and intense laser pulses with solid targets is one of the most active research areas. In recent years, particularly the use of laser-accelerated protons as a particle probe has been increasing steadily. Due to their properties (high laminarity, low divergence, small source size [103] [102]), proton beams are most suited for detection of electric fields in laser-plasma interaction. The proton probing technique is providing a powerful tool to investigate the fast dynamics of laser-produced plasmas. Laser accelerated proton beams are employed as a charged particle probe for the detection of electric and magnetic fields generated in laser-plasma interaction. Their unique properties allow a time-resolved analysis of the fields, charge density and current distributions in the probed plasma. The high temporal resolution (in ps range) makes the proton beams favourable for the investigation of fast plasma dynamics.

In this chapter, a study of the interaction of (ultra-)thin foils and intense short laser pulses is reported. Different conditions are explored, whereby the target thickness and laser energy are varied.

The experiments are performed for two different polarisations (linear and circular) of the interaction beam. The study shows that the polarisation has a great impact on the acceleration scheme. By changing the polarisation different acceleration schemes can be achieved. While for linear polarisation the target seems to explode, for circular polarisation the whole target is pushed forward as a compressed layer (away from laser axis) by the laser pulse. For linearly polarised light, the target normal sheath acceleration (TNSA) (cf. chapter 2.5.1) is the dominating mechanism, leading to the acceleration of multi-MeV ions from the nonirradiated surface of the target [21]. Changing to circularly polarised light, electron heating is strongly suppressed due to the absence of the oscillating component of the $\vec{v} \times \vec{B}$ force. Ions are accelerated by a dense electron layer piled up in front of the laser pulse.

Moreover, the experimental results presented in this chapter confirm previous simulation studies investigating the effect of the light polarisation on the interaction between solid targets and high intensity laser pulses [28].

6.1 Experimental set-up

For the experimental investigation of the interaction between a short intense laser pulse and a(n) (ultra-)thin foil target, two independently controllable laser pulses are employed.

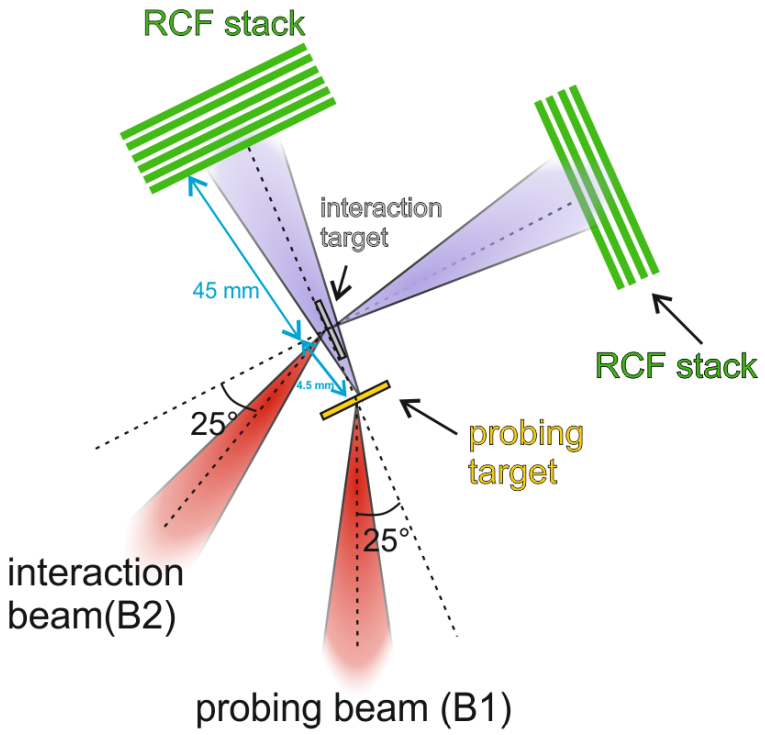

Figure 6.1: Experimental configuration for proton probing.

The experimental set-up is shown in 6.1.
In order to investigate the interaction, the proton probing technique is used (cf 3.5). The probe proton beam is generated by irradiating a foil target (*proton target*) with one of the short pulses (B2, *proton beam*). The proton target is usually a 10 µm thick gold target attached on a small aluminium post.
The interaction target is attached on a small mesh. Different target thicknesses varying between 50 and 800 nm are investigated. In order to minimise the shadow of the mesh on the interaction, the mesh is cut in half thus some parts of the target are (almost) free-standing. Eventually, the mesh is attached on a small glass needle to avoid shadowing of a big target holder. In case of a 800 nm foil, the target is directly attached on the glass needle without using a mesh.
The angle of incidence of both beams on each target is 25°. Both beams are focused by an off-axis F/2 parabola to a Gaussian focal spot of approximately 4 µm at FWHM. The intensity of the laser pulse on the interaction target is

1.5×10^{20} W/cm^2 and 3×10^{20} W/cm^2 on the proton target, respectively. A double stage pulse cleaning system, including an XPW module at the laser front end (cf. section 3.1.1) and a plasma mirror, is employed in the beam path of the interaction beam in order to ensure the integrity of the interaction target before the interaction with the main pulse.
The experiments are carried out using two different polarisations in the interaction beam. In order to change the polarisation from linear to circular, a zero-order quarter-waveplate is used. The quarter-waveplate is placed in the beam path of the interaction beam after the plasma mirror.
As a detector Radiochromic films are used (cf. chapter 3.4), which give high spatial and temporal resolution. The geometrical magnification can be calculated as described in section 3.5. In these experiments, the distance between the interaction point and the detector L is between 38 and 42 mm and the distance between the interaction point and the proton target ℓ is 4.5 mm, which eventually leads to a magnification of $M \simeq 1 + \frac{L}{\ell} \approx 9 - 10$. One stack of radiochromic films is employed along the proton target normal direction. Any modification in the proton beam due to the propagation through the interaction point can be detected. A second detector stack along the interaction target normal direction captures the proton signal.

Spatial and temporal synchronisation
The spatial and temporal synchronisation of both beams is done in the same procedure as described in chapter 5. In order to synchronise the beams spatially, a wire is imaged in tcc (target chamber centre) position in both focus diagnostics. The temporal timing of the two beams is achieved by creating a plasma in air with one beam and probing it with the second beam. As already mentioned, this procedure is accurate within ps time scale. During the experiments, the delay between the two beams is adjusted accordingly by elongating or shortening the beam path of one beam (here, the beam path of the proton beam (beam 2) is adjusted).

6.2 Effect of laser polarisation on laser-foil dynamics

In the following, the experimentally obtained proton probing results for the two different polarisation cases are going to be presented. The probing images show the distinct impact of the laser polarisation on the interaction dynamics.

6.2.1 Experimental results for linear polarisation

An exemplary image of raw data obtained during one single shot is shown in figure 6.2. Each image stands for a different probing time in a single shot. The different

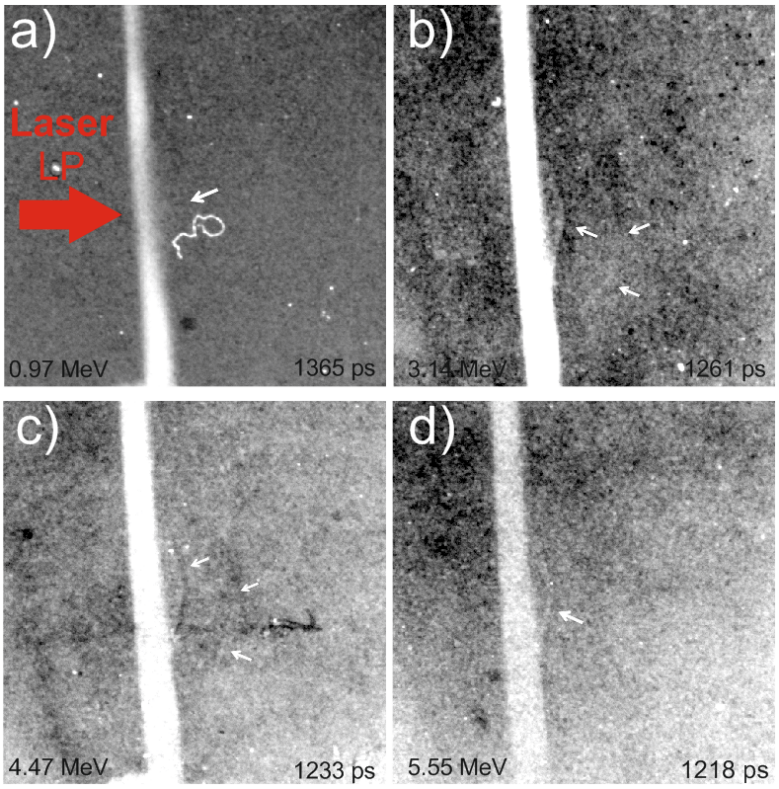

Figure 6.2: Proton probing images of a 100 nm DLC foil irradiated by a linearly polarised high-intensity laser pulse. The probing protons were accelerated from a 10 µm gold foil irradiated by another high-intensity laser pulse. All images are obtained from the same single shot. Small white arrows indicate the expansion of the foil.

probing times are due to the time of flight of the protons with different energies. In this case, the interaction target is a 100 nm thick diamond-like carbon (DLC) foil and the proton target is a gold foil of 10 µm thickness.

The evolution of the interaction between the laser pulse and the thin foil at different probing times can be seen. The interaction beam is linearly polarised and has an energy of approximately 2.8 J. Considering a throughput of the system (up to the interaction chamber) of 30 % the energy on the target is reaching 0.84 J. The delay between the two pulses is 1160 ps (interaction beam coming earlier).

Each image (a)-d)) corresponds to an RCF in the RCF stack detector and thus to a different probing time and proton energy (cf. 3.5). The corresponding proton energy on each RCF is given in the bottom left corner and the probing time in the

bottom right corner of each image.
The colouring on the RCFs is proportional to the proton flux. The darker the colour on the RCF, the higher the proton flux.
The foil has expanded significantly in the central part. The expansion at the center is about 185 μm and at the edges 34 μm. The effect of the linear polarised laser pulse can be seen clearly: the target is decompressed significantly. For linear polarisation, the decompression of the target is due to the electron heating.
Hatchett et al. presented in [60] a model describing the accelerated electrons. Only a few electrons penetrating the target can actually escape. Thus the rest is pulled back by the positive potential of the target. These electrons are drifting traversely and are oscillating though the target. A cloud of hot electrons is built up, resembling a sheath of the rear surface of the target. Due to this sheath, an electric field is built up which is strong enough to accelerate ions (cf. 2.5.1). A strong charge separation over a small scale length results in a strong electric field given by:

$$\mid E \mid \approx \frac{k_B T_{hot}}{e\lambda_D} \tag{6.2.1}$$

where $\lambda_D = (\epsilon_0 k_B T_{hot}/e^2 n_e^2)^{1/2}$ is the Debye length. With $k_B T_{hot} \sim 3.3$ MeV and $n_e = 10^{19}\mathrm{cm}^{-3}$, the Debye length is hence estimated to be $\lambda_D = 4.3$ μm, which leads to an electrical field strength of $E \sim 10^{12}$ V/m. Until the electrons are cooled down, the electric field is accelerating ions. Ions can be accelerated until the Debye length becomes equal to the ion scale length $\lambda_D = \lambda_{ion} = c_s t$, with c_s the ion sound speed. Reaching that point, a charge separation is no longer given [152].
Comparing the interaction between a linearly polarised beam and a thin foil target to the interaction between a circularly polarised interaction beam and a thin foil, major differences are observed.

6.2.2 Experimental results for circular polarisation

In figure 6.3, exemplary RCF images of a single shot interaction between a circularly polarised interaction beam and a thin foil target are shown. The experimental parameters are comparable to the linearly polarised case: the energy of the interaction beam on the target is 0.84 J and the energy of the probing beam on the proton target 1.8 J. The delay between the two pulses is 1160 ps, thus the interaction beam is impinging almost 1 ns earlier on the target than the probing beam. Contrary to the linearly polarised case the interaction between the high intensity laser pulse and thin foil shows different features. The whole foil is pushed

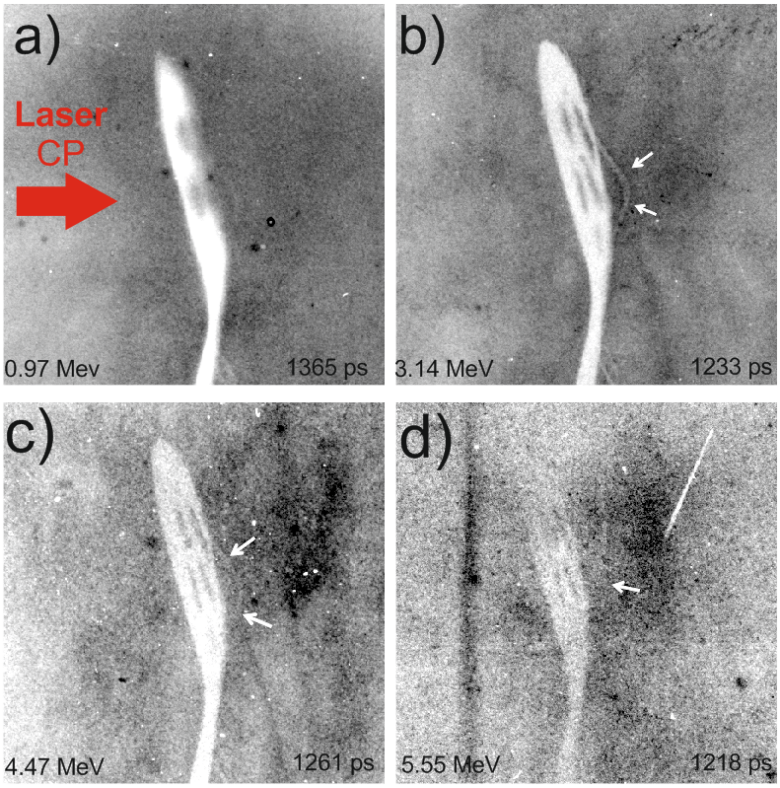

Figure 6.3: Proton probing images of a 100 nm DLC foil irradiated by a circularly polarised high-intensity laser pulse. As in the linearly polarised case, the probing protons were accelerated from a 10 µm gold foil. The images are obtained from one single shot. Corresponding probing times are given in the bottom right corner. Small white arrows indicate the expanding foil.

forward in a Gaussian shape.

It is remarkable that the target is deformed in almost a Gaussian-like shape and has moved as a whole from its initial position (cf. figure 6.3). The width of the central layer is 54 µm, which indicates a notable expansion of the initially 100 nm foil target. Although the target has expanded significantly, it still moves as a dense compressed layer. The ultra high contrast of the laser pulse ($\sim 10^{-12}$) keeps the integrity of the target intact during the interaction and ensures the ponderomotive light pressure of approximately $P = (1 + R)I/c \approx 2I/c \approx 100$ Gbar (for solid densities R $\simeq$ 1) is sufficient enough to accelerate the target forward. Due to the Gaussian intensity profile, the central region of the target has expanded more than at the edges. While the central part of the foil shown in figure 6.3 b) has expanded 44 µm, the edges have expanded only 34 µm. The intensity of the laser pulse is highest at the central region of the Gaussian profile, thus driving a stronger

ponderomotive force. As also shown numerically and experimentally for example in [28] [61], irradiating a thin solid foil target with a linearly polarised laser pulse results in a strong expansion of the target induced by the hot electrons. Changing the polarisation to circular, the foil is accelerated as a quasineutral plasma bunch. The target is pushed forward as a dense compressed layer.
Considering the ponderomotive force acting on the electrons (cf. section 2.4.2)

$$f_P = -\frac{m}{4}\frac{\partial v_{os}^2}{\partial x}(1 - cos2\omega t). \tag{6.2.2}$$

the oscillating term is vanishing for circularly polarised laser light, which is given by the second term of the above mentioned equation. The heating of the electrons is suppressed leading to a mechanical equilibrium and thus the electrostatic and ponderomotive force balancing each other. Only the non-oscillating term (left-hand-side of the ponderomotive force term) is transferring a steady pressure to the ions via space-charge.
The radiation pressure pushes the electrons in longitudinal direction, which eventually leads to the removal of the electrons from the foil. If the radiation pressure equals the electrostatic pressure, a density distribution is created where all electrons pile up at the rear surface of the target. Since for R $\simeq$ 1 the ponderomotive force and also the electrostatic field vanishes, no electrons are ejected from the rear surface of the target [153].
The equilibrium between the electrostatic pulse and the ponderomotive force ceases as soon as the laser pulse is off. The equilibrium is only reached if the charge depletion length d is close to the target thickness ℓ [153]. The depletion depth d can be estimated using the equilibrium condition

$$P_{es} = (2\pi/en_0d)^2 \simeq 2I/c$$

assuming a reflectivity of R $\simeq$ 1. The depletion depth is found to be $d \simeq \ell(a_0/\xi) \leq \ell$.
Once the equilibrium vanishes, the hydrodynamic expansion commences. A sheath field at the rear side of the target is built up by the hot electrons traversing the target. Eventually, the TNSA phase is reached.
Since the probing time is very late, the very early acceleration of ions/protons within a few ps after the interaction cannot be detected. Nevertheless, the acceleration process can be retraced from the foil dynamics, since the foil dynamics and acceleration process are closely related. Hence, the physical process during the laser-foil interaction can be determined by the state of the foil at late probing times.

On the radiochromic films a deflection of the charged proton of the edges of the target can be seen. A charge field is build up at the edges due to the high density gradient. Thus the state of the foil and the physical condition become visible. Taking the laser and target parameters used here into account, it is identified that the acceleration is mainly driven by the hole boring regime of the radiation pressure acceleration.
Assuming a Gaussian intensity profile and a laser pulse duration of 30 fs, the hole boring velocity can be estimated to be 10^8 cm/s (using formula 2.5.2). The estimated foil velocity is one order of magnitude lower than the initial hole boring velocity which is estimated to be 10^7 cm/s. This indicates that the target is moving ballistically into the vacuum. The target is moving very slowly. Comparing the images from the second and third layer (cf. figure 6.3), features in both images look almost the same. Between these two RCF layers is a time interval of approximately 28 ps. Within this time interval, the expansion is only 17 μm.
Since the radiochromic films used here as detector have a time integration feature, it is not possible to distinguish between hole-boring and TNSA driven protons. The above mentioned hole boring velocity would correspond to a proton energy of approximately 1 MeV. However, since the radiochromic films are always wrapped in 14 μm Aluminium foil to protect the radiochromic films from direct exposure to laser light, 1 MeV Protons are stopped by the Aluminium foil and do not reach the radiochromic film. The first layer of the detector stack corresponds to a proton energy of 3.14 MeV (cf. chapter 3.4).

6.3 Simulations

In order to confirm the experimental investigations, particle tracer and PIC-simulations are going to be presented.
Particle tracer simulations performed by L. Romagnani via the 3D particle tracer code *qTrace* [154] are demonstrated in figure 6.4. The spatial and temporal evolution of the electric and magnetic fields can be inferred. Running the IDL based qTrace simulations, three main steps are involved: a probe proton beam is generated at the source (1) before propagating through the interaction region (2) and eventually impinging on a detector (3).
By obtaining a match between the experimentally measured and the via particle tracer computed proton density, the spatial character of the induced quasistatic fields can be inferred. For the images shown in figure 6.4, a Gaussian density

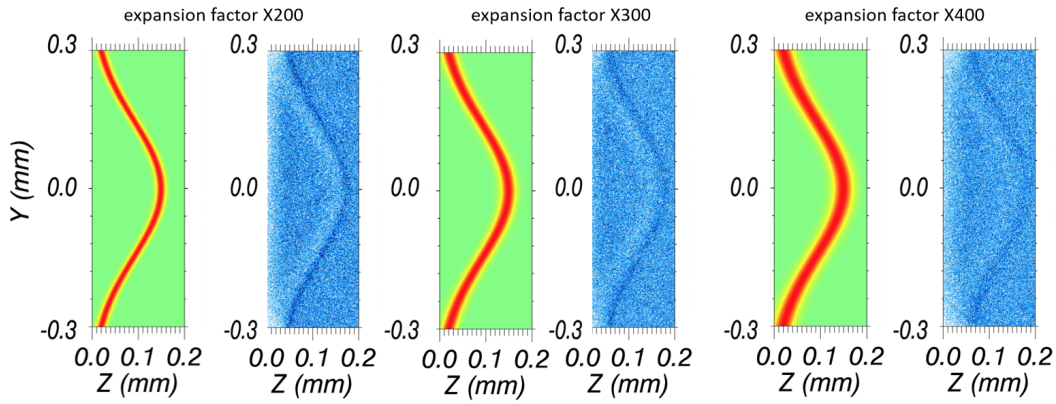

Figure 6.4: Particle tracing simulations results obtained via the particle tracer code qTrace. Different expansion factors are shown in order to find the best match between the experiments and simulations. The simulations are performed by L. Romagnani.

profile is used and the total mass is conserved in order to obtain an improved resemblance with the experimental data. Different expansion factors are considered (200, 300 and 400) in order to determine the best match with the experimentally recorded proton probing images. Furthermore, 2D PI simulations provided by R. Prasad support the experimental investigations. The simulations are performed using the open source PIC code EPOCH for high energy density physics [156]. For the images shown in figure 6.5 a target density of 470 n_c, a target thickness of 100 nm DLC, a plasma scale length of 30 nm and an angle of incidence of 25° are chosen. The simulation run time is 150 fs in this case. Images a) and c) in figure 6.5 show a comparison of the carbon density distribution between the circularly (left) and linearly (right) polarised laser light case. The simulation results confirm the experimental investigations demonstrated above. In the circularly polarised case, the whole target is pushed forward as a compressed layer. For a linearly polarised laser pulse, the target is decompressed significantly. The simulations confirm and support the experimentally obtained proton probing images of the heating process with two different laser polarisations.

Similar results are obtained for the electron density distribution for both polarisation cases. The same feature as in the ion density distribution can be observed. The target is pushed forward as a dense compressed layer and a Gaussian shape can be recognised in the circularly polarised case.

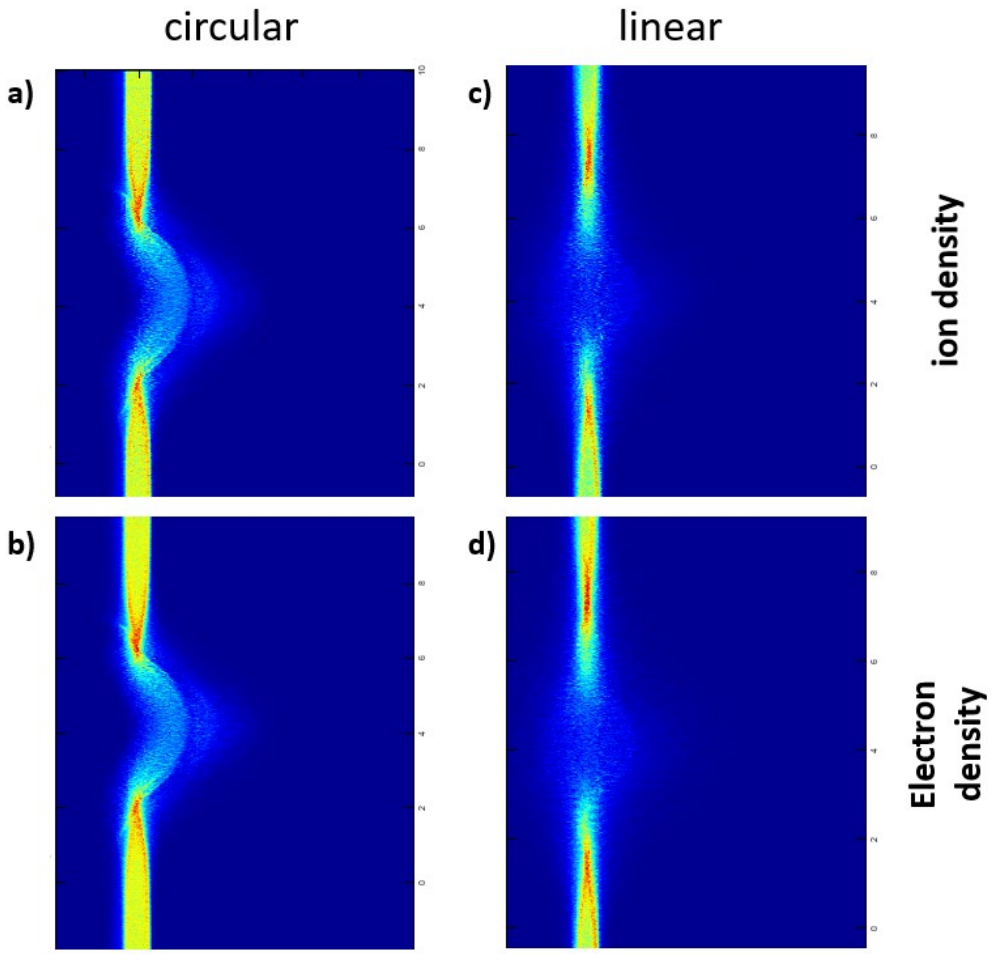

Figure 6.5: 2D PIC simulation results for two different laser pulse polarisations and intensities. On the left-hand-side the simulation results for circularly polarised (a), b)) and on the right-hand-side for linearly polarised laser light (c), d)) are given, respectively. In this case, the target is pushed forward as a dense compressed layer. The simulation results are provided by R. Prasad.

6.4 Conclusion

In this chapter, the experimental results showing the effect of linearly and circularly polarised laser light on the target heating is presented. Proton probing images showing the distinct impact of the change of the laser light polarisation are used as a diagnostic tool providing high temporal and spatial resolution. While in the linearly polarised case the target is significantly decompressed by the laser pulse, in the circularly polarised case the whole target is pushed forward as a compressed layer.

The experimental results confirm previous simulation studies exploring the central

influence of the laser light polarisation. The experiments proved the crucial effect of the light polarisation on the target heating. In case of linear polarisation, the oscillarity term of the ponderomotive force is leading to a significant electron heating suppressing the effect of the radiation pressure. For circularly polarised light, the electron heating is reduced favouring the RPA process. The electron population maintains its structure and is being pushed forward by the laser pulse. For the first time, the effect of the laser light polarisation could be shown and visualised experimentally. The proton probing technique is delivering a time-resolved analysis with a high spatial and temporal resolution, which allows capturing the interaction dynamics on radiographic images.

The study presented here will serve as a support to understand the RPA process better and will lead the path for its applications in producing energetic and high-quality proton beams.

Nevertheless, the 2D PIC simulations are only providing an indication of the electron and ion density distributions. In order to have a more detailed description of the heating process in both polarisation cases 3D simulations need to be provided. However, the 2D simulation results are already a convenient support for the experimentally observed effect of the polarisation in the heating process of a laser irradiated thin foil target.

7 Summary and Outlook

In this chapter, the experimental investigations and results are summarised and conducted with prospect of future research possibilities.
The experiments presented in this thesis are based on the interaction of ultra-short, high-intensity laser pulses with ultra-thin solid foil targets. Various experimental investigations addressed different physical phenomena. The versatile Arcturus laser facility empowers numerous possibilities of experimental campaigns.
In the first part of the experiments in this thesis, the investigations concentrate on the absorption processes and ion acceleration mechanisms in a dual beam experimental arrangement.
The plasma dynamics are investigated using various diagnostics. The delay between the two high-intensity laser pulses is varied in order to investigate a plasma with varying intensity. As the plasma is expanding with larger delays, the plasma is getting underdense. Considering larger delays (i.e. an expanded and already underdense plasma), a lower absorption fraction would be expected. However, the experimental investigations revealed that depending on the laser energy, the transmitted laser energy is reaching a minimum point at a specific delay. Analytical calculations showed that collisional absorption mechanisms become relevant at late delays and show a similar trend like the measured transmission data. A maximum in the absorption fraction is reached at a specific delay (or rather plasma extend). This maximum in the calculated absorption fraction is correlated with the minimum in the measured transmitted energy.
The absorption measurements are confirmed by monitoring the laser energy in laser direction. The beam shape and size could be monitored and showed a correlation between the delay and the transmitted energy. At the recorded minimum transmitted energy, less transmitted light was observed on the calorimeter and on the PTFE around the calorimeter's active area.
Moreover, a 2ω-imaging system transverse to the interaction direction could monitor the channelling of the laser pulse through the expanding plasma. Using the solution for the propagation of an electromagnetic wave inside a waveguide the laser pulse energy can be estimated. The experimentally measured values for the channel length of the laser pulse propagating through the pre-heated plasma are in good agreement with the waveguide theorem.
Furthermore, another notable feature is observed in the accelerated proton energies. While the transmission is reaching a minimum (and the absorption is reaching a

maximum), the protons are accelerated to energies almost a factor of two higher than in a single beam interaction. Previous studies from other working groups demonstrated that in this density regime favourable conditions for a shock-like acceleration mechanism are reached. However, previous studies did not show the same behaviour in the absorption fraction/transmitted energy. In future investigations, simulations also considering the collisional absorption mechanism should be carried out in order to confirm the experimental investigations.

The second part of this thesis deals with the investigation of the positive charging of a laser irradiated wire target by means of the proton probing technique. Protons accelerated from a thin target by a high-intense laser pulse were employed to image the interaction via a proton projection of the probed region. The spectral and spatial properties of laser accelerated ions were exploited, yielding the resolving of the transient field distribution and the evolution with high spatial and temporal resolution. A detailed parametric study of the electromagnetic pulse was performed, varying different laser parameters, including energy, pulse duration and intensity. The studies revealed a strong dependence of these parameters on the amplitude of the electromagnetic pulse. An optimum pulse length for a given laser energy could be found. Furthermore, experiments could demonstrate the dependence of the net charge on the laser intensity.
A semi-analytical/empirical model supported and confirmed the experimentally obtained data. Using the ChoCoLaT II code, the optimum pulse duration and total net charge could be verified. Furthermore, simulations over a wide range of laser parameters allow to predict and optimise the electromagnetic pulse for future laser facilities, since these will be able to reach higher laser energies and intensities. While in the experimental regime investigated in this thesis pulse durations of the electromagnetic pulse of approximately 150 fs are predicted, for upcoming laser facilities with anticipated laser energies on target around 10s of J, the pulse durations of the electromagnetic pulse are estimated to be around a few ps. A benchmark for different laser parameters could be established. The understanding of the dynamics of the (wire) target charging is important for various applications. An improved understanding of the dynamics can be a guidance for example for the post-acceleration of proton beams. Since laser-driven ion beams still have limitations in peak ion energy, beam divergence and bandwidth of the energy spectrum, new techniques like the helical coil structure for post-acceleration need to be studied. Here, the laser-driven electromagnetic pulse is guided along a helical coil wire target surrounding the laser-accelerated ion beam devoting to the

deficiencies. The investigations in this thesis will support improving and adjusting the experimental study of the post-acceleration mechanism. For future experiments, the optimised laser parameters will already be provided, which will be conducive and beneficial to the synchronisation of the electromagnetic pulse and time of flight of the laser-accelerated ion/proton beam. Also, an optimum net charge and amplitude of the electromagnetic pulse will be given.

The third and last part of this thesis is presenting the proton imaging of the dynamics of the interaction between a high-intensity, high-contrast laser and ultra-thin foil targets. For probing the interaction the proton probing technique is exploited since the properties of the laser driven proton beams (i.e. high laminarity, low divergence, small source size) are most suited for detecting electric fields. These unique properties allows a time-resolved analysis and deliver a high temporal resolution.
The experimental studies presented here consolidate former theoretical investigations on the effect of the light polarisation on the dynamics of the interaction between (ultra-)thin solid targets and high-intensity laser pulses. Here, two different polarisations, i.e. linear and circular polarisation, are considered. The proton probing images revealed that the polarisation of the laser pulse has a great impact on the acceleration scheme. In the linearly polarised case, target normal sheath acceleration is the dominant process in accelerating the protons to multi-MeV-range. Changing to circularly polarised light, the electron heating is reduced, which leads to the radiation pressure acceleration.
For the first time, the difference between both acceleration mechanisms is demonstrated by imaging the interaction experimentally via proton probing. The distinct difference in the interaction between both polarisations can be seen. The proton probing images precisely show that for circularly polarised light the target is being pushed forward in the direction of the laser pulse propagation as a compressed layer, whereas for linearly polarised light the interaction results in a strong expansion of the foil target. For circular polarisation, the electron population maintains its structure and is being pushed forward by the laser pulse. The Gaussian shape-size of the tightly focused laser pulse can also be recognised in the shape of the acceleration of the foil imaged by protons. Considering the linearly polarised case, electrons are heated heavily, leading to a significantly higher expansion of the target.
The experimental investigations are supported by 2D PIC simulations showing the effect of the laser polarisation on the efficiency of the electron heating process. However, for future investigations 3D simulations have to be considered . The 2D

simulation results are only an indication for the heating processes, which are taking place due to the irradiation of a thin foil target by a high-intensity laser pulse.

Bibliography

[1] T. H. Maiman, *Stimulated Optical Radiation in Ruby.* Nature **187** (1960), pp. 493–494.

[2] Peter V. Nickles, Karol A. Janulewicz, and W. Sandner, *Laser: Röntgenlaser auf dem Wege zu Tabletop-Systemen: Dank neuer Pumpverfahren passen Röntgenlaser inzwischen in ein kleines Labor.* Physik Journal **56** (2000), pp. 43–48.

[3] G. Mourou and D. Strickland, *Compression of Amplified Chirped Optical Pulses.* Optics Communications **56** (1985), pp. 219–221.

[4] K. Merghem, A. Akrout, A. Martinez, G. Moreau, J. P. Tourrenc, F. Lelarge, F. Van Dijk, G. H. Duan, G. Aubin, and A. Ramdane, *Short Pulse Generation Using a Passively Mode Locked Dingle InGaAsP/InP Quantum Well Laser.* Optics Express **16** (2008), pp. 10675–10683.

[5] T. Feder, *Petawatt Laser Probes Nature at Texas university.* Physics Today **61** (2008), pp. 27–27.

[6] C. Danson, D. Hillier, N. Hopps, and D. Neely, *Petawatt Class Lasers Worldwide.* High Power Laser Science and Engineering **3** (2015).

[7] A. Modena, Z. Najmudin, A. E. Dangor, C. E. Clayton, K. A. Marsh, C. Joshi, V. Malka, C. B. Darrow, C. Danson, D. Neely, and F. N. Walsh, *Electron Acceleration from the Breaking of Relativistic Plasma Waves.* Nature **377** (1995), pp. 606–608.

[8] V. T. Tikhonchuk, *Interaction of a Beam of Fast Electrons with Solids.* Physics of Plasmas **9** (2002), pp. 1416–1421.

[9] R. D. Edwards, M. A. Sinclair, T. J. Goldsack, K. Krushelnick, F. N. Beg, E. L. Clark, A. E. Dangor, Z. Najmudin, M. Tatarakis, B. Walton, M. Zepf, K. W. D. Ledingham, I. Spencer, P. A. Norreys, R. J. Clarke, R. Kodama, Y. Toyama, and M. Tampo, *Characterization of a Gamma-ray Source Based on a Laser-Plasma Accelerator with Applications to Radiography.* Applied Physics Letters **80** (2002), pp.2129–2131.

[10] E. L. Clark, K. Krushelnick, M. Zepf, F. N. Beg, M. Tatarakis, A. Machacek, M. I. Santala, I. I. Watts, P. A. Norreys, and A. E. Dangor, *Energetic Heavy-Ion and Proton Generation from Ultraintense Laser-Plasma Interactions with Solids.* Phys Rev Lett **85** (2000), pp. 1654–7.

[11] R. A. Snavely, M. H. Key, S. P. Hatchett, T. E. Cowan, M. Roth, T. W. Phillips, M. A. Stoyer, E. A. Henry, T. C. Sangster, M. S. Singh, S. C. Wilks, A. MacKinnon, A. Offenberger, D. M. Pennington, K. Yasuike, A. B. Langdon, B. F. Lasinski, J. Johnson, M. D. Perry, and E. M. Campbell, *Intense High-energy Proton Beams from Petawatt-Laser irradiation of Solids.* Phys Rev Lett **85** (2000), pp. 2945–8.

[12] A. Higginson, R. J. Gray, M. King, R. J. Dance, S. D. R. Williamson, N. M. H. Butler, R. Wilson, R. Capdessus, C. Armstrong, J. S. Green, S. J. Hawkes, P. Martin, W. Q. Wei, S. R. Mirfayzi, X. H. Yuan, S. Kar, M. Borghesi, R. J. Clarke, D. Neely, and P. McKenna, *Near-100 MeV Protons via a Laser-Driven Transparency-Enhanced Hybrid Acceleration Scheme.* Nat Commun **9** (2018), p. 724.

[13] M. Borghesi, D. H. Campbell, A. Schiavi, M. G. Haines, O. Willi, A. J. MacKinnon, P. Patel, L. A. Gizzi, M. Galimberti, R. J. Clarke, F. Pegoraro, H. Ruhl, and S. Bulanov, *Electric Field Detection in Laser-Plasma Interaction Experiments via the Proton Imaging Technique.* Physics of Plasmas **9** (2002), pp. 2214–2220.

[14] M. Borghesi, A. Schiavi, D. H. Campbell, M. G. Haines, O. Willi, A. J. MacKinnon, L. A. Gizzi, M. Galimberti, R. J. Clarke, and H. Ruhl, *Proton Imaging: A Diagnostic for Inertial Confinement Fusion/Fast Ignitor Studies.* Plasma Physics and Controlled Fusion **43** (2001), pp. A267–A276.

[15] M. Tabak, J. Hammer, M. E. Glinsky, W. L. Kruer, S. C. Wilks, J. Woodworth, E. M. Campbell, M. D. Perry, and R. J. Mason, *Ignition and High-Gain with Ultrapowerful Lasers.* Physics of Plasmas **1** (1994), pp. 1626–1634.

[16] R. Betti and O. A. Hurricane, *Inertial-Confinement Fusion with Lasers.* Nature Physics **12** (2016), pp. 435–448.

[17] S. V. Bulanov and V. S. Khoroshkov, *Feasibility of Using Laser Ion Accelerators In Proton Therapy.* Plasma Physics Reports **28** (2002), pp.453–456.

[18] V. Malka, S. Fritzler, E. Lefebvre, E. d'Humieres, R. Ferrand, G. Grillon, C. Albaret, S. Meyroneinc, J. P. Chambaret, A. Antonetti, and D. Hulin, *Practicability of Protontherapy Using Compact Laser Systems.* Med Phys **31** (2004), pp. 1587–92.

[19] M. Hegelich, S. Karsch, G. Pretzler, D. Habs, K. Witte, W. Guenther, M. Allen, A. Blazevic, J. Fuchs, J. C. Gauthier, M. Geissel, P. Audebert, T. Cowan, and M. Roth, *MeV Ion Jets from Short-Pulse-Laser Interaction with Thin Foils.* Phys Rev Lett **89** (2002), p. 085002.

[20] E. L. Clark, K. Krushelnick, J. R. Davies, M. Zepf, M. Tatarakis, F. N. Beg, A. Machacek, P. A. Norreys, M. I. Santala, I. I. Watts, and A. E. Dangor, *Measurements of Energetic Proton Transport Through Magnetized Plasma from Intense Laser Interactions with Solids.* Phys Rev Lett **84** (2000), pp. 670–3.

[21] S. C. Wilks, A. B. Langdon, T. E. Cowan, M. Roth, M. Singh, S. Hatchett, M. H. Key, D. Pennington, A. MacKinnon, and R. A. Snavely, *Energetic Proton Generation in Ultra-Intense Laser-solid Interactions.* Physics of Plasmas **8** (2001), pp. 542–549.

[22] L. Robson, P. T. Simpson, R. J. Clarke, K. W. D. Ledingham, F. Lindau, O. Lundh, T. McCanny, P. Mora, D. Neely, C. G. Wahlström, M. Zepf, and P. McKenna, *Scaling of Proton Acceleration Driven by Petawatt-Laser–Plasma Interactions.* Nature Physics **3** (2006), pp. 58–62.

[23] M. Borghesi, A. Bigongiari, S. Kar, A. Macchi, L. Romagnani, P. Audebert, J. Fuchs, T. Toncian, O. Willi, S. V. Bulanov, A. J. Mackinnon, and J. C. Gauthier, *Laser-Driven Proton Acceleration: Source Optimization and Radiographic Applications.* Plasma Physics and Controlled Fusion **50** (2008).

[24] V. Malka, J. Faure, Yann A. Gauduel, E. Lefebvre, A. Rousse, and Kim Ta Phuoc, *Principles and Applications of Compact Laser–Plasma Accelerators.* Nature Physics **4** (2008), pp. 447–453.

[25] Y. Sentoku, T. E. Cowan, A. Kemp, and H. Ruhl, *High Energy Proton Acceleration in Interaction of Short Laser Pulse with Dense Plasma Target.* Physics of Plasmas **10** (2003), pp. 2009–2015.

[26] P. Mora, *Plasma Expansion Into a Vacuum.* Phys Rev Lett **90** (2003), p. 185002.

[27] T. V. Liseikina and A. Macchi, *Features of Ion Acceleration by Circularly Polarized Laser Pulses.* Applied Physics Letters **91** (2007).

[28] A. Henig, S. Steinke, M. Schnurer, T. Sokollik, R. Horlein, D. Kiefer, D. Jung, J. Schreiber, B. M. Hegelich, X. Q. Yan, J. Meyer-ter Vehn, T. Tajima, P. V. Nickles, W. Sandner, and D. Habs, *Radiation-Pressure Acceleration of Ion Beams Driven by Circularly Polarized Laser Pulses.* Phys Rev Lett **103** (2009), p. 245003.

[29] A. Macchi and C. Benedetti, *Ion Acceleration by Radiation Pressure in Thin and Thick Targets.* Nuclear Instruments and Methods in Physics Research Section a-Accelerators Spectrometers Detectors and Associated Equipment **620** (2010), pp. 41–45.

[30] H.-P. Schlenvoigt, and O. Jäckel, and S. M. Pfotenhauer, and M. C Kaluza, *Laser-Based Particle Acceleration.* Advances in Solid State Lasers Development and Applications, IntechOpen, 2010.

[31] T. Tajima, D. Habs, and X. Yan, *Laser Acceleration of Ions for Radiation Therapy.* Reviews of Accelerator Science and Technology **02** (2012), pp. 201–228.

[32] A. M. M. Schiavi. *Study of Laser Produced Plasmas by X-Ray and Proton Radiography.* Doctoral thesis, 2003.

[33] M. Borghesi, D. H. Campbell, A. Schiavi, O. Willi, A. J. Mackinnon, D. Hicks, P. Patel, L. A. Gizzi, M. Galimberti, and R. J. Clarke, *Laser-Produced Protons and their Application as a Particle Probe.* Laser and Particle Beams **20** (2002).

[34] L. Romagnani, J. Fuchs, M. Borghesi, P. Antici, P. Audebert, F. Ceccherini, T. Cowan, T. Grismayer, S. Kar, A. Macchi, P. Mora, G. Pretzler, A. Schiavi, T. Toncian, and O. Willi, *Dynamics of Electric Fields Driving the Laser Acceleration of Multi-MeV Protons.* Phys Rev Lett **95** (2005), p. 195001.

[35] S. Palaniyappan, B. M. Hegelich, H. C. Wu, D. Jung, D. C. Gautier, L. Yin, B. J. Albright, R. P. Johnson, T. Shimada, S. Letzring, D. T. Offermann, J. Ren, C. K. Huang, R. Horlein, B. Dromey, J. C. Fernandez, and R. C. Shah, *Dynamics of Relativistic Transparency and Optical Shuttering in Expanding Overdense Plasmas.* Nature Physics **8** (2012), pp. 763–769.

[36] P. Gibbon. *Short Pulse Laser Interactions with Matter: An Introduction.* Imperial College Press, London, 2005.

[37] S. Eliezer. *The Interaction of High-Power Lasers with Plasmas.* CRC Press, 2002.

[38] William L. Kruer. *The Physics of Laser Plasma Interactions.* Frontiers in physics. Westview Pr, Boulder Col., 2003.

[39] Francis F. Chen. *Introduction to Plasma Physics and Controlled Fusion.* 2016.

[40] V. S. Popov, *Tunnel and Multiphoton Ionization of Atoms and Ions in a Strong Laser Field (Keldysh Theory).* Physics-Uspekhi **47** (2004), pp. 855–885.

[41] J. R. Davies, *Laser absorption by overdense plasmas in the relativistic regime.* Plasma Physics and Controlled Fusion **51** (2009), p. 014006.

[42] L. Schlessinger and J. Wright, *Inverse-Bremsstrahlung Absorption Rate in an Intense Laser Field.* Physical Review A **20** (1979), pp. 1934–1945.

[43] John F. Seely and Edward G. Harris, *Heating of a Plasma by Multiphoton Inverse Bremsstrahlung.* Physical Review A **7** (1973), pp. 1064–1067.

[44] P. Gibbon and A. R. Bell, *Collisionless Absorption in Sharp-Edged Plasmas.* Phys Rev Lett **68** (1992), pp. 1535–1538.

[45] N. G. Denisov, *Resonance Absorption of Electromagnetic Waves by an Inhomogeneous Plasma.* Soviet Physics Jetp-Ussr **7** (1958), pp.364–365.

[46] N. G. Denisov, *On a Singularity of the Field on an Electromagnetic Wave Propagated in an Inhomogeneous Plasma.* Soviet Physics Jetp-Ussr **4** (1957), pp.544–553.

[47] T. Speziale and P. J. Catto, *Linear Wave Conversion in an Unmagnetized, Collisionless Plasma.* Physics of Fluids **20** (1977).

[48] Z. M. Sheng, S. M. Weng, L. L. Yu, W. M. Wang, Y. Q. Cui, M. Chen, and J. Zhang, *Absorption of Ultrashort Intense Lasers in Laser-Solid Interactions.* Chinese Physics B **24** (2015), p. 015201.

[49] F. Brunel, *Not-so-resonant, resonant absorption.* Phys Rev Lett **59** (1987), pp. 52–55.

[50] T. Y. B. Yang, W. L. Kruer, R. M. More, and A. B. Langdon, *Absorption of Laser-Light in Overdense Plasmas by Sheath Inverse Bremsstrahlung.* Physics of Plasmas **2** (1995), pp. 3146–3154.

[51] P. J. Catto and R. M. More, *Sheath Inverse Bremsstrahlung in Laser-Produced Plasmas.* Physics of Fluids **20** (1977), pp. 704–705.

[52] W. Kruer and K. Eastabrook, *J×B Heating by Very Intense Laser Light.* Physics of Fluids **28** (1985), pp. 430–432.

[53] R. Jung. *Laser-plasma interaction with ultra-short laser pulses.* Doctoral thesis (2005).

[54] Hong-bo Cai, Wei Yu, Shao-ping Zhu, and Chun-yang Zheng, *Short-Pulse Laser Absorption via J x B Heating in Ultrahigh Intensity Laser Plasma Interaction.* Physics of Plasmas **13** (2006), p. 113105.

[55] Yun-Qian Cui, Wei-Min Wang, Zheng-Ming Sheng, Yu-Tong Li, and Jie Zhang, *Laser Absorption and Hot Electron Temperature Scalings in Laser–Plasma Interactions.* Plasma Physics and Controlled Fusion **55** (2013), p. 085008.

[56] A. Maksimchuk, S. Gu, K. Flippo, D. Umstadter, and V. Y. Bychenkov, *Forward Ion Acceleration in Thin Films Driven by a High-Intensity Laser.* Phys Rev Lett **84** (2000), pp. 4108–11.

[57] S. J. Gitomer, R. D. Jones, F. Begay, A. W. Ehler, J. F. Kephart, and R. Kristal, *Fast Ions and Hot Electrons in the Laser–Plasma Interaction.* Physics of Fluids **29** (1986), p. 2679.

[58] A. P. Fews, P. A. Norreys, F. N. Beg, A. R. Bell, A. E. Dangor, C. N. Danson, P. Lee, and S. J. Rose, *Plasma Ion Emission from High Intensity Picosecond Laser Pulse Interactions with Solid Targets.* Phys Rev Lett **73** (1994), pp. 1801–1804.

[59] A. Macchi, M. Borghesi, and M. Passoni, *Ion Acceleration by Superintense Laser-Plasma Interaction.* Reviews of Modern Physics **85** (2013), pp. 751–793.

[60] S. P. Hatchett, C. G. Brown, T. E. Cowan, E. A. Henry, J. S. Johnson, M. H. Key, J. A. Koch, A. B. Langdon, B. F. Lasinski, R. W. Lee, A. J. Mackinnon, D. M. Pennington, M. D. Perry, T. W. Phillips, M. Roth, T. C. Sangster, M. S. Singh, R. A. Snavely, M. A. Stoyer, S. C. Wilks, and K. Yasuike, *Electron,*

Photon, and Ion Beams from the Relativistic Interaction of Petawatt Laser Pulses with Solid Targets. Physics of Plasmas **7** (2000), pp. 2076–2082.

[61] A. P. L. Robinson, M. Zepf, S. Kar, R. G. Evans, and C. Bellei, *Radiation Pressure Acceleration of Thin Foils with Circularly Polarized Laser Pulses.* New Journal of Physics **10** (2008), p. 013021.

[62] T. Schlegel, N. Naumova, V. T. Tikhonchuk, C. Labaune, I. V. Sokolov, and G. Mourou, *Relativistic Laser Piston Model: Ponderomotive Ion Acceleration in Dense Plasmas Using Ultraintense Laser Pulses.* Physics of Plasmas **16** (2009), p. 083103.

[63] A. Macchi, F. Cattani, T. V. Liseykina, and F. Cornolti, *Laser Acceleration of Ion Bunches at the Front Surface of Overdense Plasmas.* Phys Rev Lett **94** (2005), p. 165003.

[64] C. A. Palmer, N. P. Dover, I. Pogorelsky, M. Babzien, G. I. Dudnikova, M. Ispiriyan, M. N. Polyanskiy, J. Schreiber, P. Shkolnikov, V. Yakimenko, and Z. Najmudin, *Monoenergetic Proton Beams Accelerated by a Radiation Pressure Driven Shock.* Phys Rev Lett **106** (2011), p. 014801.

[65] A. Macchi, S. Veghini, T. V. Liseykina, and F. Pegoraro, *Radiation Pressure Acceleration of Ultrathin Foils.* New Journal of Physics **12** (2010), p. 045013.

[66] S. Kar, K. F. Kakolee, B. Qiao, A. Macchi, M. Cerchez, D. Doria, M. Geissler, P. McKenna, D. Neely, J. Osterholz, R. Prasad, K. Quinn, B. Ramakrishna, G. Sarri, O. Willi, X. Y. Yuan, M. Zepf, and M. Borghesi, *Ion Acceleration in Multispecies Targets Driven by Intense Laser Radiation Pressure.* Phys Rev Lett **109** (2012), p. 185006.

[67] S. S. Bulanov, E. Esarey, C. B. Schroeder, S. V. Bulanov, T. Zh Esirkepov, M. Kando, F. Pegoraro, and W. P. Leemans, *Radiation Pressure Acceleration: The Factors Limiting Maximum Attainable Ion Energy.* Physics of Plasmas **23** (2016).

[68] S. S. Bulanov, C. B. Schroeder, E. Esarey, and W. P. Leemans, *Optimized Laser Pulse Profile for Efficient Radiation Pressure Acceleration of Ions.* Physics of Plasmas **19** (2012).

[69] M. Roth and M. Schollmeier, *Ion Acceleration—Target Normal Sheath Acceleration.* 2016 **1** (2016).

[70] S. C. Wilks, *Simulations of ultraintense laser–plasma interactions**. Physics of Fluids B: Plasma Physics **5** (1993), pp. 2603–2608.

[71] J. Fuchs, P. Antici, E. d'Humières, E. Lefebvre, M. Borghesi, E. Brambrink, C. A. Cecchetti, M. Kaluza, V. Malka, M. Manclossi, S. Meyroneinc, P. Mora, J. Schreiber, T. Toncian, H. Pépin, and P. Audebert, *Laser-Driven Proton Scaling Laws and New Paths Towards Energy Increase*. Nature Physics **2** (2005), pp. 48–54.

[72] S. C. Wilks, *Absorption of Ultra-Intense Laser Pulses*. Phys Rev Lett **69** (1992), pp. 1383–1386.

[73] G. Mourou, T. Tajima, and Sergei V. Bulanov, *Optics in the Relativistic Regime*. Reviews of Modern Physics **78** (2006), pp. 309–371.

[74] Jo. Nuckolls, L. Wood, A. Thiessen, and G. Zimmerman, *Laser Compression of Matter to Super-High Densities: Thermonuclear (CTR) Applications*. Nature **239** (1972), pp. 139–142.

[75] P. Kaw, *Relativistic Nonlinear Propagation of Laser Beams in Cold Overdense Plasmas*. Physics of Fluids **13** (1970).

[76] A. I. Akhiezer and R. V. Polovin, *Theory of Wave Motion of an Electron Plasma*. Soviet Physics Jetp-Ussr **3** (1956), pp. 696–705.

[77] C. Rullière. *Femtosecond Laser Pulses*. Advanced Texts in Physics. 2005.

[78] A. Ricci, A. Jullien, J. P. Rousseau, Y. Liu, A. Houard, P. Ramirez, D. Papadopoulos, A. Pellegrina, P. Georges, F. Druon, N. Forget, and R. Lopez-Martens, *Energy-Scalable Temporal Cleaning Device for Femtosecond Laser Pulses Based on Cross-Polarized Wave Generation*. Rev Sci Instrum **84** (2013), p. 043106.

[79] H. C. Kapteyn, M. M. Murnane, A. Szoke, and R. W. Falcone, *Prepulse Energy Suppression for High-Energy Ultrashort Pulses Using Self-Induced Plasma Shuttering*. Optics Letters **16** (1991), pp. 490–492.

[80] C. Thaury, F. Quere, J. P. Geindre, A. Levy, T. Ceccotti, P. Monot, M. Bougeard, F. Reau, P. D'Oliveira, P. Audebert, R. Marjoribanks, and P. H. Martin, *Plasma Mirrors for Ultrahigh-Intensity Optics*. Nature Physics **3** (2007), pp. 424–429.

[81] M. Cerchez, R. Prasad, B. Aurand, A. L. Giesecke, S. Spickermann, S. Brauckmann, E. Aktan, M. Swantusch, M. Toncian, T. Toncian, and O. Willi, *ARCTURUS Laser: A Versatile High-Contrast, High-Power Multi-Beam Laser System.* High Power Laser Science and Engineering **7** (2019).

[82] J. J. Thomson, *XXVI. Rays of Positive Electricity.* The London, Edinburgh, and Dublin Philosophical Magazine and Journal of Science **21** (2009), pp. 225–249.

[83] S. Ter-Avetisyan, M. Schnurer, and P. V. Nickles, *Time Resolved Corpuscular Diagnostics of Plasmas Produced with High-Intensity Femtosecond Laser Pulses.* Journal of Physics D-Applied Physics **38** (2005), pp. 863–867.

[84] D. Jung, R. Horlein, D. Kiefer, S. Letzring, D. C. Gautier, U. Schramm, C. Hubsch, R. Ohm, B. J. Albright, J. C. Fernandez, D. Habs, and B. M. Hegelich, *Development of a High Resolution and High Dispersion Thomson Parabola.* Rev Sci Instrum **82** (2011), p. 013306.

[85] A. Alejo, D. Gwynne, D. Doria, H. Ahmed, D. C. Carroll, R. J. Clarke, D. Neely, G. G. Scott, M. Borghesi, and S. Kar, *Recent developments in the Thomson Parabola Spectrometer diagnostic for laser-driven multi-species ion sources.* Journal of Instrumentation **11** (2016), pp. C10005–C10005.

[86] D. Gwynne, S. Kar, D. Doria, H. Ahmed, M. Cerchez, J. Fernandez, R. J. Gray, J. S. Green, F. Hanton, D. A. MacLellan, P. McKenna, Z. Najmudin, D. Neely, J. A. Ruiz, A. Schiavi, M. Streeter, M. Swantusch, O. Willi, M. Zepf, and M. Borghesi, *Modified Thomson Spectrometer Design for High Rnergy, Multi-Species Ion Sources.* Rev Sci Instrum **85** (2014), p. 033304.

[87] K. Harres, M. Schollmeier, E. Brambrink, P. Audebert, A. Blazevic, K. Flippo, D. C. Gautier, M. Geissel, B. M. Hegelich, F. Nurnberg, J. Schreiber, H. Wahl, and M. Roth, *Development and Calibration of a Thomson Parabola with Microchannel Plate for the Detection of Laser-Accelerated MeV Ions.* Rev Sci Instrum **79** (2008), p. 093306.

[88] N. Bohr, *XXXVII. On the Constitution of Atoms and Molecules.* The London, Edinburgh, and Dublin Philosophical Magazine and Journal of Science **26** (2009), pp. 476–502.

[89] J. F. Ziegler, *Stopping of Energetic Light Ions in Elemental Matter.* Journal of Applied Physics **85** (1999), pp. 1249–1272.

[90] H. Bethe, *Zur Theorie des Durchgangs schneller Korpuskularstrahlen durch Materie.* Annalen der Physik **397** (1930), pp. 325–400.

[91] F. Bloch, *Zur Bremsung rasch bewegter Teilchen beim Durchgang durch Materie.* Annalen der Physik **408** (1933), pp. 285–320.

[92] J. O. Archambeau, G. W. Bennett, G. S. Levine, R. Cowen, and A. Akanuma, *Proton Radiation Therapy.* Radiology **110** (1974), pp. 445–57.

[93] J. F. Ziegler *The Stopping and Range of Ions in Matter Software, http://www.srim.org/.* (2013)

[94] Ashland Gafchromic, *Gafchromic HD-V2 Film Specificationand User Guide, url: http://www.gafchromic.com/documents/gafchromic-hdv2.pdf.* (2020)

[95] Martin J. Butson, Peter K. N. Yu, Tsang Cheung, and Peter Metcalfe, *Radiochromic Film for Medical Radiation Dosimetry.* Materials Science and Engineering: R: Reports **41** (2003), pp. 61–120.

[96] V. Kaymak, E. Aktan, M. Cerchez, B. Elkin, M. Papenheim, R. Prasad, A. Pukhov, H. C. Scheer, A. M. Schroer, O. Willi, and B. Aurand, *Boosted Acceleration of Protons by Tailored Ultra-Thin Foil Zargets.* Sci Rep **9** (2019), p. 18672.

[97] W. L. McLaughlin, A. Miller, S. Fidan, K. Pejtersen, and W. Batsberg Pedersen, *Radiochromic Plastic Films for Accurate Measurement of Radiation Absorbed Dose and Dose Distributions.* Radiation Physics and Chemistry (1977) **10** (1977), pp. 119–127.

[98] A. Niroomand-Rad, C. R. Blackwell, B. M. Coursey, K. P. Gall, J. M. Galvin, W. L. McLaughlin, A. S. Meigooni, R. Nath, J. E. Rodgers, and C. G. Soares, *Radiochromic Film Dosimetry: Recommendations of AAPM Radiation Therapy Committee Task Group 55. American Association of Physicists in Medicine.* Med Phys **25** (1998), pp. 2093–115.

[99] M. Borghesi, A. Schiavi, D. H. Campbell, M. G. Haines, O. Willi, A. J. Mackinnon, P. Patel, M. Galimberti, and L. A. Gizzi, *Proton Imaging Detection of Transient Electromagnetic Fields in Laser-Plasma Interactions (invited).* Review of Scientific Instruments **74** (2003), pp. 1688–1693.

[100] M. Borghesi, L. Romagnani, A. Schiavi, D. H. Campbell, M. G. Haines, O. Willi, A. J. Mackinnon, M. Galimberti, L. Gizzi, R. J. Clarke, and S. Hawkes, *Measurement of Highly Transient Electrical Charging Following High-Intensity Laser–Solid Interaction.* Applied Physics Letters **82** (2003), pp. 1529–1531.

[101] J. A. Cobble, R. P. Johnson, T. E. Cowan, N. Renard-Le Galloudec, and M. Allen, *High Resolution Laser-Driven Proton Radiography.* Journal of Applied Physics **92** (2002), pp. 1775–1779.

[102] T. E. Cowan, J. Fuchs, H. Ruhl, A. Kemp, P. Audebert, M. Roth, R. Stephens, I. Barton, A. Blazevic, E. Brambrink, J. Cobble, J. Fernandez, J. C. Gauthier, M. Geissel, M. Hegelich, J. Kaae, S. Karsch, G. P. Le Sage, S. Letzring, M. Manclossi, S. Meyroneinc, A. Newkirk, H. Pepin, and N. Renard-LeGalloudec, *Ultralow Emittance, Multi-MeV Proton Beams from a Laser Virtual-Cathode Plasma Accelerator.* Phys Rev Lett **92** (2004), p. 204801.

[103] M. Borghesi, A. J. Mackinnon, D. H. Campbell, D. G. Hicks, S. Kar, P. K. Patel, D. Price, L. Romagnani, A. Schiavi, and O. Willi, *Multi-MeV Proton Source Investigations in Ultraintense Laser-Foil Interactions.* Phys Rev Lett **92** (2004), p. 055003.

[104] William H. Press Flannery, A Saul A. Teukolsky, A William T. Vetterling, and A Brian P. *Numerical Recipes 3rd Edition: The Art of Scientific Computing.* 2007.

[105] G. Pretzler, A. Kasper, and K. J. Witte, *Angular Chirp and Tilted Light Pulses in CPA Lasers.* Applied Physics B-Lasers and Optics **70** (2000), pp. 1–9.

[106] J. Robertson, *Diamond-like amorphous carbon.* Materials Science and Engineering: R: Reports **37** (2002), pp. 129–281.

[107] V. Kh Liechtenstein, T. M. Ivkova, E. D. Olshanski, R. Repnow, P. Steier, W. Kutschera, A. Wallner, and R. von Hahn, *Preparation and Investigation of Ultra-Thin Diamond-Like Carbon (DLC) Foils Reinforced with Collodion.* Nuclear Instruments and Methods in Physics Research Section A: Accelerators, Spectrometers, Detectors and Associated Equipment **561** (2006), pp. 120–123.

[108] V. Kh Liechtenstein, T. M. Ivkova, E. D. Olshanski, R. Golser, W. Kutschera, P. Steier, C. Vockenhuber, R. Repnow, R. von Hahn, M. Friedrich, and

U. Kreissig, *Recent Investigations and Applications of Thin Diamond-Like Carbon (DLC) Foils.* Nuclear Instruments and Methods in Physics Research Section A: Accelerators, Spectrometers, Detectors and Associated Equipment **521** (2004), pp. 197–202.

[109] M. Cerchez, R. Jung, J. Osterholz, T. Toncian, O. Willi, P. Mulser, and H. Ruhl, *Absorption of Ultrashort Laser Pulses in Strongly Overdense Targets.* Phys Rev Lett **100** (2008), p. 245001.

[110] R. Sauerbrey, J. Fure, S. P. Le Blanc, B. van Wonterghem, U. Teubner, and F. P. Schäfer, *Reflectivity of Laser-Produced Plasmas Generated by a High Intensity Ultrashort Pulse*.* Physics of Plasmas **1** (1994), pp. 1635–1642.

[111] L. M. Chen, J. Zhang, Q. L. Dong, H. Teng, T. J. Liang, L. Z. Zhao, and Z. Y. Wei, *Hot Electron Generation Via Vacuum Heating Process in Femtosecond Laser–Solid Interactions.* Physics of Plasmas **8** (2001), pp. 2925–2929.

[112] P. Antici, J. Fuchs, E. d'Humières, J. Robiche, E. Brambrink, S. Atzeni, A. Schiavi, Y. Sentoku, P. Audebert, and H. Pépin, *Laser Acceleration of High-Energy Protons in Variable Density Plasmas.* New Journal of Physics **11** (2009).

[113] P. Antici, E. Boella, S. N. Chen, D. S. Andrews, M. Barberio, J. Boker, F. Cardelli, J. L. Feugeas, M. Glesser, P. Nicolai, L. Romagnani, M. Sciscio, M. Starodubtsev, O. Willi, J. C. Kieffer, V. Tikhonchuk, H. Pepin, L. O. Silva, E. Humieres, and J. Fuchs, *Acceleration of Collimated 45 MeV Protons by Collisionless Shocks Driven in Low-Density, Large-Scale Gradient Plasmas by a* $10^{20}W/cm^2$*, 1* μm *Laser.* Sci Rep **7** (2017), p. 16463.

[114] E. d'Humiéres, J. L. Feugeas, P. Nicolaï, S. Gaillard, T. Cowan, Y. Sentoku, and V. Tikhonchuk, *Investigation of High Intensity Laser Proton Acceleration with Underdense Targets.* Journal of Physics: Conference Series **244** (2010).

[115] M. N. Saha, *LIII. Ionization in the Solar Chromosphere.* The London, Edinburgh, and Dublin Philosophical Magazine and Journal of Science **40** (1920), pp. 472–488.

[116] B. Dromey, M. Zepf, A. Gopal, K. Lancaster, M. S. Wei, K. Krushelnick, M. Tatarakis, N. Vakakis, S. Moustaizis, R. Kodama, M. Tampo, C. Stoeckl, R. Clarke, H. Habara, D. Neely, S. Karsch, and P. Norreys, *High Harmonic Generation in the Relativistic Limit.* Nature Physics **2** (2006), pp. 456–459.

[117] G. S. Sarkisov, V. Yu Bychenkov, V. T. Tikhonchuk, A. Maksimchuk, S. Y. Chen, R. Wagner, G. Mourou, and D. Umstadter, *Observation of the Plasma Channel Dynamics and Coulomb Explosion in the Interaction of a High-Intensity Laser Pulse with a He Gas Jet.* Journal of Experimental and Theoretical Physics Letters **66** (1997), pp. 828–834.

[118] K. Krushelnick, E. L. Clark, Z. Najmudin, M. Salvati, M. I. K. Santala, M. Tatarakis, A. E. Dangor, V. Malka, D. Neely, R. Allott, and C. Danson, *Multi-MeV Ion Production from High-Intensity Laser Interactions with Underdense Plasmas.* Physical Review Letters **83** (1999), pp. 737–740.

[119] L. O. Silva, M. Marti, J. R. Davies, R. A. Fonseca, C. Ren, F. S. Tsung, and W. B. Mori, *Proton Shock Acceleration in Laser-Plasma Interactions.* Phys Rev Lett **92** (2004), p. 015002.

[120] L. Willingale, P. M. Nilson, A. G. R. Thomas, S. S. Bulanov, A. Maksimchuk, W. Nazarov, T. C. Sangster, C. Stoeckl, and K. Krushelnick, *High-Power, Kilojoule Laser Interactions with Near-Critical Density Plasma.* Physics of Plasmas **18** (2011).

[121] D. Giulietti, M. Galimberti, A. Giulietti, L. A. Gizzi, R. Numico, P. Tomassini, M. Borghesi, V. Malka, S. Fritzler, M. Pittman, K. Ta Phouc, and A. Pukhov, *Production of Ultracollimated Bunches of multi-MeV Electrons by 35 fs Laser Pulses Propagating in Exploding-Foil Plasmas.* Physics of Plasmas **9** (2002), pp. 3655–3658.

[122] D. B. Melrose, *Plasma Emission - a Review.* Solar Physics **111** (1987), pp. 89–101.

[123] J. A. Stamper, R. H. Lehmberg, A. Schmitt, M. J. Herbst, F. C. Young, J. H. Gardner, and S. P. Obenschain, *Evidence in the Second-Harmonic Emission for Self-Focusing of a Laser Pulse in a Plasma.* Physics of Fluids **28** (1985).

[124] S. S. Bulanov, V. Y. Bychenkov, V. Chvykov, G. Kalinchenko, D. W. Litzenberg, T. Matsuoka, A. G. Thomas, L. Willingale, V. Yanovsky, K. Krushelnick, and A. Maksimchuk, *Generation of GeV Protons from 1 PW Laser Interaction with Near Critical Density Targets.* Phys Plasmas **17** (2010).

[125] L. Willingale, S. R. Nagel, A. G. Thomas, C. Bellei, R. J. Clarke, A. E. Dangor, R. Heathcote, M. C. Kaluza, C. Kamperidis, S. Kneip, K. Krushelnick,

N. Lopes, S. P. Mangles, W. Nazarov, P. M. Nilson, and Z. Najmudin, *Characterization of High-intensity Laser Propagation in the Relativistic Transparent Regime Through Measurements of Energetic Proton Beams.* Phys Rev Lett **102** (2009), p. 125002.

[126] L.D. Landau, J.S. Bell, M.J. Kearsley, L.P. Pitaevskii, E.M. Lifshitz, and J.B. Sykes. *Electrodynamics of Continuous Media*, volume 8. elsevier, 2013.

[127] D.M. Pozar. *Microwave Engineering, 4th Edition.* Wiley, 2011.

[128] E. d'Humières, P. Antici, M. Glesser, J. Boeker, F. Cardelli, S. Chen, J. L. Feugeas, F. Filippi, M. Gauthier, A. Levy, P. Nicolaï, H. Pépin, L. Romagnani, M. Scisciò, V. T. Tikhonchuk, O. Willi, J. C. Kieffer, and J. Fuchs, *Investigation of Laser Ion Acceleration in Low-Density Targets Using Exploded Foils.* Plasma Physics and Controlled Fusion **55** (2013).

[129] M. Gauthier, A. Lévy, E. d'Humières, M. Glesser, B. Albertazzi, C. Beaucourt, J. Breil, S. N. Chen, V. Dervieux, J. L. Feugeas, P. Nicolaï, V. Tikhonchuk, H. Pépin, P. Antici, and J. Fuchs, *Investigation of Longitudinal Proton Acceleration in Exploded Targets Irradiated by Intense Short-Pulse Laser.* Physics of Plasmas **21** (2014).

[130] L. Willingale, S.P. Mangles, P.M. Nilson, R.J. Clarke, A. E. Dangor, M.C. Kaluza, S. Karsch, K. L. Lancaster, W.B. Mori, Z. Najmudin, J. Schreiber, A.G. Thomas, M.S. Wei, and K. Krushelnick, *Collimated Multi-MeV Ion Beams from High-Intensity Laser Interactions with Underdense Plasma.* Phys Rev Lett **96** (2006), p. 245002.

[131] A. Macchi. *A Superintense Laser-Plasma Interaction Theory Primer.* SpringerBriefs in Physics. 2013.

[132] K. Quinn, P. A. Wilson, C. A. Cecchetti, B. Ramakrishna, L. Romagnani, G. Sarri, L. Lancia, J. Fuchs, A. Pipahl, T. Toncian, O. Willi, R. J. Clarke, D. Neely, M. Notley, P. Gallegos, D. C. Carroll, M. N. Quinn, X. H. Yuan, P. McKenna, T. V. Liseykina, A. Macchi, and M. Borghesi, *Laser-Driven Ultrafast Field Propagation on Solid Surfaces.* Phys Rev Lett **102** (2009), p. 194801.

[133] H. Ahmed, S. Kar, G. Cantono, P. Hadjisolomou, A. Poye, D. Gwynne, C. L. S. Lewis, A. Macchi, K. Naughton, G. Nersisyan, V. Tikhonchuk,

O. Willi, and M. Borghesi, *Efficient Post-Acceleration of Protons in Helical Coil Targets Driven by sub-ps Laser Pulses.* Sci Rep **7** (2017), p. 10891.

[134] S. Kar, H. Ahmed, R. Prasad, M. Cerchez, S. Brauckmann, B. Aurand, G. Cantono, P. Hadjisolomou, C. L. Lewis, A. Macchi, G. Nersisyan, A. P. Robinson, A. M. Schroer, M. Swantusch, M. Zepf, O. Willi, and M. Borghesi, *Guided Post-Acceleration of Laser-Driven Ions by a Miniature Modular Structure.* Nat Commun **7** (2016), p. 10792.

[135] H. Ahmed, S. Kar, A. L. Giesecke, D. Doria, G. Nersisyan, O. Willi, C. L. S. Lewis, and M. Borghesi, *Proton Probing of Laser-Driven EM Pulses Travelling in Helical Coils.* High Power Laser Science and Engineering **5** (2017).

[136] H. Ahmed, S. Kar, G. Cantono, G. Nersisyan, S. Brauckmann, D. Doria, D. Gwynne, A. Macchi, K. Naughton, O. Willi, C. L. S. Lewis, and M. Borghesi, *Investigations of Ultrafast Charge Dynamics in Laser-Irradiated Targets by a Self Probing Technique Employing Laser Driven Protons.* Nuclear Instruments and Methods in Physics Research Section A: Accelerators, Spectrometers, Detectors and Associated Equipment **829** (2016), pp. 172–175.

[137] Extreme Light Infrastructure *ELI, https://eli-laser.eu/* (2020).

[138] Laboratoire pour l'utilisation des lasers intense, *Apollon, https://portail.polytechnique.edu/luli/en/cilex-apollon/apollon* (2020).

[139] E. Aktan, H. Ahmed, B. Aurand, M. Cerchez, A. Poyé, P. Hadjisolomou, M. Borghesi, S. Kar, O. Willi, and R. Prasad, *Parametric Study of a High Amplitude Electromagnetic Pulse Driven by an Intense Laser.* Physics of Plasmas **26** (2019).

[140] J. L. Dubois, F. Lubrano-Lavaderci, D. Raffestin, J. Ribolzi, J. Gazave, A. Compant La Fontaine, E. d'Humieres, S. Hulin, P. Nicolai, A. Poye, and V. T. Tikhonchuk, *Target Charging in Short-Pulse-Laser-Plasma Experiments.* Phys Rev E Stat Nonlin Soft Matter Phys **89** (2014), p. 013102.

[141] J. S. Pearlman and G. H. Dahlbacka, *Charge Separation and Target Voltages in Laser-Produced Plasmas.* Applied Physics Letters **31** (1977), pp. 414–417.

[142] M. J. Mead, D. Neely, J. Gauoin, R. Heathcote, and P. Patel, *Electromagnetic Pulse Generation Within a Petawatt Laser Target Chamber.* Review of Scientific Instruments **75** (2004), pp. 4225–4227.

[143] A. Poye, J. L. Dubois, F. Lubrano-Lavaderci, E. D'Humieres, M. Bardon, S. Hulin, M. Bailly-Grandvaux, J. Ribolzi, D. Raffestin, J. J. Santos, P. Nicolai, and V. Tikhonchuk, *Dynamic Model of Target Charging by Short Laser Pulse Interactions.* Phys Rev E Stat Nonlin Soft Matter Phys **92** (2015), p. 043107.

[144] M. G. Haines, M. S. Wei, F. N. Beg, and R. B. Stephens, *Hot-Electron Temperature and Laser-Light Absorption in Fast Ignition.* Phys Rev Lett **102** (2009), p. 045008.

[145] S. Tokita, S. Sakabe, T. Nagashima, M. Hashida, and S. Inoue, *Strong Sub-Terahertz Surface Waves Generated on a Metal Wire by High-Intensity Laser Pulses.* Sci Rep **5** (2015), p. 8268.

[146] John D. Cutnell, Kenneth W. Johnson. *Physics.* 9th edition, 2012.

[147] G. Malka and J. L. Miquel, *Experimental Confirmation of Ponderomotive-Force Electrons Produced by an Ultrarelativistic Laser Pulse on a Solid Target.* Phys Rev Lett **77** (1996), pp. 75–78.

[148] K. B. Wharton, S. P. Hatchett, S. C. Wilks, M. H. Key, J. D. Moody, V. Yanovsky, A. A. Offenberger, B. A. Hammel, M. D. Perry, and C. Joshi, *Experimental Measurements of Hot Electrons Generated by Ultraintense ($>10^{19} W/cm^2$) Laser-Plasma Interactions on Solid-Density Targets.* Phys Rev Lett **81** (1998), pp. 822–825

[149] A. Poyé, S. Hulin, J. Ribolzi, M. Bailly-Grandvaux, F. Lubrano-Lavaderci, M. Bardon, D. Raffestin, J. J. Santos, and V. Tikhonchuk, *Thin Target Charging in Short Laser Pulse Interactions.* Physical Review E **98** (2018).

[150] National Institute of Standards and Technology, *ESTAR - Stopping-Power and Range tables for Electrons, https://physics.nist.gov/PhysRefData/Star/Text/ESTAR.html* (2019, November 15).

[151] A. Poye, J. L. Dubois, F. Lubrano-Lavaderci, E. D'Humieres, M. Bardon, S. Hulin, M. Bailly-Grandvaux, J. Ribolzi, D. Raffestin, J. J. Santos, P. Nicolai, and V. Tikhonchuk, *Dynamic Model of Target Charging by Short Laser Pulse Interactions (Supplemental Material at http://link.aps.org/supplemental/10.1103/PhysRevE.92.043107).* 2015.

[152] M. Allen, Y. Sentoku, P. Audebert, A. Blazevic, T. Cowan, J. Fuchs, J. C. Gauthier, M. Geissel, M. Hegelich, S. Karsch, E. Morse, P. K. Patel, and M. Roth, *Proton Spectra from Ultraintense Laser–Plasma Interaction with Thin Foils: Experiments, Theory, and Simulation*. Physics of Plasmas **10** (2003), pp. 3283–3289.

[153] A. Macchi, S. Veghini, and F. Pegoraro, *"Light Sail" Acceleration Reexamined*. Phys Rev Lett **103** (2009), p. 085003.

[154] L. Romagnani. *Laser-Plasma Investigations Employing Laser-Driven Proton Probes*. Doctoral thesis (2005).

[155] Ernst E. Fill, *Ultrashort-Pulse Laser Plasmas: Fraction of Hot Electrons Escaping From the Target and Electron Spectra in Planar and Spherical Geometry*. Physics of Plasmas **12** (2005).

[156] K. Bennett, C. Brady, H. Schmitz, C. Ridgers, T. Arber, R. Evans, and T. Bell *Users Manual for the EPOCH PIC codes*. University of Warwick, Coventry, UK (2017).

List of Publications

- B. Aurand, K. Schwind, T. Toncian, E. Aktan, M. Cerchez, L. Lessmann, C. Mannweiler, R. Prasad, A. Khoukaz and O. Willi, *Study of the parameter dependence of laser-accelerated protons from a hydrogen cluster source.* New Journal of Physics **22** (2020).

- V. Kaymak, E. Aktan, M. Cerchez, B. Elkin, M. Papenheim, R. Prasad, A. Pukhov, H. Scheer, A.-M. Schroer, O. Willi, and B. Aurand, *Boosted acceleration of protons by tailored ultra-thin foil targets.* Scientific Reports **9** (2019).

- E. Aktan, H. Ahmed, B. Aurand, M. Cerchez, A. Poye, P. Hadjisolomou, M. Borghesi, S. Kar, O. Willi and R. Prasad, *Parametric study of a high amplitude electromagnetic pulse driven by an intense laser.* Physics of Plasmas **26** 070701 (2019).

- B. Aurand, S. Grieser, T. Toncian, E. Aktan, M Cerchez, L. Leßmann, R. Prasad, A. Khoukaz and O. Willi, *A multihertz, kiloelectronvolt pulsed proton source from a laser irradiated continuous hydrogen cluster target.* Physics of Plasmas **26** 073102 (2019).

- K. Schwind, E. Aktan, R. Prasad, M. Cerchez, D. Eversheim, O. Willi and B. Aurand, *An online beam profiler for laser-accelerated protons.* Review of Scientific Instruments **90** 053307 (2019).

- S. Grieser, B. Aurand, E. Aktan, D. Bonaventura, M. Büscher, M. Cerchez, I. Engin, L. Leßmann, C. Mannweiler, R. Prasad, O. Willi, and A. Khoukaz, *Nm-sized cryogenic hydrogen clusters for a laser-driven proton source.* Review of Scientific Instruments **90** 043301 (2019).

- K. Schwind, E. Aktan, M. Cerchez, R. Prasad, O. Willi, and B. Aurand, *A high-repetition rate droplet-source for plasma physics applications.* Nuclear Instruments and Methods in Physics Research Section A: Accelerators, Spectrometers, Detectors and Associated Equipment **928** (2019).

- M. Cerchez, R. Prasad, B. Aurand, A.-L. Giesecke, S. Spickermann, S. Brauckmann, E. Aktan, M. Swantusch, M. Toncian, T. Toncian, and O. Willi, *ARCTURUS laser: a versatile high-contrast, high-power multi-beam laser system.* High Power Laser Science and Engineering **7** (2019).

Acknowledgement

The completion of this thesis would not have been possible without the support and guidance of a few people. I would like to use this opportunity and thank them all. I'm not a person of many words, but here I go.

First of all, I would like to thank my academic supervisor Prof. Willi for offering me the opportunity to do my PhD in his working group. His enthusiasm about this highly interesting research field was always contagious and he always managed to motivate me throughout my time as a student at his institute. No matter how frustrating the situation was, I could always count on his support. Not only his vast knowledge, but also his moral advice and encouragement guided my way through the hard work.

I would like to thank Prof. Pukhov for being the second referee of my PhD thesis. The discussions with him and his working group were always fruitful.

Special thanks to Dr. Rajendra Prasad! He did not only make me believe that sleeping is just a bad habit, but also that every cloud has a silver lining. Without his persistent optimism and never-ending enthusiasm, the long days and nights in the lab would have been even more strenuous.

I would like to thank Dr. Mirela Cerchez for her great support. Even if she had a desk full of paperwork and a bunch of other things to do, she did not hesitate to make time to answer any of my questions.

Many thanks also to Dr. Aurand who would lend a helping hand any time needed. He was always supportive regardless the topic.

I was lucky to work alongside very kind colleagues. Whether working in the lab or just chatting in the kitchen (mostly while eating cake) it was great to have companions along the exhausting journey. I thank all the other (former) PhD-/Master-/Bachelor-students which I met during my PhD.

I also would like to thank my friend Max, for distracting me from work whenever I felt like drowning. His support is invaluable.

Finally, I would like to dedicate this thesis to my family. Especially in this last stage of my very exhausting study, I would have been lost without their endless support. I am very grateful that my parents and my brother never stopped believing in me and that I could always count on them.

Statutory Declaration

I hereby declare that the thesis submitted is composed by myself without any restricted help and the work herein is my own except explicitly stated. All material which has been quoted either literally or by content from the used sources are acknowledged as references.

This thesis was not previously presented to another examination board and has not been published.

city, date	Esin Aktan